Justus-Liebig-Universität Gießen
I. Physikalisches Institut

Charge-Transfer Dynamics in Molecular Donor-Acceptor Systems and Heterostructures

Dissertation

zur Erlangung des Doktorgrades
der Naturwissenschaften
–Dr. rer. nat.–

dem
Fachbereich 07
Mathematik und Informatik, Physik, Geographie
vorgelegt von

Robin Carl Döring

aus

Hamburg

Giessen, im Juni 2018

Erstgutachter:	Prof. Dr. Sangam Chatterjee
Zweitgutachter:	Prof. Dr. Derck Schlettwein

Selbstständigkeitserklärung

Ich erkläre: Ich habe die vorgelegte Dissertation selbstständig und ohne unerlaubte fremde Hilfe und nur mit den Hilfen angefertigt, die ich in der Dissertation angegeben habe. Alle Textstellen, die wörtlich oder sinngemäß aus veröffentlichten Schriften entnommen sind, und alle Angaben, die auf mündlichen Auskünften beruhen, sind als solche kenntlich gemacht. Ich stimme einer evtl. Überprüfung meiner Dissertation durch eine Antiplagiat-Software zu. Bei den von mir durchgeführten und in der Dissertation erwähnten Untersuchungen habe ich die Grundsätze guter wissenschaftlicher Praxis, wie sie in der "Satzung der Justus-Liebig-Universität Gießen zur Sicherung guter wissenschaftlicher Praxis" niedergelegt sind, eingehalten.

(Ort, Datum)	(Robin Carl Döring)

Zusammenfassung

In der vorliegenden Arbeit wurden drei verschiedene molekulare Materialien spektroskopisch untersucht. Des Weiteren wurden die verwendeten spektroskopischen Methoden aufgebaut oder erweitert. Unter anderem wurde ein experimenteller Aufbau für Photolumineszenz-Anregungsspektroskopie bei kryogenen Temperaturen für die Untersuchung der Besetzungsdynamik von Charge-Transfer-(CT)-Exzitonen in molekularen Festkörpern konzipiert, aufgebaut und charakterisiert.
Zunächst wurden Perylen-Derivate untersucht. Diese Derivate sind vielversprechend für eine Vielzahl von technischen Anwendungen, unter anderem als Autolacke, pH-Sensoren oder als Bausteine von organischen Solarzellen. Für die vorliegende Arbeit wurden spezielle Donor-Akzeptor-Moleküle synthetisiert, die gewissermaßen eine intramolekulare Grenzfläche darstellen. Ziel war es, die Ladungstransferraten zu bestimmen und durch verschiedene synthetische und experimentelle Methoden zu kontrollieren.
Molekulare Festkörper, bestehend aus Heterostrukturen von Donor- und Akzeptor-Molekülen können an der Grenzfläche zwischen beiden Materialien sogenannte CT-Exzitonen ausbilden. Die Untersuchung von CT-Exzitonen ist entscheidend aus technischer Sicht–zur Optimierung von organischen Solarzellen–und auch aus Sicht der Grundlagenforschung. Im Rahmen der Arbeit werden Erkenntnisse bezüglich des Besetzungsverhaltens des CT-Zustandes im Materialsystem Pentacen-Perflouropentacen gewonnen. Die erzielten Ergebnisse haben potentiell eine gewisse grundsätzliche Tragweite für das Verständnis von CT-Zuständen. So wurde festgestellt, dass ein möglicher Lochtransfer vom Akzeptor in das Donormaterial nicht zu einem messbaren CT-Lumineszenzsignal führt, der umgekehrte Fall des Elektronentransfer vom Donormaterial hingegen schon. Da Proben höchster struktureller Güte mit einer wohldefinierten Grenzfläche verwendet wurden, konnten die Messergebnisse eindeutig als Grenzflächeneffekt identifiziert werden. Durch Untersuchung unterschiedlicher Molekülorientierungen an der Grenzfläche, konnte die Vermutung erhöhter elektronischer Kopplung im Falle

eines sogenannten π-stackings der Moleküle bestätigt werden. Für das Materialsystem Pentacen-C_{60} konnte erstmalig an einer wohldefinierten Grenzfläche ein CT-Signal direkt gemessen werden. Weiterhin zeigen die Messungen, dass ein langreichweitiger Effekt die Dynamik der C_{60} -Lumineszenz und die Mobilität angeregter Zustände beeinflusst.

List of Abbreviations

A	acceptor
CCD	charge-coupled device
CS	charge separation
CSS	charge separated state
CV	cyclic voltammetry
CW	continous wave
CT	charge-transfer
C_{60}	C_{60}
D	donor
DFT	density functional theory
DOS	density of states
EELS	electron energy loss spectroscopy
EET	excitation energy transfer
ECA	exciton charge annihilation
EL	electroluminescence
ESHT	excited state hydrogen transfer
ET	electron transfer
FCC	face centered cubic
FGR	Fermi's golden rule
FX	free exciton
HOMO	highest occupied molecular orbital
HT	Herzberg-Teller
IC	internal conversion
IPES	inverse photoelectron spectroscopy
IR	infra-red
ISC	Intersystem crossing
LCD	liquid crystal display

LED	light emitting diode
l.h.s.	left-hand side
LUMO	lowest unoccupied molecular orbital
MO	molecular orbital
OLED	organic light emitting diode
OMBE	(organic) molecular beam epitaxy
OPV	organic photovoltaics
PDI	perylene diimide
PEN	pentacene
PEP	potential energy profile
PES	photoelectron spectroscopy
PFP	perflouropentacene
PL	photoluminescence
PLE	photoluminescence excitation
PLQY	PL quantum yield
PEDOT:PSS	poly(ethylenedioxythiophene):poly(styrenesulfonate)
PMMA	poly(methyl methacrylate)
RET	(Förster) resonant energy transfer
r.h.s.	right-hand side
SF	singlet fission
STM	scanning tunneling microscopy
TDDFT	time-dependent density functional theory
TDM	transition dipole moment
TRPL	time-resolved photoluminescence
UPS	ultraviolet photoelectron spectroscopy
UV	ultraviolet
VP	vibronic progression
VR	vibrational relaxation

Contents

List of Tables

List of Figures

1 Introduction

The very making of this thesis depends heavily on several fundamental technological developments and pioneering scientific discoveries of the last century: Starting with the development of the first transistor by Bardeen, Brattain and Shockley [1], the discovery of the laser by Theodore Maiman [2][1] or the development of the first integrated circuit by Kilby [3][2] in the 1960s. The latter paved the way for modern day microprocessing units and data storage. Silicon has since been established as the backbone of modern computer technology, manifested, e.g., by the naming of the global hub for high technology as "Silicon Valley". As the base of applications expanded over the course of time, so did the materials base. Hence, semiconductor devices nowadays act, e.g., as light sources [lasers, light emitting diodes (LEDs)], detectors [charge-coupled devices (CCDs)] and sources of electrical power (solar cells), thereby making use of a broad combination of different materials.

However, natural resources are limited, and most devices rely on rare earth metals and potentially hazardous materials. Since the late 1990s, the class of organic semiconductors has become increasingly popular as an alternative to the established inorganic semiconductors. Nowadays, several display manufacturers employ organic light emitting diode (OLED) technology due to its superior color contrast and mechanical flexibility, as well as increased efficiencies, compared to conventional liquid crystal displays (LCDs). Moreover, global demographics and the potential threats caused by climate change demand new forms of sustainable and efficient light and energy sources. The amount of sunlight reaching earth ($\approx$122 PW) exceeds the global consumption of electrical power by almost four orders of magnitude [4]. This abundance strongly suggests the use of solar energy as the primary energy source. While silicon-based devices

[1] Maiman is not universally credited with the invention of the laser, despite later being granted the patent. Gordon Gould, who first came up with the acronym LASER (light amplification by stimulated emission of radiation), is also attributed with the invention by some.

[2] Early predecessors were already fabricated at the end of WWII by engineers at Siemens.

have the largest market share (>90 % [5]), the production costs are still high, despite the very advanced manufacturing techniques. The use of organic materials offers a wide range of potential advantages: low cost, due to solution-processibility; high mechanical flexibility and low weight[3]; the possibility of engineering crucial device parameters such as the electrical band gap by appropriate choice or by specific chemical synthesis of the molecules constituting the device.

Beyond their prospective technological benefit, organic molecules and solids are an active field of scientific research. As most device structures are hetero-systems of some type, i.e., constituted of more than one type of molecule, there exists a region in every structure in which an interface between the two materials is formed. The ongoing miniaturization of electronic devices stresses the crucial role of the interfacial region. Hence, (internal) interfaces will be the main topic of this thesis. The aim is to identify spectroscopic signatures specific to the interface. For example, an excited state can form at the interface where one material acts as (electron) donor (D), while the other material is the (electron) acceptor (A). Such an excitation is commonly referred to as a charge-transfer (CT) exciton. Its exciton binding energy can vary broadly, while it is expected to be smaller than that of the bulk excitons in the individual constituents. A larger exciton radius typically leads to such reduced binding energies. While interface-specific spectroscopic signals are not always observable, other effects, e.g., altered decay dynamics of the constituents, can arise as a consequence of the hetero-stacking of two organic materials. CT states are of particular use for OPV applications as they act as precursors leading to the separation of charges, the ultimate goal in OPV devices. However, the beneficial properties of CT states are not limited to this kind of applications; they are also promising for OLED devices due to, e.g., the low operating voltage [6] and the emission wavelength tunability achievable by an appropriate selection of D and A materials [7]. The insights gained in the course of this thesis will possibly contribute to the understanding of this type of materials. Eventually, they might even allow researchers and engineers working on the development of organic solar cells, photodetectors, and OLEDs to improve device performance by, e.g., specific control of the CT state's properties through choice of respective molecules, molecular orientation and interfacial properties at the internal interfaces.

Chaps. 2 and 3 act as an introduction to the theoretical background and description

[3]The generally very large absorption cross-section allows organic photovoltaics (OPV) cells to be produced as thin-film structures with thicknesses on the order of 100 nm.

of experimental techniques which are a prerequisite for an understanding of the results obtained in Chaps. 4-6. The focus is laid on the description of electronic states of single molecules and the respective coupling mechanisms which can lead to, e.g., CT reactions. The chapter on experimental techniques encompasses time-integrated and time-resolved spectroscopic techniques.

The results section (Chaps. 4-6) opens with the discussion of a series of specially synthesized perylene diimide (PDI) molecules. Here, synthesis was aimed at creating interfaces on a molecular scale. More specifically, a molecular D-A complex was designed, in which an electron lone pair localized on a nitrogen atom can act as electron D [8]. The backbone of the molecule, essentially a perylene unit, acts as an electron A [9]. In contrast to the systems discussed in Chap. 5 and 6, D and A are bound covalently. The chapter on the PDIs is dedicated mainly to the control of intramolecular CT rates. Large rates are desirable in a typical device scheme for the active layer of an OPV cell [10]. For the recombination of the separated electron-hole pair back to the ground state, the opposite is desired in order to maximize the number of charges to be extracted and thus increase device efficiency. The results obtained in this thesis indicate that control of the CT rates can be established by different means: by protonation and methylation, by variation of the D-A distance and by tuning the excitation energies used in the time-resolved measurements.

Additionally, two different van der Waals heterosystems are investigated. From a fundamental perspective, the microscopic understanding of the excitonic and interfacial processes in these types of materials is still at an unsatisfactory level. This hampers further progress in device fabrication. For instance, the effect of the geometrical orientation of the molecules at the interface is generally not well studied, owing to the challenges involved in growing well-defined hetero-interfaces of ordered molecular materials. Theoeretical considerations hint at a significant dependence on the molecular orientation, indicating formation efficiences varying in some cases by several orders of magnitude [11]. To this end, samples of unprecedented structural quality are used throughout this thesis, thus enabling more detailed study of the above-mentioned aspects.

The pentacene (PEN)-perflouropentacene (PFP) heterosystem is a very promising model system for the study of interfacial CT interactions in well-defined heterostructures. While structurally almost identical, the large electronegativity of flourine signif-

icantly alters the electronic properties of PFP. For instance, PFP features an inverted quadropole moment [12], compared to PEN, as well as overall lowered electronic state energies [13]. Hence, PFP acts as an electron acceptor, while PEN is a donor in this combination [14]. By means of templated sample growth [15], differences in coupling strengths for different molecular orientations can be analyzed in the case of the model system PEN-PFP. The coupling is expected to be enhanced for face-to-face growth. In a face-to-face packing motif, the overlap of the π electron systems of D and A is increased, compared to edge-to-edge orientation. In a commonly employed picture, the molecular orbitals (MOs) of the constituents are unperturbed at the interface [7], leading to an allowed electronic transition between the D highest occupied molecular orbital (HOMO) and the A lowest unoccupied molecular orbital (LUMO). This assumption is put to the test and the results obtained within this thesis indicate a more complex formation process involving perturbated MOs.

In Chap. 6 the focus is shifted towards a related model structure, namely the PEN-C_{60} (C_{60}) heterosystem. Generally, the most common applications are realized by combining a polymer material with fullerene derivatives [16–19]. However, these systems often only form blend films with very little crystal orientation. The added complexity of the molecules further cumbers the understanding of the very fundamental processes of charge-carrier generation, dissociation, transport, and extraction, respectively. Hence, no unambigious identification of an interfacial CT state has been reported to date. While PEN and C_{60} are not as compatible structurally, compared to PEN and PFP, smooth interfaces with very little mutual interdiffusion can still be achieved [20, 21]. In the case of the PEN-C_{60} system, the experiments lag behind the theoretical level of knowledge.

2 Theoretical Background

This chapter outlines the theoretical foundations for the following studies. It focuses especially on the electronic and optical properties of single molecules and mechanisms of charge transfer. As excitations in a solid are typically described in an excitonic picture, excitons in inorganic and organic solids as well as CT excitons are discussed.

2.1 Electronic Processes in Organic Molecules

In this chapter, the fundamental electronic properties of organic molecules are introduced. Already the definition of organic materials is somewhat arbitrary. One simple and broad definition states that virtually any compound containing carbon is to be named organic. Other definitions of the term "organic" require the carbon atoms to be the main structural element of the compound, or, more specifically, the compound must consist of (aromatic) hydrocarbons. For the sake of simplicity and generality, the terms "molecular" and "organic" will be used equivalently in the following. The building blocks of the acenes and also of perylene and its derivatives, are benzene molecules. Hence, the chapter will be restricted to the properties deriving from the delocalized π-orbitals.

2.1.1 Delocalized π-orbitals

From standard textbooks [22–24] it is known that atomic orbitals can hybidrize. For instance, one s- and two p-orbitals can combine to form three so-called sp^2 hybrid-orbitals. The energy required to lift one s-electron to a p-level is overcompensated by a lowering of the total energy once a bond to another atom is made. The electronic ground state configuration of carbon is $(1s^2)(2s^2)(2p_x^1)(2p_y^1)$. The sp^2-hybridization

leads to a $(2sp^3)(1p_z^1)$ configuration and, e.g., to the planar ring geometry of benzene (C_6H_6). In benzene each carbon atom forms bonds within the x-y-plane to two neighboring carbon and one hydrogen atoms at a bond angle of 120°. These localized bonds are called σ-bonds. The six remaining unpaired p_z electrons are oriented perpendicular to the plane of the σ-bonds and, thus, the plane of the molecule. The orbitals overlap, further increasing the strength of the inter-atomic bond. The neighboring orbitals become delocalized within the plane of the molecule. The bond length of the C-C bonds within the ring (137 pm) is intermediate between C-C single (140 pm) and double (135 pm) bonds, consistent with electron delocalization. The electrons are thus equally distributed between the carbon atoms with the plane of the molecule forming the nodal plane of electron density, meaning that the electrons are able to move rather "freely".

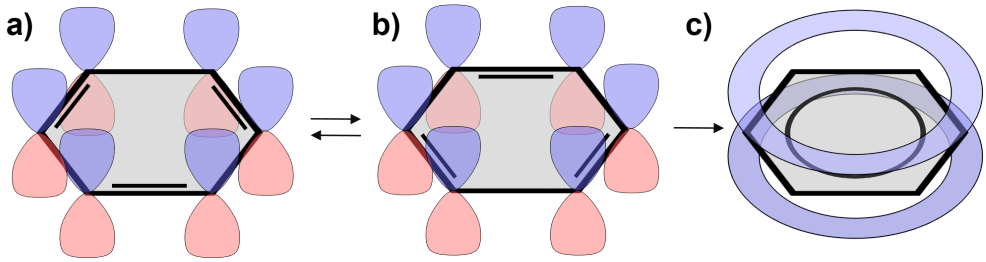

Figure 2.1: (a) The benzene molecule with its six p_z electrons forming three double bonds between the neighboring atoms at the 1-2, 3-4 and 5-6 positions and respectively at the 2-3, 4-5 and 6-1 positions (b). (c) shows the resulting delocalized π-electron system.

Due to the low strength of bonds formed by p_z electrons, the lowest electronic transitions in such molecules usually lie within the π-electron system. The $\pi \rightarrow \pi^*$ transition energy between the bonding π and antibonding π^* state typically lies in the range of 1–4 eV for many polycyclic aromatic hydrocarbons. Thus, they often comprise the HOMO and LUMO. In more complex molecules inhabiting electron lone pairs, the HOMO-LUMO transition may be of the $n \rightarrow \pi^*$ rather than of the $\pi \rightarrow \pi^*$ type [25]. Optical transition energies between the bonding and antibonding π-orbitals can be approximated by assuming the electrons as free particles in a potential well. This very crude approximation gives surprisingly precise estimates for the transition energy between the quantized states. A more precise description of the optical properties can be obtained by the evaluating the transition dipole matrix element, μ_{fi}, as introduced in the following chapters.

2.1.2 Born-Oppenheimer Approximation

Within the Born-Oppenheimer approximation the wavefunctions describing electronic and nuclear motion in a molecule can be separated. This assumption is generally valid, as the mass of the nucleus is much larger than that of the electrons (e.g., $m_N/m_{el} \approx 2 \cdot 10^3$ for hydrogen). The electron cloud can thus respond to any motion of the nuclei quasi instantaneously. Consequently, the total wavefunction Ψ_{tot} of the molecule

$$\Psi_{tot}\left(\mathbf{r_i}, \mathbf{Q_j}\right) \approx \chi_N\left(\mathbf{Q_j}\right) \cdot \Psi_{el}\left(\mathbf{r_i}, \mathbf{Q_j}\right), \tag{2.1}$$

can be expressed as a product of one wavefunction, $\chi_N\left(\mathbf{Q_j}\right)$, describing nuclear motion and another, $\Psi_{el}\left(\mathbf{r_i}, \mathbf{Q_j}\right)$, describing the electronic motion. As the nuclei are seen as rigid, the nuclear co-ordinate $\mathbf{Q_j}$ enters as parameter in the electronic wavefunction Ψ_{el}. It is important to note that this does not imply that electron-nucleus interactions vanish. The electrons are still attracted by the Coulomb potential created by the nuclei fixed at certain positions in space.

2.1.3 Franck-Condon Principle

Adopting the principles of the Born-Oppenheimer approximation essentially means that electronic transitions from state $|i\rangle$, e.g., the ground state, to state $|f\rangle$, e.g., the first electronically excited state take place "vertically". Starting from the ground-state equilibrium co-ordinate $\mathbf{Q^i}$, the system is transferred to that point on the potential energy curve of $|f\rangle$ that corresponds to the same co-ordinate. Essentially, this implies that the nuclear framework remains constant during the transition (as the transition time is on the order of 10^{-15} s whereas one oscillation period of the nucleus is typically on the order of 10^{-13} s). As the momentum $\hbar k$ of the absorbed photon is negligibly small compared to that of the nuclei, their respective momentum and thus also their kinetic energy $\langle T_N \rangle$ remains constant during the transition. Energy conservation

$$
\begin{aligned}
h \cdot \nu &= \left\langle H^f \right\rangle - \left\langle H^i \right\rangle \\
&= \left\langle U^f \right\rangle + \left\langle T^f \right\rangle - \left[\left\langle U^i \right\rangle + \left\langle T^i \right\rangle \right] \\
&= \left\langle U^f \right\rangle - \left\langle U^i \right\rangle ,
\end{aligned}
\tag{2.2}
$$

thus leads to the conclusion that the transition will take place at the co-ordinate $\mathbf{Q}^*$ for which $\langle T_N^i(\mathbf{Q}^*)\rangle = \left\langle T_N^f(\mathbf{Q}^*)\right\rangle$ holds. The strength of transitions is determined by the transition dipole matrix element

$$
\mu_{fi} = \langle f | \hat{\mu} | i \rangle . \tag{2.3}
$$

The dipole operator, again in Born-Oppenheimer approximation, is the sum over all nuclear and electronic co-ordinates and reads

$$
\hat{\mu} = -e \sum_n \mathbf{r_n} + -e \sum_m Z_m \mathbf{Q_m}. \tag{2.4}
$$

The total state of the molecule consists of a nuclear part $|\nu\rangle$ and an electronic part $|\epsilon\rangle$. Combining Eqs. (2.3) and (2.4) yields the matrix element μ_{fi}

$$
\begin{aligned}
\mu_{fi} &= \langle \epsilon_f \nu_f | - e \sum_n \mathbf{r_n} + e \sum_m \mathbf{Q_m} | \epsilon_i \nu_i \rangle \\
&= -e \sum_n \langle \epsilon_f | \mathbf{r_n} | \epsilon_i \rangle \langle \nu_f | \nu_i \rangle + e \sum_m \langle \epsilon_f | \epsilon_i \rangle \langle \nu_f | \mathbf{Q_m} | \nu_i \rangle \\
&= -e \sum_n \langle \epsilon_f | \mathbf{r_n} | \epsilon_i \rangle \langle \nu_f | \nu_i \rangle .
\end{aligned}
\tag{2.5}
$$

The right-hand side (r.h.s.) of the second row of Eq. (2.5) vanishes, because for two different electronic wavefunctions $\langle \epsilon_f | \epsilon_i \rangle = 0$. The transition intensity is proportional to the square of the transition dipole matrix element $|\mu_{fi}|^2$. Therefore, it follows that the intensity distribution for a given electronic transition is proportional to the overlap integral between the vibrational wavefunctions, $|\nu_i\rangle$, in the initial electronic state and those of the final electronic state, $|\nu_f\rangle$, respectively. It is thus determined by the Franck-Condon factor $S = \langle \nu_f | \nu_i \rangle^2$. From this relationship arise the very fundamental spectroscopic observations valid for many molecular systems, which are explained in

more detail in the following. Also, as electronic transitions take place from one vibrational level in the initial state to another in the final state, such transitions of coupled electronic *and* vibrational excitations are termed *vibronic*.

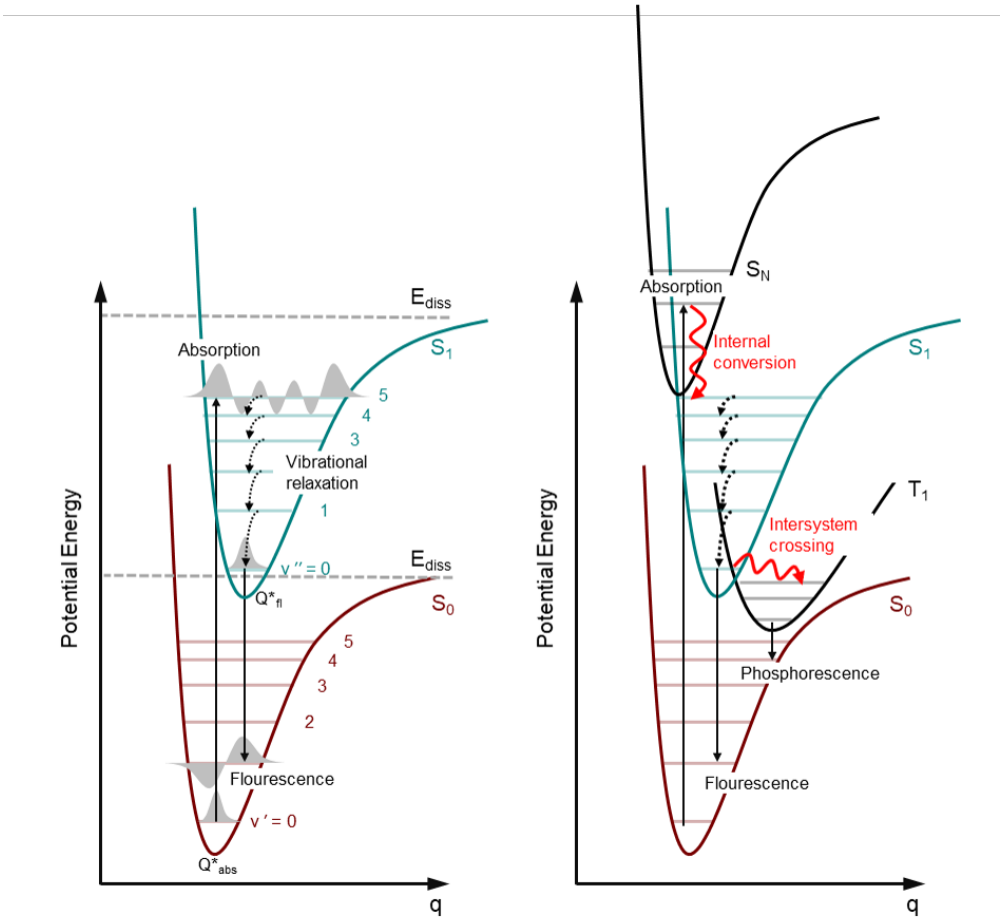

Figure 2.2: (a) Illustration of the Franck-Condon principle. Transitions between the two electronic states S_0 and S_1 take place where the vibrational wavefunctions overlap the most. In the case shown here, absorption occurs from the $\nu' = 0$ to the $\nu'' = 5$ state. Fast vibrational relaxation the $\nu'' = 0$ state is followed by a flourescent transition to the $\nu' = 1$ state, again the two states for which wavefunction overlap maximizes. (b) Higher energy states S_N relax to first excited singlet state through internal conversion at the co-ordinate the two PEP intersect. Crossing from the singlet to the triplet manifold is termed ISC and leads to the observation of the long-lived phosphorescence.

Fig. 2.2 illustrates the Franck-Condon principle. The abscissa shows a generalized molecular co-ordinate which, in the case of a diatomic molecule, would simply be

the inter-atomic displacement. On the ordinate the potential energy of the molecule is plotted. In the more general case, the displacement co-ordinate would be n-dimensional and thus the potential energy would be described by an n-dimensional hyper surface. In Fig. 2.2 the horizontal offset of the potential curves is quite significant, while their shape is almost identical. Consequently, when a photon is absorbed, the largest S is achieved for the $\nu' = 0 \rightarrow \nu'' = 5$ transition. Following the absorption of a photon, the molecule rapidly relaxes to the zero-vibrational level through the process of vibrational relaxation. This typically takes place on a timescale ranging from 0.01 ps - 10 ps [26]. From the zero vibrational level, there exist in principle three different processes for the relaxation back into the ground state:

- *Radiative recombination*: The system relaxes to the (electronic) ground state and thereby emits a photon whose energy corresponds to the energy of the vertical transition between the two states. This process thus obeys the Franck-Condon principle. The typical timescale is 10^{-9}–10^{-7} s.

- *Internal conversion (IC)*: IC is a non-radiative isoenergetic decay mechanism between two states of same multiplicity, i.e., $S_m \rightarrow S_n, n = m - 1$. It occurs predominantly in the vicinity of an intersection of the potential energy curves of two states as here their nuclear energies match (isoenergetic). If the vibrational level of state S_n is an excited one, vibrational relaxation to the ground level will occur. The time frame is the same as for vibrational relaxation. While extremely efficient for transitions with $m > 2$ and $n \geq 1$, the transit to the ground state S_0 is very slow due to the large energy gap ($\approx$2 eV) and the small overlap of energy levels. Hence, radiative recombination becomes a competitive or even the dominant relaxation mechanism.

- *Intersystem crossing (ISC) and phosphorescence*: ISC describes the transition from a state with a total spin of $S = 0$ in which electrons are pairwise coupled to a state for which $S = 1$. It is, essentially, an internal conversion (IC) process involving a spin flip. While it is generally selection rule forbidden, it can, however, gain significance under certain circumstances. The molecules studied in this thesis are constructed of lightweight atoms like hydrogen, carbon, nitrogen, oxygen and flourine. Thus, spin-orbit interaction is expected to be low, as it scales with the atomic charge number (and thus the atomic mass) squared. For theoretical details on the ISC process, see Chap. 2.1.4.

- Besides those already mentioned, there exist several other mechanisms leading to a relaxation to the ground state, all of which have in common the property of being non-intrinsic and thus relying on bi-molecular interaction, complex formation or the existence of a so-called supramolecular species. The reader is referred to Chaps. 2.1.4 and 4 in which these processes are treated in detail.

For the class of conjugated molecules studied in this thesis the most prominent vibrational excitation is associated with a vinyl stretching mode with an energy of ≈175 meV [27]. The population of the vibrational levels follows a Boltzmann distribution and thus, already at room temperature ($k_BT \approx 25$ meV), it is highly unlikely (approx. 1:1000) to find a molecule in which even one vibrational quantum is excited. Consequently, any probed transition will always be a $\nu_i = 0 \rightarrow \nu_f \geq 0$ transition where ν_f is the vibrational quantum number of the final state. That means performing a fluorescence measurement yields information about the vibrational structure of the ground state, whereas in an absorption measurement the excited state is probed [25]. The vibrational levels themselves are split again into rotational sublevels. Their energies, however, are on the µeV energy scale and thus not resolved with the experimental techniques used within this thesis.

2.1.4 The Triplet System

In systems with low coupling of the spin- and the orbital angular momentum, the spin remains a good quantum number. Thus, two electrons with the same principle, orbital and magnetic quantum numbers must have opposite spin, owing to Pauli's exclusion principle. As spin-orbit coupling increases with the atomic mass squared, its magnitude can be expected to be small in the systems under study in this thesis. The total wavefunction can be separated into two individual parts, the spatial wavefunction $\psi(\mathbf{r})$ and the spin part $\chi(\sigma)$, to give the total wavefunction:

$$\Psi_{total}(\mathbf{r}, \sigma) = \psi(\mathbf{r})\,\chi(\sigma)\,. \tag{2.6}$$

Electrons are fermions and consequently, Eq. (2.6) needs to be antisymmetric under exchange of two electrons. As the product of two symmetric (antisymmetric) functions will always yield a symmetric function, $\psi(\mathbf{r})$ needs to be antisymmetric, when $\chi(\sigma)$

is symmetric, and vice versa. As the two electrons are indistinguishable, the two states $(\chi_\downarrow(1), \chi_\uparrow(2))$ and $(\chi_\uparrow(2), \chi_\downarrow(1))$ are identical. For the case of symmetric spin wavefunctions ($\uparrow\uparrow$ or $\downarrow\downarrow$, with the total spin $S = 1$), the total spin wavefunction has to be described by the linear combination. One obtains three spin wavefunctions, hence the name triplet:

$$\begin{aligned}
\chi_1 &= \chi_\uparrow(1)\chi_\uparrow(2), \\
&\qquad \text{with } M_S = m_{s_1} + m_{s_2} = +1 \\
\chi_2 &= \chi_\downarrow(1)\chi_\downarrow(2), \\
&\qquad \text{with } M_S = m_{s_1} + m_{s_2} = -1 \\
\chi_3 &= c\,[\chi_\uparrow(1)\chi_\downarrow(2) + \chi_\downarrow(1)\chi_\uparrow(2)] \\
&\qquad \text{with } M_S = 0.
\end{aligned} \tag{2.7}$$

The spatial wavefunction $\psi(\mathbf{r})$ is symmetric in the ground state, i.e., the state in which both electrons have the same quantum numbers n, l and m_l. Hence, the corresponding spin wavefunctions must have antisymmetric character:

$$\begin{aligned}
\chi^a &= \chi_\uparrow(1)\chi_\downarrow(2) - \chi_\downarrow(1)\chi_\uparrow(2) \\
&\qquad \text{with } M_S = 0.
\end{aligned} \tag{2.8}$$

The antisymmetric spin wavefunction is accompanied by a symmetric spatial wavefunction, yielding an overall singlet state. Dipole transitions between the singlet and triplet systems are generally forbidden due to selection rules in the case of weak spin orbit coupling. This holds true for optical excitations, owing to the bosonic nature of photons, as well as for the subsequent relaxation processes from an intially optically excited state. The latter can, however, gain significant importance in the right circumstances even in the system of low spin orbit coupling such as the molecules under study in this thesis. Accordingly, the transitions from an (excited) singlet to an (excited) triplet state has already been introduced as ISC in Chap. 2.1.3. The rate constants for ISC are typically on the order of $10^3\,\mathrm{s}^{-1}$ to $10^8\,\mathrm{s}^{-1}$ [28].

In molecular dimers and crystals, another process can lead to the population of the triplet state. A singlet exciton can decay to form two triplets of corresponding energy, i.e., if $E_{S1} \geq 2E_{T1}$ holds true:

$$S_1 \rightarrow T_1 + T_1. \tag{2.9}$$

Consequently, the process is named singlet fission (SF) as one singlet exciton fissions into two triplets. SF was first discovered in anthracene single crystals in 1965 [29] but has since also been observed in many other molecular crystals. The development of OPV cells has recently sparked the interest in SF, as it potentially allows to exceed the Shockley-Queisser limit [30]. PEN and PFP, as well as the class of PDIs have proven to be capable of SF. SF has a significant influence on the S_1 states lifetime, as it takes place on an ultrashort timescale ($\approx 10^8$ fs) and thus with rate constants on the order of $10^{11}\,\mathrm{s}^{-1}$, typically leading to a strong quenching of the photoluminescence (PL) intensity and lifetime observed in a time-resolved photoluminescence (TRPL) experiment.

2.1.5 Electronic Coupling

Initially, an optical two-level system is considered in order to introduce the concept of electronic coupling. This lays the theoretical foundation for the description of electron transfer (ET) and excitation energy transfer (EET) processes which can occur in, e.g., molecular D-A complexes.

Coupling of an Optical Two-level System

Next, the electronic coupling between two systems A and B of which either can be in the excited or ground state, respectively, is introduced. The classical analogy is the coupling between two harmonic oscillators, e.g., two coupled pendula through a spring. Details on the computation can be found in standard textbooks on quantum mechanics (see e.g., Ref. [31]). The associated matrix element V describes the coupling potential and is defined as follows:

$$V = \left\langle \psi^{A^*B} \right| \hat{V}_{el}^{AB} \left| \psi^{AB^*} \right\rangle . \tag{2.10}$$

The matrix element V consists of two components: The Coulomb-interaction term V_{Coul} and the exchange-interaction term V_{exc}:

$$V = V_{Coul} + V_{exc}. \tag{2.11}$$

The exchange interaction term V_{exc} depends exponentially on distance due to the link to the overlap of wavefunctions of A and B. Hence, it is responsible for short range interactions and has a significant impact only for interaction distances of $\approx$1 nm. V_{exc} causes triplet energy transfer and electron-transfer reactions. On the other hand, V_{Coul} is proportional to $1/r^2$ (long range interaction) and is the cause of singlet excitation energy transfer (cf. Chap. 2.1.6).

The coupling of an optical two-level system is described in standard textbooks on quantum mechanics as the simplest case of coupling. This concept is commonly described as avoided crossing. The two states can be described in the unperturbed case by their respective eigenfunctions $|\psi_{A,B}\rangle$, and their eigenenergies $E_{A,B}$ as

$$\hat{H}_0 \left|\psi_{A,B}\right\rangle = E_{A,B} \left|\psi_{A,B}\right\rangle . \tag{2.12}$$

The two-system Hamiltonian reads

$$\hat{H}_0 = \begin{pmatrix} E_A & 0 \\ 0 & E_B \end{pmatrix} . \tag{2.13}$$

If one now takes into account an external perturbation (coupling) $\hat{V}$, the modified Hamiltonian $\hat{H}'$ reads

$$\hat{H}' = \hat{H}_0 + \hat{V} = \begin{pmatrix} E_A & 0 \\ 0 & E_B \end{pmatrix} + \begin{pmatrix} 0 & V \\ V^* & 0 \end{pmatrix} = \begin{pmatrix} E_A & V \\ V^* & E_B \end{pmatrix} . \tag{2.14}$$

The perturbation leads to the new eigenfunctions $|\psi_+\rangle$ and $|\psi_-\rangle$ and a splitting of the energy levels at the point of intersection. The corresponding eigenenergies are

$$E_{\pm} = \frac{1}{2}(E_A + E_B) \pm \frac{1}{2}\sqrt{(E_A - E_B)^2 + 4|V|^2}. \tag{2.15}$$

If one makes the following substitutions in Eq. (2.15)

$$\begin{aligned} E_0 &= \frac{1}{2}(E_A + E_B), \\ \Delta &= \frac{1}{2}(E_A - E_B). \end{aligned} \tag{2.16}$$

the new eigenenergies read

$$\begin{aligned} E_{\pm} &= E_0 \pm \sqrt{\Delta^2 + 4|V|^2}, \\ \Delta_{\pm} &= |E_+ - E_-| = 2 \cdot \sqrt{\Delta^2 + 4|V|^2}. \end{aligned} \tag{2.17}$$

From Eq. (2.17), one immediately sees that the absolute energy E_0 has no effect on the splitting of the new states. A variation of E_0 only shifts the zero point energy. A plot of E_A, E_B, E_+ and E_- as function of the splitting Δ is shown in Fig. 2.3. According to Eq. (2.16) E_A and E_B are lines with slopes of $+1$ and -1, respectively. One finds hyperbolic curves for E_+ and E_-, which asymptotically approach the original unperturbed energy levels. It becomes evident that even for the case of $E_A = E_B$ (degeneracy) the splitting is no longer zero.

For the corresponding eigenstates one can compute

$$\begin{aligned} |\psi_+\rangle &= \cos\frac{\Phi}{2} \cdot \left|\psi^{A^*B}\right\rangle + \sin\frac{\Phi}{2}\left|\psi^{AB^*}\right\rangle, \\ |\psi_-\rangle &= -\sin\frac{\Phi}{2} \cdot \left|\psi^{A^*B}\right\rangle + \cos\frac{\Phi}{2}\left|\psi^{AB^*}\right\rangle, \\ \tan\Phi &= \frac{|V|}{\Delta}. \end{aligned} \tag{2.18}$$

It is obvious that for $|V| \gg \Delta$ (strong coupling limit), $\Phi \simeq \pi/2$ and the eigenstates of the perturbed system can be described by linear combinations of those of the uncoupled

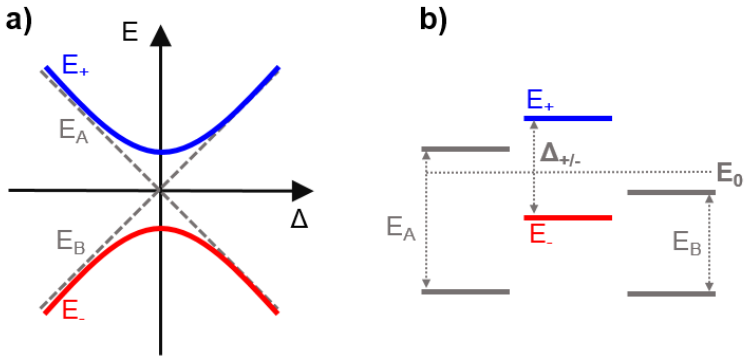

Figure 2.3: The pertubartion V leads to an lifting of the degeneracy of the energy levels for $E_A = E_B$. A quantum mechanical avoided crossing lifts the degeneracy and induces the an energy level splitting $\Delta_{\pm}$.

states. When $|V| \ll \Delta$ (weak coupling limit), then $\Phi \simeq 0$ and the system can be described by the individual unperturbed eigenstates.

In general however, $|\psi_{A,B}\rangle$ are no longer the eigenstates of the modified Hamiltonian $\hat{H}'$. As a consequence of this, they are no longer stationary states. If one now measures the system to be in the state $|\psi_A\rangle$ at $t = 0$, there is a certain probabilty of finding the system in the state $|\psi_B\rangle$ at later times $t > 0$. The perturbation V thus induces a finite transition rate between the two unperturbed states.

Indeed, the aformentioned also has some "practical" relevance regarding the benzene molecule introduced in Chap. 2.1.1 The quantum stabilization of benzene is one of the most fundamental examples of this phenomenon. As already illustrated above, in the benzene molecule, the six carbon atoms are located at the vertices of a hexagon. One would expect the electronic ground state of the molecule to consist of three double bonds between neighboring atoms, whereas the other three bonds would be single ones. The two different possible configurations are given in Fig. 2.1(a), (b) and are described by the wavefunctions $|\phi_A\rangle$ and $|\phi_B\rangle$. By symmetry it is fair to assume that $\langle\phi_A|\,\hat{H}\,|\phi_A\rangle = \langle\phi_B|\,\hat{H}\,|\phi_B\rangle$, which allows conclusion that the ground state is doubly degenerate. However, the off-diagonal matrix element $\langle\phi_B|\,\hat{H}\,|\phi_A\rangle$ is non-zero. This coupling between the two states gives rise to an energy level below E_m and, therefore, constitutes the true ground state of the benzene molecule. Thus, the total energy of the molecule is lowered and it is more stable than initially expected. Moreover, as the ground state is represented by a linear combination of $|\phi_A\rangle$ and $|\phi_B\rangle$, it cannot be

represented by either Fig. 2.1(a) or Fig. 2.1(b). This is why the representation shown in Fig. 2.1(c) is chosen, manifested by the term "delocalization".

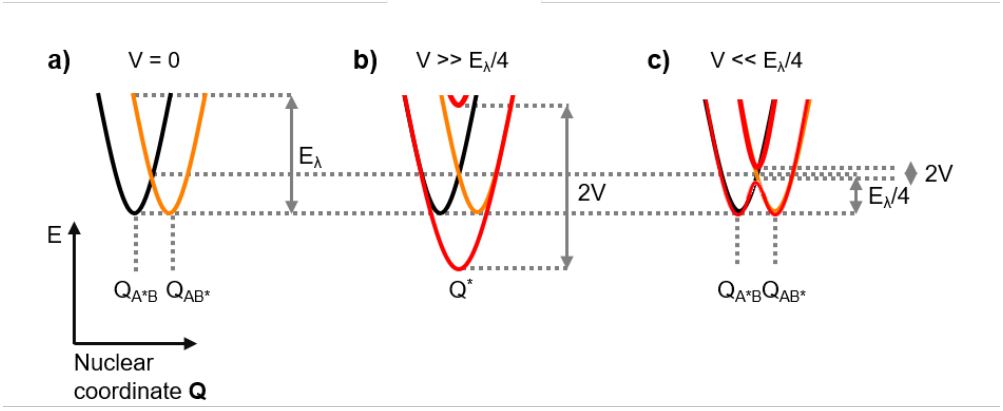

Figure 2.4: (a) The reorganization energy E_λ is a measure of the conformational change when a molecule makes an electronic transition, e.g., between the ground and excited state. In the case of strong coupling, the two individual potentials are replaced by an entirely new potential (red curve) and a new equillibrium co-ordinate $\mathbf{Q}^*$ (b). (c) In the case of weak coupling the resulting potential shows a splitting in the vicinity of the crossing point but the two equillibrium co-ordinates $\mathbf{Q_{A^*B}}$, $\mathbf{Q_{AB^*}}$ remain local minima.

Coupling Regimes and Wavefunction Localization

It is useful to make a distinction between different degrees of coupling strength. This distinction is made by comparing the coupling strength V to the reorganization energy E_λ which is a measure for the energy related to the changes in geometry when making an electronic transition, e.g., from the ground state to an excited state. The degrees of coupling stength have been classified into three regimes:

1. The "strong" coupling regime: The coupled system shows a total loss of the vibrational structure with regard to the individual constituents. The coupling is so strong that a new adiabatic potential curve is formed, accompanied by a red- or blue-shift of the optical transistions. An example for this regime is given by molecular dimers and excimers.

2. The "intermediate" regime: The individual chromophores' vibrational structure is retained. The delocalization is caused not by the electronic part Ψ_{el} of the total

wavefunction but by the nuclear part, χ_N, responsible for the vibrational structure of the molecule. However, depending on the orientation of the molecules, red- or blue-shifts of the spectra can occur. The former is known as J- and the latter as H-aggregatation. Both cases can be viewed as extreme cases of the so-called Davydov-splitting.

3. The "weak" coupling regime: The optical spectra of the combined system resemble the incoherent sum of the individual constituents. The individual vibrational structures are retained. Thus, a Fermi's golden rule (FGR) approach is valid. This case describes incoherent energy transfer. Incoherent energy transfer processes can be divided into EET and ET, respectively. These two concepts will be discussed in the following sections.

It should be noted that the above classification was originally developed by R. L. Fulton and M. Gouterman [32] for the case of two identical chromophores interacting with one another. It is, however, also applicable in hetero-molecular systems or to the coupling between two states (e.g., between an excited state and a cationic state) of one single chromophore.

2.1.6 Excitation Energy and Electron Transfer Processes

ET as well as EET processes are driven by similar electron-electron and electron-vibration interactions. The mathematical formalisms describing both are also similar. Transition probabilities are calculated in the framework of first order perturbation theory adopting a FGR form. In turn, the theories initially formulated by R.A. Marcus [33] or Th. Förster [34, 35] are realizations of such a FGR expression. The transition rate k_{if} for a system to transfer from an initial state $|i\rangle$ to a quasi-continuum of states $|f\rangle$ is given by first order perturbartion theory in the limit of a weak perturbation (coupling) by

$$k_{if} = \frac{2\pi}{\hbar} \left| \langle \Psi_i | \, \hat{V} \, | \Psi_f \rangle \right|^2 \rho(E_f), \tag{2.19}$$

where $V_{if} = \langle \Psi_i | \, \hat{V} \, | \Psi_f \rangle$ is the matrix element of the pertubartion operation belonging to the corresponding transition, which was already treated by Eq. (2.11). $\rho(E_f)$ de-

notes the density of states (DOS) at the final state energy. For theoretical approaches introduced in the following, the "weak" coupling regime applies ($V \ll \lambda/4$). This implies that for all considerations the Born-Openheimer approximation remains valid and electronic and nuclear co-ordinates may be separated. Eq. (2.19) factorizes into an electronic and a nuclear part and then reads:

$$k_{if} = \frac{2\pi}{\hbar} \underbrace{|V_{if}|^2}_{\text{electronic}} \cdot \underbrace{FCWD}_{\text{nuclear}}. \tag{2.20}$$

Here, $FCWD$ denotes the Franck-Condon weighted density of states. It constitutes the thermally-averaged sum of vibrational wavefunction overlap in the initial and final states, respectively. It is essentially the nuclear contribution to the transfer rate.

Charge-Transfer Processes in Molecular D-A Systems: The Marcus Model

In an ET process, an electron is transferred from a D to an A. The reaction scheme is thus

$$D + A \rightarrow D^+ + A^-.$$

The Marcus model of ET describes the non-adiabatic (="weak" coupling) regime. It describes ET reactions in which no chemical bonds are formed or broken, the latter situation being covered by Eyring's transition state theory. Here, the quantum-mechanical description of the model will be given, while it can be derived in a classical manner, yielding the exact same result. In the high-temperature limit ($h\nu_i << k_BT$), all vibrational modes ν_i are thermally excited. In this case the $FCWD$ obeys the expression:

$$FCWD = \sqrt{\frac{1}{4\pi k_B T E_\lambda}} \exp\left\{-\frac{\Delta G^{\neq}}{k_B T}\right\}. \tag{2.21}$$

where E_λ is the reorganization energy and $\Delta G^{\neq}$ is the Gibbs free energy of activation. R.A. Marcus derived for $\Delta G^{\neq}$ [33]:

$$\Delta G^{\neq} = \frac{\left(\Delta G^0 + E_\lambda\right)^2}{4E_\lambda}. \tag{2.22}$$

Combining Eqs. 2.20-2.22 one obtains the full expression

$$k_{if}^{M} = \frac{2\pi}{\hbar}|V_{if}|^2\sqrt{\frac{1}{4\pi k_B T E_\lambda}}\exp\left\{-\frac{\left(\Delta G^0 + E_\lambda\right)^2}{4E_\lambda k_B T}\right\}. \tag{2.23}$$

According to Eq. (2.23) and, thus, to Marcus theory, the ET rate depends on the following factors:

1. The distance between the D and A: due to the dependence $|V_{if}|^2$, k_{if}^M; will generally decrease exponentially with increasing D-A distance. However, the nuclear contribution ($FCWD$) can also show a distance dependence in the Marcus theory, thus yielding a more intricate overall behavior of k_{if}^M.

2. The Gibbs free energy of reaction: The energy reduction when the system is transferred from the initial to the final state. It is defined as potential energy difference $\Delta G^0 = G_f - G_i$, where G_i and G_i are the Gibbs energies of the initial and final state of the ET reaction. Thus, a more negative value implies a large energy loss.

3. The reorganization energy: the energy cost incurred by molecular rearrangements of D, A and surrounding medium during the ET process. Illustrated in Fig. 2.4.

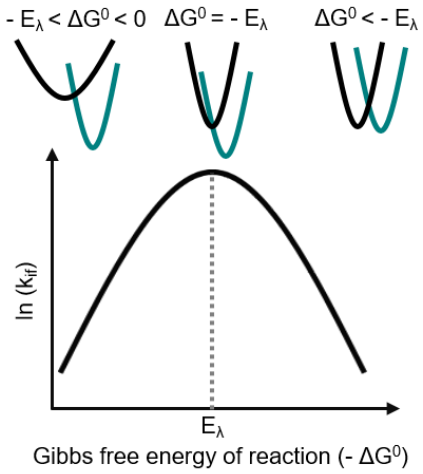

Figure 2.5: Plot of the dependency of the ET rate k_{if} on the change of the Gibbs free energy $-\Delta G^0$. Eq. (2.22) gives rise to the parabolic shape.

Additionally, the ET rate's dependence on ΔG^0 can be divided into three distinct regimes (cf. Fig. 2.5):

1. The normal regime where k_{if}^{M} increases with increasing driving force ΔG^0.

2. An activationless regime where k_{if}^{M} peaks. This regime is reached when $\Delta G^0 \simeq -E_\lambda$ and thus $\Delta G^{\neq} \simeq 0$.

3. The inverted regime where $-E_\lambda < \Delta G^0$ and hence k_{if}^{M} is reduced for increasing ΔG^0.

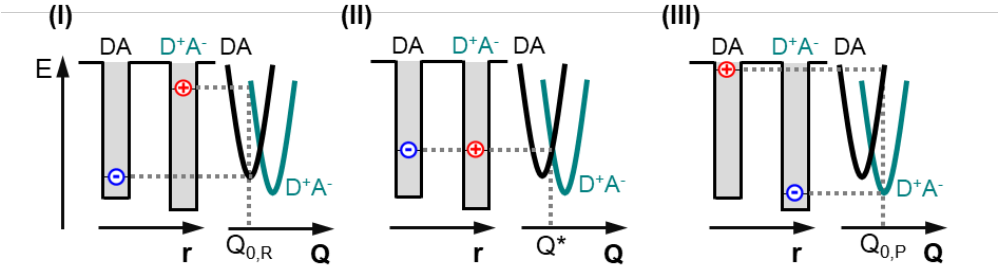

Figure 2.6: ET process illustrated by showing the correspondence between the electronic (on the l.h.s. of each panel) and the nuclear energy levels (on the r.h.s.), respectively. (I) At the initial nuclear configuration $Q_{0,R}$, the lowest unoccupied energy level of the D^+A^- (denoted by a red circle) is too high in energy. (II) At Q^*, both energies become degenerate and electron transfer occurs by tunnelling through the barrier. (III) The equillibrium configuration of the D^+A^- is the counterpart of the situation shown in (I). Adapted from Ref. [25].

The correspondence between the electronic energy levels and the nuclear energy levels is illustrated in Fig. 2.6. Fig. 2.6 helps understand the importance of nuclear rearrangement for the ET process, in order for electronic energies to become degenerate and electron tunneling to become energetically feasible. It is obvious that an ET can only occur after thermal fluctuations bring the geometry of the system to the equillibrium co-ordinate Q^*. Alternatively, this can be done by optical excitation with excess photon energy, which in turn is converted to vibrational energy.

Typically, in a molecular D-A complex, the D^+A^- state infers that electron and hole are localized the different moieties of a molecular complex. For this, it is also referred to as charge separated state (CSS). In the case of, e.g., D-A heterostructures, the expression CT state is usually preferred.

Determination of Gibbs Free Energy ΔG^0

The Gibbs free energy ΔG^0 of a CT process gives the potential energy difference between the intial and the final states in a reaction. As ΔG^0 it enters in Eq. (2.23), which describes the rate constant of a charge transfer within the framework of Marcus theory, it is important in revealing the microscopic mechanisms of the charge transfer process. The following equation is commonly employed to estimate ΔG^0 [36]:

$$\Delta G^0 = \underbrace{E_{ox} - E_{red}}_{=\Delta_{redox}} - E_{(0,0)} \underbrace{- \frac{e^2}{(4\pi\epsilon_0\epsilon_s R_{ee})}}_{=E_C} \underbrace{- \frac{e^2}{(8\pi\epsilon_0)} \left(\frac{1}{r+} + \frac{1}{r-}\right) \left(\frac{1}{\epsilon_{ref}} - \frac{1}{\epsilon_s}\right)}_{\text{Correction term accounting for differences in } \epsilon}. \quad (2.24)$$

Here, $\mathrm{E_{red}}$ is attributed to the first reduction potential and $\mathrm{E_{ox}}$ to the first oxidation potential. Together they give the redox potential Δ_{redox}. $\mathrm{E_{0,0}}$ is the energy of the $S_1 \rightarrow S_n$ transition, which is taken from the spectroscopic measurements as the center of gravity between the lowest energy absorptive and highest energy PL features, respectively. $\mathrm{R_{ee}}$ corresponds to the edge-to-edge distance of the charge D and A and is thus key to the magnitude of the Coulomb energy E_C. The last term of Eq. (2.24) is introduced to correct for deviations between the solvents used in, e.g., cyclic voltammetry (CV) and optical measurements $r+$ and $r-$ mark the respective ionic radii. Eq. (2.24) is given relative to the S_1 state energy.

Δ_{redox} can be obtained experimentally, by performing either photoelectron spectroscopy (PES) or CV measurements, respectively. In the isolated molecule and in absence of intermediate energy levels, the optically measured $E_{0,0}$ transition energy[1] matches Δ_{redox}. Consequently, Δ_{redox} is sometimes referred to as the electrochemical bandgap. In turn, deviations between the values are indicative of intermediate states, which can be related to, e.g., (electron) D groups.

[1] which are exclusively $\pi - \pi^*$-excitations in the class of materials studied in this thesis

Excitation Energy Transfer: Förster Theory

The concept and theoretical description of EET processes dates back to the work of Th. Förster [34, 35]. In the Förster theory of EET, a

$$D^* + A \rightarrow D + A^*, \tag{2.25}$$

reaction, transferring excitation energy from the D to the A takes place. The main achievement of Förster's work is in linking the analytical expression to entities which are determinable experimentally. Förster derived a rate constant for an non-radiative EET from the FGR expression [Eq. (2.19)] by approximating the Coulombic part of the pertubation operation through a dipole-dipole term.

$$\begin{aligned} k_{if}^F &= \frac{2\pi}{\hbar}\left[\frac{|\vec{\mu_i}|\cdot|\vec{\mu_f}|}{\epsilon r^3}\Gamma\left(\theta_i,\theta_f\right)\right]^2 \cdot J_F, \\ &= \frac{2\pi}{\hbar}\frac{\Gamma^2\eta}{r^6\tau_i}\cdot J_F. \end{aligned} \tag{2.26}$$

Here, Γ^2 is the dipole orientation factor, which can be approximated as $\Gamma^2 = 2/3$ for a random distribution of dipoles, e.g., for molecules in solution. η is the PL quantum yield (PLQY) which will be introduced in Chap. 3.4, r denotes the distance between the two interacting partners, and τ_i is the native (i.e., when no As are present) excited state lifetime of the D.

Förster linked the $FCWD$ term to the emission and absorption spectra of the D and A, respectively, yielding the spectral overlap integral J_F, which can be computed as

$$J_F = \frac{\int f_D\left(\lambda\right)\epsilon_A\left(\lambda\right)\lambda^4 d\lambda}{\int f_D\left(\lambda\right)d\lambda}, \tag{2.27}$$

with the normalized D emission spectrum, $f_D\left(\lambda\right)$, and the A absorption spectrum (in $\mathrm{Lmol^{-1}cm^{-1}}$), $\epsilon_A\left(\lambda\right)$. From this, the so-called Förster radius R_0 can be derived, which is defined as the D-A distance for which the EET efficiency amounts to 50 %:

$$R_0 = 0.221 \left(\frac{\Gamma^2 \eta}{n^4} J_F \right)^{(1/6)} . \tag{2.28}$$

Eq. (2.26) is applicable to all dipole-allowed electronic transitions. Hence it is the description of singlet-singlet EET. The transfer decays with r^{-6}. ET processes which are due to the exchange interaction part of the coupling matrix element $|V_{if}|^2$ are described by the Dexter theory.

2.2 Electronic Excitations in Molecular Crystals

Certain characteristic effects take place when going from the single molecule to individual molecules and finally to the solid. In general, the eigenstates of the constituting atoms or molecules are no longer valid and must be replaced by by states complying to the collective excitations of the crystal. The discrete energy levels of the atoms/molecules and are replaced by the formation of the electronic bands, respectively. However, owing to the comparably low intermolecular forces in molecular solids, their optical spectra are still derived from those of the individual molecules. Generally, one observes the following differences when making the transition to the condensed phase:

- **Solvent shift**: Describes the shift of energy levels, usually toward lower energies. This is caused by interaction with the neigbouring molecules, e.g., in solution with the solvent molecules. The magnitude of the shift is generally different for the different molecular states.

- **Line broadening**: The discrete molecular levels are broadened in the solid, leading to excitonic bands. This is a consequence of the periodic potential in a (crystalline) solid where excitation energy is delocalized over more than one lattice site.

- **Lifting of degeneracies and breaking of selection rules**: Transitions which are forbidden in the individual molecule may become (partially) allowed in the solid. Here, the symmetry of the entire crystal and no longer solely that of the molecule is the determining factor.

- **Davydov splitting**: Describes a splitting of each molecular level into Z terms in the solid. Here, Z is the number of translationally invariant molecules in the unit cell. Resonant interaction between the molecules leads to a splitting on the order of a few cm^{-1} to several thousands of cm^{-1}. Davydov splitting shows, e.g., as two distinct transitions depending on the polarization of the incident light.

2.2.1 Frenkel Excitons

In the solid, an entirely new type of excitation emerges, in addition to the effects mentioned above. Due to Coulomb attraction, excited charge carriers, that is electrons and holes, can form correlated pairs, so-called excitons. Their mutual attraction lowers the total energy of the system, such that the exciton is frequently the lowest energy excitation found in optical experiments on crystalline solids.

Depending on the correlation length of electron and hole, three distinctions are made to classify excitons. The situation is schematically sketched in Fig. 2.7. Frenkel excitons have the largest binding energy which can reach 1 eV or more. Here, the excitons are commonly localized on one lattice site. The other extreme is given by the Wannier exciton with binding energies in the low meV range. This, in turn, leads to a very delocalized nature of this type of excitons, with Bohr radii as large as 10 nm. The intermediate case is that of the so-called CT exciton. As only excitations related to Frenkel and CT excitons will be dealt with in this thesis, the description of Wannier excitons is omitted in the following.

As shown in Fig. 2.7, the Frenkel exciton corresponds to an excitation which is localized on one lattice site. The considerable binding energy results from the fact that van der Waals interactions are weak, which in turn infers weak Coulomb-screening of charges. Along with the greatly reduced dielectric constants in molecular solids, compared to inorganic crystals, the Coulomb attraction between the electron and hole grows to the reported values. For electrons and holes to be able to move freely throughout the crystal as independent entities, they must be promoted to a state in which the HOMO and LUMO of two distant molecules are each singly occupied by a hole and an electron, respectively. Such an excitation can be viewed as the organic equivalent of the valence and conduction bands of an inorganic semiconductor. However, the correlated

electron-hole pair can move through the crystal as a whole, typically by hopping-like transport.

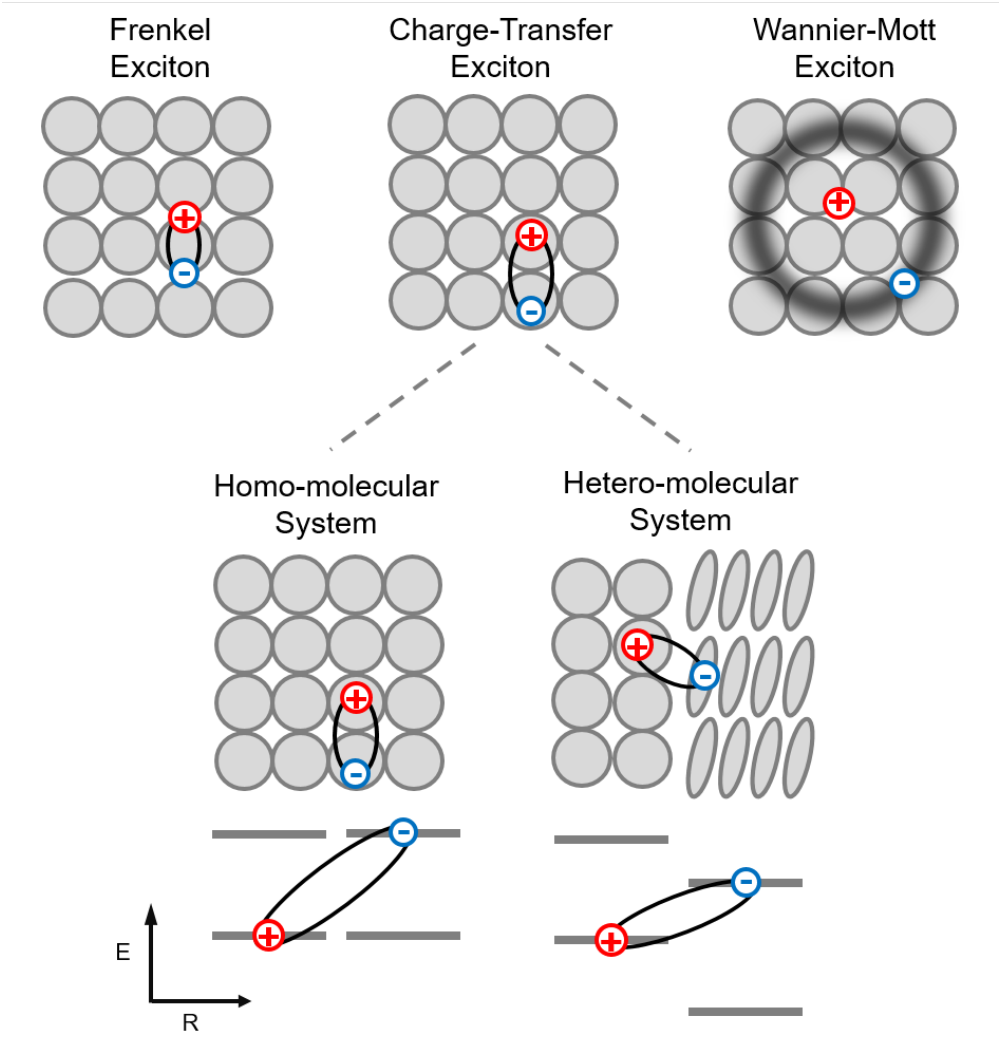

Figure 2.7: On the l.h.s. the situation of the Frenkel exciton localized to one molecule is shown. The other limit, that of the Wannier exciton is shown on the r.h.s. Here, electron and hole can be separated by a distance many times the lattice constant. In the middle, the intermediate case of the CT exciton is shown.

Now, a molecular crystal with two molecules in the unit cell, e.g., the PEN and PFP crystals studied in this thesis, is considered. Such a pair of molecules gives a physical dimer and is sometimes referred to as a mini-exciton in the optically excited state [22]. The ground-state wavefunction and energy of the dimer are given by

$$\Psi_{total} = \psi_A \psi_B \qquad \text{and} \qquad E_G = 2E_0. \tag{2.29}$$

Now, it is assumed that one of the molecules is promoted to an excited state Ψ^* with the energy E^*. The probability of finding either one of the molecules in the excited state is equal. Consequently, the total wavefunction Ψ^*_{total} is given by the linear combination

$$\Psi^*_{total} = \frac{1}{\sqrt{2}} \left(\psi_A \psi^*_B \pm \psi^*_A \psi_B \right). \tag{2.30}$$

The energies of the dimer are $E^*_+ = E^*_- = E_0 + E^*$ in the non-interacting case. This situation is illustrated in Fig. 2.8(a). However, if the interaction $V_{A,B}$ becomes non-zero, the energy degeneracy will be lifted. The theoretical description of this case resembles the situation of quantum mechanical anti-crossing introduced in Chap. 2.1.5, Eqs. (2.10)-(2.18), for the case of degenerate energies ($E_A = E_B$). The matrix element V_{AB} describes the the resonant exchange of excitation energy between the molecules and is given as:

$$V_{AB} = \langle \psi^*_A \psi_B | \, \hat{V}_{AB} \, | \psi_A \psi^*_B \rangle \, . \tag{2.31}$$

For the excited dimer case, the new eigenenergies now read:

$$E^*_\pm = E^* + E_0 \pm V_{AB}. \tag{2.32}$$

Hence, the energy splitting amounts to $2V_{AB} = \Delta_d$. The quantity Δ_d is known as the Davydov splitting. Besides the resonance interaction, also the Coulomb interaction between the (altered) charge distribution of molecule A in the excited state and molecule B in the ground state (and vice versa) has to be accounted for. It amounts to

$$D^* = \langle \psi^*_A \psi_B | \, H_{AB} \, | \psi^*_A \psi_B \rangle = \langle \psi_A \psi^*_B | \, H_{AB} \, | \psi_A \psi^*_B \rangle \, . \tag{2.33}$$

Already in the ground state there is Coulomb interaction, which consequently is given by:

$$D_0 = \langle \psi_A \psi_B | \, H_{AB} \, | \psi_A \psi_B \rangle \, . \tag{2.34}$$

Here, D_0 is identical to the van der Waals binding energy of the molecules in the crystal. The sum $D = D^* - D_0$ typically has a positive sign and actually resembles the "solvent shift", that is the red-shift of optical transitions compared to the solvated molecule. The effects of the performed calculations are schematically shown in Fig. 2.8(b).

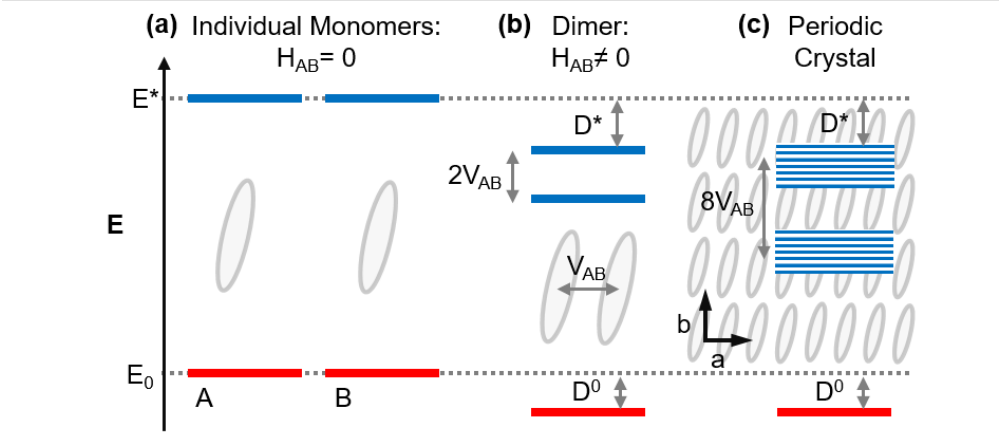

Figure 2.8: (a) Energy levels for a pair of uncoupled monomers, (b) a crystal where only the two molecules in the unit cell are taken into account, giving a physical dimer, and (c) the situation in which the full crystal periodicity is taken into account. In the crystal the splitting increases to $n \cdot 2V_{AB}$ for the n translationally inequivalent nearest neighbors. Adapted from Ref. [22].

To account for the periodicity of a crystal, the dimer picture has to be extended. Again, the case of a crystal with two molecules in the unit cell is considered. In this case, the ground-state wavefunction is the direct product of the ground state of the individual molecules $\psi_{m,\alpha}$:

$$\Psi_G = \mathcal{A} \prod_{m,\alpha}^{N} \psi_{m,\alpha}. \tag{2.35}$$

Here, $\mathcal{A}$ is an antisymmetrisation operator, ensuring that the total wavefunction is antisymmetric. m runs over N units cells in the crystal while the indices α and β run over the two (in the case considered here) molecules in the unit cell. If a localized electron-hole pair excitation at the α site of the n-th unit cell is considered, while all other molecules remain in the ground state, the wavefunction yields:

$$\Psi^*_{n,\alpha} = \mathcal{A}\psi^*_{n,\alpha} \prod_{n,\alpha \neq m,\beta} \psi_{m,\beta}. \tag{2.36}$$

It is important to note, that these wavefunctions are not eigenfunctions of the crystal Hamiltonian. A Bloch-wave ansatz delivers a wavefunction appropriate to the crystal symmetry and periodic potential. From Eq. (2.36), the delocalised wavefunction can be obtained as:

$$\Psi^*_{\alpha}(\mathbf{k}) = \frac{1}{\sqrt{N}} \sum_n \Psi^*_{n,\alpha} \exp(i\mathbf{k}\mathbf{R}_{\mathbf{n},\alpha}), \tag{2.37}$$

where Ψ^* is the local exciton wavefunction $\mathbf{R}_{\mathbf{n},\alpha}$ is the position vector of the molecule. This approach takes into account the fact that all electronic excitations must be partially delocalized, because the incident photon is delocalized according to its finite wavelength. In the case of zero coupling all states differing in $\mathbf{k}$ would be degenerate. In general, the coupling in an organic crystal is weak. However, it is non-zero and consequently and leads to non-negligible (exciton) band dispersion and the Davydov splitting mentioned earlier. The band dispersion is typically highly anisotropic due to the intrinsic anisotropy of most molecules leading to a strongly varying electronic coupling for different crystalline axis. For a detailed theoretical treatment of this particular matter, the reader is referred to textbooks and review articles [22, 37].

2.2.2 Charge-Transfer Excitons

The regime intermediate to the two limiting cases of highly-localized Frenkel- and delocalized Wannier-excitons is that of CT excitons. This term is applied to electronic excitations in which the electron-hole separation is larger than the molecular structural units. As electron and hole are localized and different molecules, the state has, at least partially, ionic character. This is why they have been referred to as ion pair states in the past.

As indicated in Fig. 2.7, this type of excitation is found in homo-molecular crystals, i.e., consisting of only one type of molecule, as well as in hetero-molecular ones. In the former, the excitations are intermediate to the respective energies of lowest-lying Frenkel excitons and the localized $S_n \rightarrow S_0$ transitions. This renders them hard to observe, as especially the $S_n \rightarrow S_0$ transitions frequently have very large oscillator strengths. However, their polar character makes CT-transitions subject to the Stark

effect. Hence, an electroabsorption measurement, where a modulated DC electric field is applied to the crystal, can reveal the nature of optical transition.

In addition to CT states in homo-molecular crystals, they can also appear in hetero-molecular systems. In this scenario, one of the two constituents typically acts as electron donor, while the other is an acceptor. The hetero-systems can consist of mixed crystals of alternating structure with a DADA stacking order. Such mixed crystals can be grown in different D:A ratios. Alternatively, phase-separated crystals can be grown. Here, there exists only a narrow internal interfacial region in which the two phases are in direct contact. Ideally, this internal interface is molecularly smooth, with no mutual intercalation between molecules of the respective phases. Both crystal types are the subject of this thesis. As can be seen schematically in the bottom part of Fig. 2.7, CTs of this second type are frequently the lowest-energy transitions of the singlet subsystem.

CT systems are both scientifically interesting as well as potentially technologically relevant. First, CT states are being discussed as precursors to charge separation. charge separation (CS) is relevant for OPV, as here electron and hole must be efficiently separated to allow a current to flow. In this regard, D-A systems such as the PEN-PFP and PEN-C_{60} are promising candidates for potential device applications. Besides, they can be utilized as model-systems for the study of internal interfaces. Here, especially the coupling of molecules in the interfacial region is of great interest. Generally, the coupling is expected to be in the weak regime, rendering unperturbed D and A MOs, respectively.

3 Experimental Details

Te following chapter illustrates in detail the experimental techniques carried out within this thesis. The description includes the setups for linear aborption and continous wave (CW) PL, TRPL, photoluminescence excitation (PLE) and PLQY, respectively.

3.1 Linear Absorption

Linear absorption measurements are used to measure dipole-allowed transitions between the occupied states and the unoccupied states. In terms of molecular spectroscopy, this corresponds to the HOMO - LUMO transition. Additionally, higher states, e.g., LUMO+1, LUMO+2, etc. are also probed. In the case of molecular solids, the excitons corresponding to the HOMO-LUMO transition might also be observed.

Different experimental setups were used to the obtain the data presented in this thesis. For measurements of individual molecules in solution, a commercially available instrument[1] is used. Here, two different light sources, a tungsten halogen and an Xenon arc lamp, are used to cover a spectral range of 1.38–6.2 eV (200–900 nm).

When lateral resolution was of no issue, the same experimental arrangement as described in Chap. 3.3 was used. A standard 50 W tungsten halogen lamp is imaged onto a pinhole of 100 µm diameter. The pinhole, in turn, is imaged at a 1:1 magnification onto the sample surface. The same detection scheme as in the PLE setup is used. The different techniques all have in common the method of data processing. To measure the absorption (or absorbance), three separate measurements must be performed. A

[1] "Cary 3 UV-VIS Spectrophotometer", Varian

background measurement, to correct for scattered light reaching the detector, a reference measurement, which gives the 100 % transmission baseline and finally the actual sample transmission spectrum. The absorption A is given by

$$A = 1 - T - R. \tag{3.1}$$

A is computed from the sample's transmission spectrum, T_S, a reference spectrum T_R, typically the respective substrate without any coverage, and a background measurement I_{BG} to account for stray-light and dark-current of the detector:

$$A = 1 - \frac{T_S - I_{BG}}{T_R - I_{BG}}. \tag{3.2}$$

The reflection R is neglected and assumed add a constant (but small) offset across the wavelength region of interest. In molecular spectrocpy of dissolved samples, the molar exctintion coefficient ϵ is commonly used. ϵ is defined as

$$\epsilon = \frac{A}{c \cdot d}, \tag{3.3}$$

where c is the molar concentration (measured in $mol \cdot L^{-1}$) and d is the optical path length (for samples in liquid solution typically the length of cuvette).

3.2 Time-Resolved Photoluminescence Spectroscopy

In contrast to linear absorption, the occupation density of emissive states is monitored in PL spectroscopy. The concert of the two methods typically yields a shift of the emission maximum towards lower energies, with respect to the absorption maximum. This effect is known as the Stokes shift, which forms an important material parameter. A time-resolved photoluminescence experiment adds information on the relaxation dynamics of the emissive states. For systems in which more than one radiative decay channel exists, transient PL data can be used to indentify individual channels by their characteristic decay behavior. In general, the measured decay always incorporates the

superposition of radiative and non-radiative channels. Furthermore, changes in the behavior are often indicative of newly introduced (non-radiative) decay channels.

3.2.1 Experimental Setup

The experimental setup used to acquire time-resolved data can the subdivided into three different sections: excitation, microscope and detection sections respectively. A tunable titanium:sapphire laser[2] pumped by a frequency-doubled Nd:YVO laser[3] is used as excitation source. It provides tunable excitation energies ranging from 1.13–1.77 eV (700–1100 nm) with an maximum power of 3 W. In the configuration employed in this experiment, the pulse length of the emitted radiation is on the order of 100 fs at a repetition rate of $((79.0 \pm 0.1)\,\mathrm{MHz})$ MHz. This corresponds to a separation of approximately 12.8 ns between two consecutive pulses. To extend the range of excitation wavelengths, a frequency doubling and tripling unit is employed, providing near-continouus excitation from 1.13–4.96 eV (250–1100 nm). This enables resonant excitation of a broad range of different materials. The system is designed in an all-reflective configuration to ensure minimum temporal pulse distortion. The use of reflective optics also guarantees low loss of excitation power throughout the entire range of excitation wavelengths. The excitation light is coupled to the microscope section via a periscope and a beamsplitter with a transmission:reflection ratio of 70:30. The ratio of the beamspliter is chosen as the emitted light level is usually the limiting factor of detection sensitivity while at the given ratio an excitation power of up to 100 mW is still available under optimum cirumstances. The microscope is operated in a confocal manner, ensuring excitation and detection pathways are in focus simultaneously. Again, all-reflective optics are used in the Schwarzschild microscope objective. The operator benefits from the long working distance ($w_d = 17.6\,\mathrm{mm}$). Through the high numerical aperture ($NA = 0.5$) near-diffraction-limited spot sizes of 5 µm are achieved. The sample itself is mounted in a He-flow cryostat to allow measurements under cryogenic conditions. Temperatures as low as 4 K can be achieved while the unit of resistive heater and PID controller allows temperature-dependent measurements up to temperatures of 320 K at approximately 0.1 K precision. As previously mentionend, the objective is also used to collect the light emitted from the sample. The emitted light

[2] "Tsunami", SpectraPhysics
[3] "Millenia eV", SpectraPhysics

again passes the beamsplitter and finally passes through the sole transmissive optic in the setup, the focussing lense which images the sample surface onto the spectrometer slit. A beamsplitter can mounted between focussing lense and spectrometer entrance which guides the light to a camera. By this way, the position of the excitation light on the sample can be measured. Additionally, through the installed motorized xy-scanning stage, the entire sample can be scanned automatically and measured spectra can be correlated to the respective areas on the sample surface.

The detection section consists of a grating spectrometer[4] with a focal length of $f = 260\,\mathrm{mm}$. A grating turret with three gratings installed simultaneously offers the choice between broad spectral acquisition window and high resolution in different spectral regions. The highest resolution obtained is approximately 0.1 nm. The dual exit-port configuration with a motorized mirror enables rapid switching between to different detectors. For time-integrated measurements, a high-sensitivity thermoelectrically-cooled silicon CCD[5] is used. It high sensitivity facilitates the detection of low light levels. A low dark-current and noise level is achieved by cooling the detector to temperatures as low as $-60\,^{\circ}\mathrm{C}$. For time-resolved measurements, a "synchro-scan" Streak Camera[6] is attached to the second exit port of the spectrograph.

The operation principle of a streak shall be explained in-depth. Photons exciting the spectrograph are spectrally dispersed in its image plane. The entrance optics of the Streak camera images the light passing through the horizontal entrance slit onto a photocathode (S20). Through the photo-electric effect electrons are released instantaneously. By this, not only the horizontal distrubution corresponding to the specific wavelength of the impinging photons is conserverd. Additionally, the temporal order in which electrons are released corresponds to the temporal order of the incident photons. The emitted electrons are accelerated through a vacuum tube. During their passage through the center of two capacitor plates to which a sinusoidally modulated high voltage is applied. By means of a trigger signal from the laser source the phase and frequency of the modulation voltage are locked to those of the laser. The limit for temporal window is given by the segment of the sine is an good approximation described by a linear function. Generally speaking, the temporal resolution is limited by different factors: The pulse-length of the exciting laser light, the width of the horizontal entrance

[4] "Cornerstone 74068", Newport/Oriel
[5] "iDus BV-440BU", Andor Technologies
[6] Hamamatsu Photonics

slit, the electron optics in the sreak unit, and ultimatively by Heisenberg's uncertainty relation. On the other hand, the maximum time window is firstly limited by the linear region of the sinus function and secondly by time window (≈12.8 ns) between two consecutive excitation pulses.

In this work, a the majority of measurements where performed on molecules dissolved in various solvents. To facilitate the measurements and allow the use of standard cuvettes (12.5 mm × 12.5 mm cross-section), a drop-in module was constructed. The module houses its own focussing/collimation optics, the cuvette holder itself and a beam-dump to absorb excitation light passing through the cuvette without being absorbed by the sample.

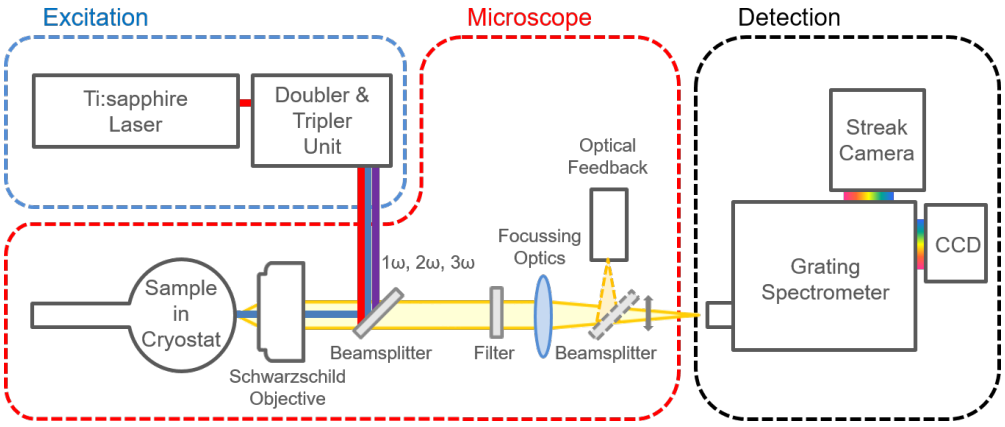

Figure 3.1: Schematic drawing of the TRPL-Setup used in the framework of this thesis. The setup allows for measurements at high spatial, temporal and spectral resolution of a broad range of excitation energies and at cryogenic temperatures.

3.2.2 Data Evaluation

In an TRPL experiment one always monitors the population dynamics of the emissive state. In a solid excitons can be assumend the main source of luminescence. Thus, the observed lifetime of excitonic luminescence, τ_{PL}, depends merely on the exciton population N_X:

$$\frac{dN_X(t)}{dt} \propto N_X(t). \tag{3.4}$$

Equation 3.4 can be solved analytically and yields

$$N_1(t) = N_0 exp^{-\frac{t}{\tau_{PL}}}. \tag{3.5}$$

The population N_X and thus the PL intensity I_{PL} decay in a single-exponential manner with a decay-constant of $1/\tau_{PL}$. This is generally true for all cases in which the dynamics only depends on the the population of the emissive state. Exceptions are given, e.g., in the case of the recombination of an electron-hole plasma. Here the dynamics depend on the product of electron and hole population and the resulting decay dynamics are of parabolic behaviour.

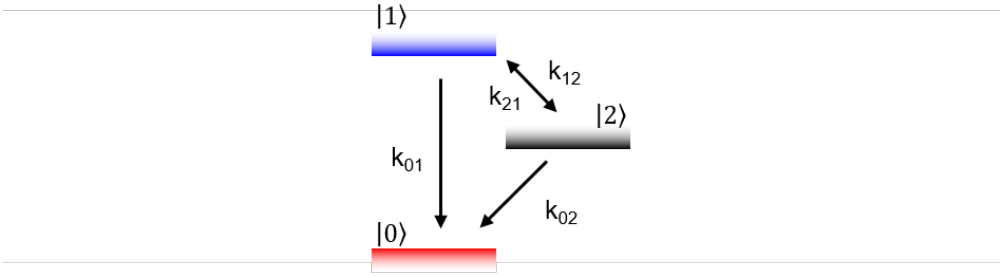

Figure 3.2: Three-level system that was assumend for the calculations. The arrows indicate the corresponding rates between the levels.

Deviations from the expected single-exponential behavior allow to extract interesting properties of the system under study. An example shall be given for an idealized optical three level system (cf. Fig. 3.2), consisting of the ground state $|0\rangle$ the excited state $|1\rangle$ from where emission occurs and a third state, $|2\rangle$, which is able to interact with $|0\rangle$ as wells as with $|1\rangle$. For the three states involved, the rate equations are as follows

$$\frac{dN_0}{dt} = +k_{02}N_2 + k_{01}N_1, \tag{3.6}$$

$$\frac{dN_1}{dt} = -\left(k_{01} + k_{21}\right)N_1 + k_{12}N_2, \tag{3.7}$$

$$\frac{dN_2}{dt} = -\left(k_{12} + k_{02}\right)N_1 + k_{21}N_1. \tag{3.8}$$

As in a transient PL experiment the system is excited by a short laser pulse which promotes the $|1\rangle \leftarrow |0\rangle$ transition, the dynamics of $|0\rangle$ are irrevalent. From transient

PL data, the sum of the two rates $k_{01} + k_{21}$ is obtained. The information on (de-)population dynamics of N_2 are considered not accessible by PL and thus a "dark" state. It will be shown that there exists an analytical solution to equations Eq. (3.7) and Eq. (3.8). The set of equations can be written as a matrix equation of the form $\dot{\vec{N}} = \mathbf{A}\tilde{N}$, where

$$\mathbf{A} = \begin{bmatrix} -(k_{01} + k_{21}) & k_{12} \\ k_{21} & -(k_{12} + k_{02}) \end{bmatrix}$$

is the coefficient matrix. A general solution can be assumed to be given by $\vec{N} = \vec{a}e^{rt}$ with r and $\vec{a}$ the eigenvalues and -vectors, respectively. Using $|\mathbf{A} - \mathbf{I}r| = 0$ we obtain for the eigenvalues r two decay constants

$$k_i = \frac{1}{2}\left[Tr(\mathbf{A}) \pm \left(Tr\left(\mathbf{A}\right)^2 - 4Det\left(\mathbf{A}\right)\right)^{1/2}\right]. \tag{3.9}$$

For the eigenvectors of the system we obtain

$$\vec{a_i} = \begin{pmatrix} k_{12} + k_{02} + k_i \\ k_{21} \end{pmatrix}. \tag{3.10}$$

The general solution is given by

$$\begin{pmatrix} N_1 \\ N_2 \end{pmatrix} = C_1\vec{a_1}exp^{r_1 t} + C_2\vec{a_2}exp^{r_2 t}. \tag{3.11}$$

At $t = 0$, immediately after the excitation pulse, $N_1(t = 0) = 1$ and $N_2(t = 0) = 0$, we thus obtain

$$\frac{C_1}{C_2} = 1 + \frac{k_\Delta^2}{k_{21}k_{12}}. \tag{3.12}$$

Reversible processes (e.g., charge separation, ISC) in individual molecules or bimolecular process frequently show bi-exponential decay dynamics. From the (bi-exponential) fitting of the experimental data the two decay components, τ_1, τ_2 and their respective amplitudes a_1 and a_2 are obtained. If now, for example, a quenching study is performed, k_{01} could be determined by measuring the PL lifetime with no quencher present. The missing three rate constants k_{12}, k_{21} and k_{02} can then be calculated from from the following equation

$$\begin{aligned} \frac{a_1}{a_2} &= \frac{k_1 - Y}{Y - k_2}, \quad k_i = \frac{1}{\tau_i}, \quad Y = k_{12} + k_{02}, \quad X = k_{01} + k_{21} \\ k_i &= \frac{1}{2}\left[(X+Y) \pm \left((X+Y)^2 - 4k_{12}k_{21}\right)^{1/2}\right]. \end{aligned} \tag{3.13}$$

3.3 Photoluminescence Excitation Spectroscopy

The experimental technique where a continously tunable excitation source is used to detect the PL intensity as a function of the excitation wavelength is known as PLE. The most common use of this technique is to study the absorptive behaviour of samples grown on opaque substrates. In this case, an absorption measurement in transmission geometry is impossible without etching or thinning of the substrate. Generally speaking, one assumes the relation between PL intensity I_{PL} at a fixed detection wavelength, λ_{Det}, and excitation intensity I_{Exc} to be as follows:

$$I_{PL} \propto \alpha(\lambda_{Exc}) \cdot \gamma \cdot P_{rad} \cdot I_{Exc.}(\lambda_{Exc}). \tag{3.14}$$

Here, $\alpha(\lambda_{Exc})$ denotes the absorption coefficient of the material, derived from Lambert-Beer law. The probability for excited carries to relax to the emissive state, γ, and their subsequent probability of radiative recombination, P_{rad}, are assumed to be excitation wavelength independent. One assumes that the carriers "forget" how they reach the emissive state which makes γ independent of λ_{Exc}. In this case, a measure directly proportional to the absorption coefficient is obtained if I_{Exc} is held constant. However, sometimes $\gamma = \gamma(\lambda_{Exc})$ is a more precise description of physical reality. In this case, the coupling efficiency between absorptive states and the emission channel can be deduced by comparing PLE and absorption measurements. Both, qualitative and quantitative deviations between the two spectra give insight into the intricate relaxation dynamics of individual molecules and molecular crystals.

The PLE measurements performed within the framework of this thesis where obtained with to different experimental setups, depending on specific requirements. For measurements on the PDI material system described in section 4, a commercial flourometer[7]

[7] "FlouroLog", Horiba Scientific

was used. Here, a 250 W Xenon arc lamp is used as excitation source. The white-light sepctrum is dispersed by a double-monochromator delivering excitation linewidths of 0.1 nm. Emitted light is again dispersed by a grating monochromator and detected by photomultiplier tube and Germanium detector for measurements in the VIS and NIR spectral region, respectively. The setup however is limited to measurements at room temperature and offers only very limited spatial resolution.

Within this thesis, a setup for PLE measurements has been developed. Again, a Ti:Sa laser[8] is used as primary light source. The Ti:sa produces 1 W of pulsed output, when pumped by a 5 W intra-cavity frequency-doubled Nd:YVo laser[9]. A low dispersion mirror set is used to generate pulses of 30 fs length. This comes at the cost of a reduced tuning range, which is in this case about 1.48–1.61 eV (770–840 nm). A photonic crystal fiber (PCF)[10] generates a white-light supercontinuum spanning roughly two octaves. Within the crystal fiber, a combination of self phase modulation, Raman scattering, and soliton generation leads to a spectral broadening of the fundamental laser pulse. To select the desired excitation wavelength from the supercontinuum, a homebuilt prism monochromator is used. The facet of a single mode fiber is used as slit. The fiber is mounted on a motorized stage allowing selection of the desired wavelength. To excite the sample, the end facet of the fiber ($d = 400\,\mu m$) is imaged by an achromatic lense onto the sample surface. To cool the samples to cryogenic temperatures, a closed-cycle helium cryostat[11] is employed. The emitted light is imaged onto the entrance slit of the f/4.1 grating spectrometer[12]. In this configuration, an intensity of 0.5 mW/nm is obtained under ideal circumstances. Taking the 1:3 de-magnification of the fiber facet into account, the laser spot size of 130 µm corresponds to a peak excitation density in the range of $12\,W/c^2m$. A value sufficient for the material classes under study, if a sensitive combination of grating blaze wavelength and CCD is selected.

To take into account fluctuations in excitation power during the runtime of the experiment, a back reflection from the focussing lense is constantly monitored with a laser power meter[13]. By this effects caused the non-constant intensity distribution of the supercontinuum as well as power fluctuations over time a are eliminated from the

[8] "Tsunami", SpectraPhysics
[9] "Millenia V", SpectraPhysics
[10] "FemtoWhite 800", NKT Photonics
[11] "8300 compressor" and "M22 cryodyne refrigerator", CTI-Cryogenics
[12] "Triax 320", Horiba-JobinYvon
[13] "PM100 w/ S130A Si-Diode", Thorlabs

measured PLE signal.

Unlike convententional PLE setups, where a monochromatic detection is used (as the spectral information is gained by tuning the excitation wavelength), in the setup used here, a liquid nitrogen cooled Si CCD is used as detection. This allows, in principle, 2D PLE measurements, where individual PLE traces can be extracted from the entire emission spectrum of the sample. The use of a pulsed excitation source in principle also allows the measurement of time-resolved PLE spectra. This is planned as a future step of experimental implemention.

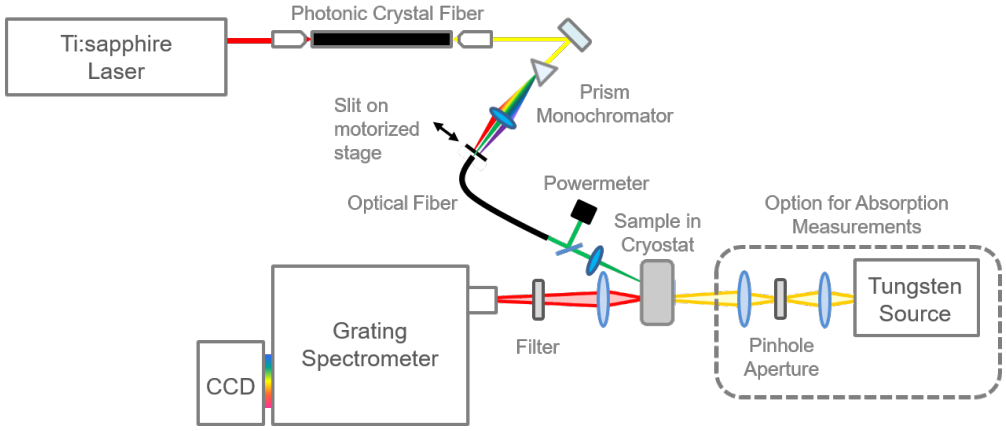

Figure 3.3: Schematic drawing of the PLE setup. By taking advantage of a highly nonlinear PCF an octave-spanning bright white-light supercontinuum is used as excitation source after being dispersed by the prism monochromator.

3.4 Photoluminescence Quantum Yield

The determination the electro- and PL quantum yield is one of the key parameters of characterization of flourescent materials. Its technological benefit is crucial for optimization of devices such as OLEDs. Beyond, the characterization of, e.g., the temperature-dependence of the PLQY gives insight on the nature of non-radiative decay channels or - in the case of condensed matter - parameters such as spatial fluctuations of material parameters (e.g., disorder-related effects).

The experimental apparatus is illustrated in Fig. 3.4. An excitation laser of choice is used to excite the sample which is mounted inside an integratig sphere. The sphere is coated with a diffuse high reflectance coating, yielding nearly perfect Lambertian

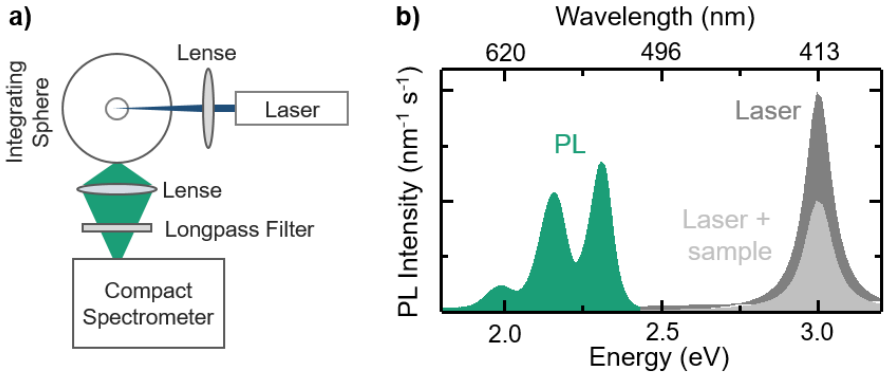

Figure 3.4: (a) Schematic drawing of the experimental setup used for the determination of the PLQY. (b) Illustration of how the PLQY is determined experimentally from the measurement of power emitted from the sample (green) and laser (light grey). This is referenced again the laser power with no sample (dark grey) installed in the integrating sphere.

behaviour and a minimum reflectance of 98 % in the wavelength region of interest. By this, all anisotropy in the spatial emission characteristics can be compensated for. The challenge and main source of error lies in the precise calibration of the spectral response of the detection scheme[14]. A calibrated Tungsten halogen light source[15] which is held at constant temperature is used for this purpose. In general, the PLQY is defined as follows:

$$\eta = \frac{\text{number of photons emitted}}{\text{number of photons absorbed}}. \tag{3.15}$$

To determine the PLQY (Eq. (3.15)), first the number of photons absorbed has to be determined. To this end, two measurements have to be performed: 1) the laser spectrum impinging on the integrating sphere. 2) a measurements with the sample installed in the sphere, in which both, the laser and the sample spectrum are recorded. The respective areas are then integrated and $A_{exc.,w/oSample} - A_{exc.,w/Sample}$ gives the absorbed power and ratio of the former and the integrated PL area A_{PL} then gives the photoluminescence QY:

[14] "USB2000", OceanOptics
[15] "HL2000", Avantes

$$\eta = \frac{A_{exc.,w/oSample} - A_{exc.,w/Sample}}{A_{PL}} \times 100\%. \tag{3.16}$$

Additionally, PLQY measurements are complementary to TRPL, as the combination of both techniques allows the separation of radiative recombination rate, k_r and non-radiative recombination rate, k_{nr}:

$$\eta = \frac{k_r}{k_r + \sum k_{nr}}. \tag{3.17}$$

In general, there exists more than one non-radiative recombination channel. For this reason, k_{nr} is written as $\sum k_{nr}$ in Eq. (3.17).

4 Interfaces on a Molecular Scale: Perylene Diimides

Perylene derivatives such as the perylene diimides (PDIs) were initially synthesized in the 1910s. From the 1950s on, they found a broad range of applications, e.g., as high-grade pigments in industrial applications such as automotive finishes [38]. Since these early days, PDIs have developed into one of the most valueable material classes of molecular electronics. Recently, advanced uses in contactless pH measurements, as metal cation sensors, and as active layers in OPV are proposed. Moreover, SF has been reported in slip-stacked thin-films of ortho-phenyl-substituted PDIs [39] and it is also expected to occur in rigidly linked dimers. Beyond their technological benefit, PDIs are also ideal model systems for charge and energy transport studies. Their high thermal and photochemical stability along with their preferable spectral range and electron acceptor properties favor such fundamental investigations [9]. While a vast number of publications investigate core- and imide-N-substituted PDIs, only very few focus on perylene dihydrazides (PDHs). Utilizing a short fluorophore-fluorophore distance, nitrogen-nitrogen linked perylene and naphthalene imide dyads and triads are used as model systems for the investigation of (single) molecular wires and intramolecular energy transfer [40–43]. Their use as dyes in p-type dye sensitized solar cells leads to a sharp increase of solar cell efficiency: the formation of dye-localized long-lived charge separated states enables increased hole injection [44–47]. PDIs also promise to be able to compete with the fullerenes (discussed in Chap. 6) as electron transporting materials due to their high electron mobility, thermal stability, and structural variety. However, their, in general, strong tendency to form aggregates is detrimental with regard to possible applications [48]. The synthesis of the molecules studied in this thesis was aimed at creating an intramolecular donor-acceptor complex. The charge-separation and -recombination rates are controlled by different methods, i.e., protonation of the donor moiety, increase of donor acceptor distance and variation of excitation energy, respectively.

4.1 Sample Synthesis

The samples discussed in the following were synthesized by Eduard Baal from the group of Prof. Dr. Jörg Sundermeyer of the faculty of Chemistry at Philips University Marburg. Eduard Baal also performed the infra-red (IR) spectroscopy and CV measurements. density functional theory (DFT) calculations were performed by Malcolm Bartlett, also with the group of Prof. Sundermeyer and Remco W. A. Havenith from the University of Groningen.

Sample synthesis was aimed at obtaining the shortest possible D-A distance at the imide position. This position was deliberately chosen due to the presence of a node in the MOs of unsubstituted PDI. By this, orbital overlap is minimized and a defined "intramolecular interface" is obtained. The overall high aggregation tendency was overcome by covalently linking the PDIs via an imide nitrogen-nitrogen bond, which results in a perpendicular fluorophore orientation. This, in turn, leads to a reduced tendency of stacking. These beneficial properties could make nitrogen-nitrogen linked PDIs a serious competitor [48–51].

To probe the distance dependence of the photophysical properties, e.g., possible CT interactions, ethylene, propylene and hexylene bridge units are introduced to separate the donating amine and the PDI imide groups (cf. Fig. 4.1). The use of non-conjugating bridging units minimizes mixing of D and A MOs. Contrastingly, the more commonly used phenyl spacing units bear their own π-electron systems. As a consequence, the overall lower energy levels compared to non-conjugating units allow carrier localization on the bridge and thus "hopping"-like transport. The π-electrons themselves also provide rich carrier dynamics of their own. Details on the synthetic process can be found in Ref. [52].

4.2 Photoluminescence Quenching through Charge Separation

Intramolecular CT has been discussed in the literature as origin for PL quenching. To this end, PLQY measurements were performed on the reference "swallowtail" Langhals compound **1** and that of the derivatives of **1**.

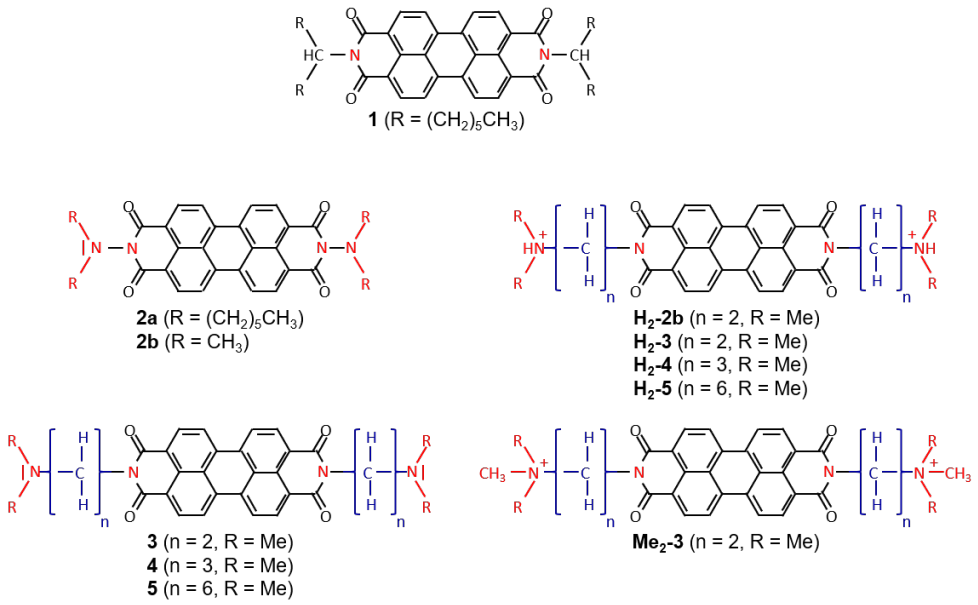

Figure 4.1: Overview of the PDI molecules synthesized for the study of internal interfaces on a molecular scale.

The effect of symmetrical substitution of the carbon atom at the imide position by nitrogen (cf. Fig. 4.1) was investigated by PLQY measurements introduced in Chap. 3.4. The results from steady-state spectroscopic measurements are presented in Fig. 4.2. The data corroborate the assumption that the photophysical properties of the Perylene backbone are not altered by the chemical substitutions. In line with the literature, the absorption maximum is located at 2.36 eV for samples dissolved in chloroform ($ChCl_3$) [40, 53]. A ≈30 meV blue-shift is observed, if acetonitrile (MeCN) is used as solvent, resulting in a well-established value of the absorption maximum (2.39 eV) [54]. Additionally, the Franck-Condon principle (cf., Chap. 2.1.3) is obeyed, indicated by the near mirror-symmetry of absorption and emission spectra. The vibronic progressions are spaced equidistantly by 170 meV and are unchanged in their spectral position and relative intensities, for all samples. Unlike the other spectroscopic properties, the PLQY is substantially changed for the nitrogen-bearing samples. The effect is visualized in Fig. 4.2(b), where the PL is compared on an absolute scale (note the logarithmic ordinate). The PL intensity drops more than one order of magnitude, indicating a reduction of the PLQY from almost 1 for **1** to below 0.005 for **2**. Thus, the presence of the electron lone pair at the amine group strongly suggests that a CT reaction is

responsible for the quenching of the PLQY.

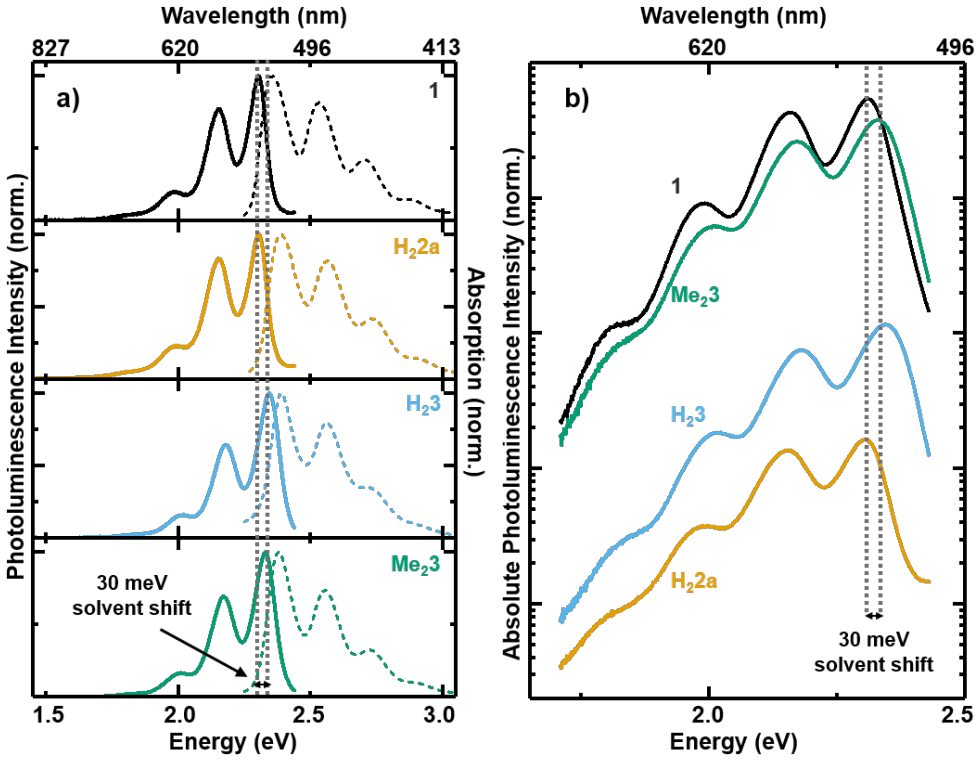

Figure 4.2: Normalized absorption (dashed) and PL (solid) spectra of **1** (as reference), $\mathbf{H_2 2}$, $\mathbf{H_2 3}$ and $\mathbf{Me_2 2}$. (b) Absolute PL of the same samples on a semi-logarithmic scale.

This conclusion is supported by DFT and time-dependent density functional theory (TDDFT) computations. For the nitrogen-bearing samples, the order of the MOs is altered. The π MO of the perylene core no longer constitutes the HOMO. Hence, the bright $\pi \leftarrow \pi^*$ transition is no longer the lowest energy electronic transistion (cf. Fig. 4.3). The calculations corroborate the assumption of decay to the radical anion state, $PDI^{\bullet -}$.

4.2.1 Effect of Protonation

It has already been reported in the literature [8], that protonation of the D group is expected to lower the oxidation potential of the former, possibly to a level at which the

PL-quenching CT process becomes energetically unfavorable. To this end, the nitrogen moiety of samples **2**-**5** was protonated using different protonation agents.

DFT calculations confirm the assumption that a protonation increases the oxidation potential, i.e., lowers the D's energy level [cf. Fig. 4.3(a) and (b)]. However, the protonated variant of sample **2**, **2p**, shows no significant recovery of PL intensity compared to **2**. DFT calculations do not take into the account effects of the sourrounding medium, i.e., the solvent. In a realistic scenario, there will always be an equilibrium between those protons bound to the donating amine moiety, and those dissolved in the solvent. The exact magnitude of this effect depends on the basicity of the solvent compared to that of the protonation target. It can be estimated by comparing the results of the PLQY measurements. For instance, by calculating the ratio of PLQY for two different D-A distances and comparing the result to that obtained for the respective protonated samples. For **2** and $\mathbf{H_2}$**2** the ratio amounts to unity. Controversely, for **3** and $\mathbf{H_2}$**3** a ratio of two is calculated. The same ratio is expected for both couples, as there is no reason for protonation to be more (or less) effective for either of the samples (**2** and **3**). From this, one can conclude that most likely another mechanism is responsible for inefficiency of the protonation.

Additional evidence for this claim is given by CV measurements. For unpronated sample **2**, a second oxidation potential is observed, intermediate to the electrochemical bandgap at 2.46 V which can be related to the HOMO-LUMO transition. However, for $\mathbf{H_2}$**2**, no such second oxidation potential is observed. This indicates that the oxidation potential attributed to the donor level is increased and thus the energetic position is shifted to energies lower than the fundamental transition. Consequently, this can be interpretated as clear evidence that de-protonation does not occur to a significant extent.

It is safe to assume that only a minority of protons is permanently solvated in the equilibrium. Hence, a different effect must be responsible for the absent recovery of PL intensity. For instance, this could be an excited state hydrogen transfer (ESHT). Several experiments were carried out to provide evidence for a hydrogen bond between the amine moiety and the perylene-centered carbonyl unit. Firstly the crystal structure of $\mathbf{H_2}$**2b**, which forms crystallites when sublimed, is compared to that of **2b**. From the X-ray diffraction measurements its is evident that the carbonyl bond at the imide

position is elongated in **H$_2$2b**, compared to **2b**. This is taken as indication of a hydrogen bond between the donating proton and the carbonyl oxygen.

Comparitive IR measurements corroborate the afformentioned assumptions (cf. Tab. 4.1). The hydrogen bond is indicated by a shift of the two modes associated with the C-O bond by $12\,\mathrm{cm}^{-1}$ and $17\,\mathrm{cm}^{-1}$, respectively, when comparing **2** and **H$_2$2**. Also, a weak trend is emminent for increasing D-A distances, e.g., for **5** and **H$_2$5** the shift reduces to only $1\,\mathrm{cm}^{-1}$ and $3\,\mathrm{cm}^{-1}$, respectively.

Table 4.1: Overview of IR absorption features associated with the C-O bond. The data for the uncharged samples are presented in the first three columns are compared to those of the charged samples are given in the second three columns.

Uncharged	CO′ (cm^{-1})	CO″ (cm^{-1})	**C**harged	CO′ (cm^{-1})	CO″ (cm^{-1})
1	1697	1658			
2	1707.6	1666.8	**H$_2$2**	1719.7	1683.4
2b	1708.8	1664.3	**H$_2$2b**	1728.6	1996.3
3	1692.8	1651.9	**H$_2$3**	1695.3	1654.0
			Me$_2$3	1696.0	1652.5
4	1692.7	1647.3	**H$_2$4**	1688.6	1654.9
5	1691.3	1650.1	**H$_2$5**	1692.4	1653.1

As final check of consistency, a methylated sample is investigated. Methylation should in principle have the same effect as protonation. However, instead of a proton, a methyl group is used to lower the D's energy level. As the methylene binds covalently to the nitrogen, a de-protonation effect is virtually excluded. Also, generally speaking, hydro-carbons are very weak acids ($40 < pK_a < 50$). They are thus considered too weak proton donors for hydrogen bonding to occur [55]. Both, the PLQY (cf. Fig. 4.2) as well as the PL lifetime (cf. Tab. 4.3) fully recover for the methylated sample **Me$_2$3**. **3** was chosen for methylation because a methylated **2** could not be obtained, even with the strongest methylations agents available.

Further investigations are required to fully confirm that an ESHT leads to the absent recovery of PLQY under protonation. A time-resolved VIS-pump - broadband IR-probe experiment could provide an answer to this question. Regardless, as proof for the existence of a hydrogen bond has been given and de-protonation is excluded, the assumption of an ESHT appears convincing.

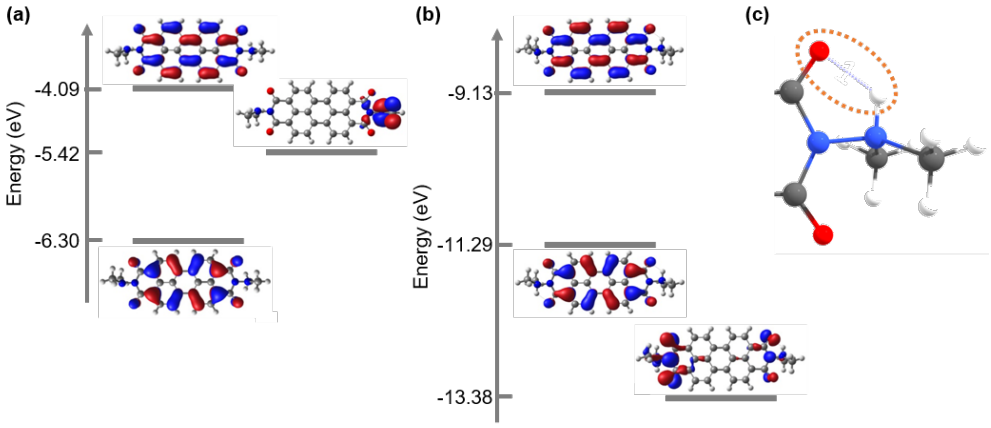

Figure 4.3: MO energy level diagram based on the S_1 excited state B3LYP/6-31G* calculated for **2** (a) and $\mathbf{H_2 2}$ (b) showing the effect of protonation upon the amine donor MO. Protonation stabilizes the amine MO and, thus, radiative recombination should be favoured over IC. (c) illustrates the hydrogen bond between the amine-centered proton and the carbonyl oxygen.

4.2.2 Effect of Altered Donor-Acceptor Distance

As the mechanism behind the quenching of the PLQY has unambigiously been identified as a (photoinduced) CT process, its exact nature shall be investigated closer. To this end, a systematic variation of the D-A distance is beneficial. Therefore, the series of samples bearing spacing units in between the nitrogen-nitrogen pairs of compound **2** is studied. The spacers consist of alkyl chains of two, three and six methylene (CH_3) groups for **3**, **4**, and **5**, respectively.

CV measurements are carried out to determine the respective oxidation and reduction potentials. The results are given in Tab. 4.2 along with an estimate of the Gibbs free energy of charge separation, ΔG_{CS}. The variations in $E_{(0,0)}$ obtained from the absorption measurements are <5 meV, while the Δ_{redox} values are reduced by 30 meV compared to the former. This corrobates the assumption of an additional energy level, intermediate to the lowest optically bright transition. Additionally, the Δ_{redox} of all donor-bearing samples is significantly lowered, compared to the reference compound **1** ($\Delta_{redox} = 2.46$ eV).

The Gibbs free energy ΔG_{CS} was calculated according to Eq. (2.24). The edge-to-edge distance R_{ee} is determined by DFT calculations and taken as the nitrogen-nitrogen

edge-to-edge distance. It should be noted that these values offer the upper limit of the D-A distance, because calculations assume stretched alkyl chains. The ϵ_{ref} and ϵ_s values are the dielectric constants of the respective solvents (for CV and optical measurements, respectively). The radii $r+$ and $r-$ are the ionic radii and taken from the literature as 200 nm for the cation and 471 nm for the anion [56].

Table 4.2: Optical and electrochemical bandgaps for the sample series with increasing D-A distance. Estimates for ΔG_{CS} are given relative to the first excited singlet state (S_1).

Sample	E_{0-0} (eV)	Δ_{redox} (eV)	R_{ee} (pm)	ΔG_{CS} (eV)
1	2.303	2.46	-	-
2	2.305	2.26	143	-1.64
3	2.302	2.27	373	-0.34
4	2.304	2.10	458	-0.37
5	2.297	2.26	797	0.08
$\epsilon(CHCl_3) = 4.81$,		$\epsilon(DCM) = 8.93$,		$\epsilon(MeCN) = 37.5$

The results of the calculation indicate that the $S_1 \rightarrow CSS$ decay becomes more favorable with decreasing D-A distance. For **2a** and **2b** (no alkyl spacers), the energy of the CSS is well below that of the S_1 state. For the C_2 and C_3 alkyl spacer bearing **3** and **4** ΔG_{CS} is significantly lower than for **2** and **2b**. In the case of **5**, decay to the CSS becomes energetically unfavorable. This occurence of a CSS confirms that PL quenching is due to a CT process. Note that the Gibbs free energy for **5** is calculated assuming a stretched alkyl chain. Calculations using shorter D-A distances for **5** result in a $\Delta G_{CS} = -0.14\,\text{eV}$ (for $R_{ee} = 500\,\text{pm}$), making CS favorable again. This hefty dependence on R_{ee} emphasizes the importance of the D-A distance on the formation and population efficiency of the CSS.

The findings agree with the optical measurements. As shown in Fig. 4.4, all samples show virtually identical absorption spectra, similar to the first series shown in Fig. 4.2. Spectral shapes and positions again show no effect on the appendage of substituents. Constrastingly, the PLQYs depend heavily on the distance between perylene backbone and D unit [illustrated in Fig. 4.4(b), which shows the absolute emission intensities]. The addition of the amine groups and their electron lone pairs invoke a drop in PLQY of more than two orders of magnitude, compared to **1**. The systematic introduction of alkyl chains as spacer units leads to a recovery of the PLQY. Eventually, for **5** (C_6 spacing unit) an efficiency of ≈0.64 is obtained, even in the unmasked neutral form.

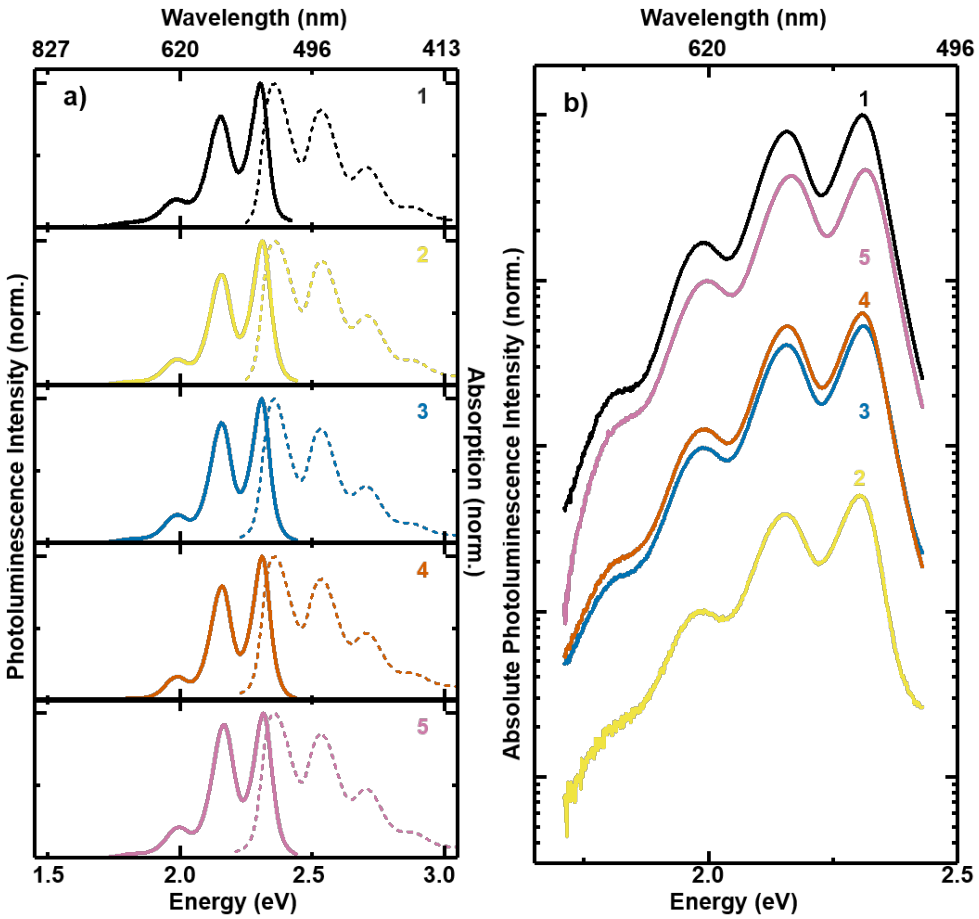

Figure 4.4: (a) Normalized absorption (dashed) and PL (solid) spectra of **1** to **5**. (b) Absolute PL of the same samples on a semi-logarithmic scale.

4.3 Excited State Dynamics

4.3.1 Analysis of Decay Dynamics

TRPL measurements provide further insight into the temporal dynamics of the population of the emissive S_1 state. Characteristic decay profiles are shown in Fig. 4.5(b). The reference compound **1** shows a single-exponential decay with a characteristic lifetime of ≈4 ns as is expected due to its virtually exclusively radiative decay. Drastic deviations from this behavior are found for the amino-substituted compounds. Samples **2**, **3** and **4** no longer show single-exponential behavior but rather more complex dynamics which are well-described bi-exponentially. While the initial decay (t_{fast}) is fastest for

2, the lifetime recovers for larger distances and the is almost single-exponential again for sample **5**, incorporating the longest (C_6) spacer.

Table 4.3: Spectroscopic properties of the samples under study. PLQYs (Φ_{PL}) and decay times measured by TRPL. All values are given for $E_{exc} = 2.8\,\text{eV}$.

Sample	Solvent	Φ_{PL} (%)	t_{fast} (ps)	t_{slow} (ps)	A_{fast}	A_{slow}	R^2
1	$CHCl_3$	>90.0	3908 ± 92 ($= t_{Ref}$)		83.2 ± 0.2[a]		0.98
2	$CHCl_3$	0.5	18.0 ± 0.1	269 ± 26	92.0 ± 0.1	6.8 ± 0.2	0.98
3	$CHCl_3$	5.4	59.0 ± 0.1	1345 ± 14	83.7 ± 0.3	14.4 ± 0.1	1
4	$CHCl_3$	6.1	132 ± 1	729 ± 20	95.1 ± 0.5	9.2 ± 0.6	1
5	$CHCl_3$	64.0	591 ± 122	2179 ± 374	27.1 ± 11.6	71.5 ± 11.5	1
$\mathbf{H_2 2}$	$CHCl_3$	0.5	30 ± 1	2090 ± 529	94.0 ± 0.1	5.0 ± 0.1	0.98
$\mathbf{H_2 3}$	MeCN	10.3	254 ± 87	6368 ± 561	80.7 ± 0.3	16.4 ± 0.1	0.99
$\mathbf{Me_2 3}$	MeCN	89.0	3472 ± 84 ($= t_{PL}$)		87.5 ± 0.4[a]		0.97

[a] >100 % because of "backsweeping" effect in the streak camera.
$\epsilon(CHCl_3) = 4.81$, $\epsilon(\text{DCM}) = 8.93$, ϵ (MeCN) = 37.5

As already mentioned, CV measurements and theoretical calculations indicate that an electron transfer from the amine is responsible for the PL quenching. More precisely, the molecule rapidly decays from its S_1 state to the $PDI^{\bullet-}$ CSS. In accordance with previous reports, the fast, initial quenching is assumed to give a figure for the rate of CS and thus decay to the CSS [57–59]. The decay profile for sample $\mathbf{Me_2 3}$ could not be approximated by bi-exponential functions anymore. Here, rate of CS is determined by the fitted single-exponential lifetime t_{PL}. As the intrinsic radiative lifetime is expected to be given by reference sample **1** and is supposedly unchanged for all samples, the k_{CS} is obtained:

$$k_{CS} = 1/t_{PL} - 1/t_{Ref}. \tag{4.1}$$

The observation of a non-single-exponential behavior for **2** and **4** - **5** can have various physical origins. The majority of which can be excluded due to careful measures taken during the experiments. In Tab. 4.4 all possible non-intrinsic mechanisms, which can lead a non-single-exponential decay are summarized. Dependencies on experimental conditions and observable effects respective mechanisms would show are also given. Additionally, 1H-NMR measurements were carried out to rule out sample contaminations by another soluble PDI-specimen, which could lead to the observed long-lived PL

component. Aggregation as an explanation for a non-single-exponential behavior seems unlikely for **2**, since a strong structural similarity to **1** is given and **1** is widely known for its very low aggregation tendency. Additionally, the spectroscopic measurements show no indication of aggregation, which is typically indicated by a broadening of resonance and overall red-shift of absorption and PL spectra (cf. Chap. 2.2). Moreover, the respective amplitudes of the fast and slow decay component vary for the different samples, showing generally an increased A_{slow}/A_{fast} ratio with increasing D-A distance (cf. Tab. 4.3).

Table 4.4: Non-intrinsic mechanisms leading to non-single-exponential decay dynamics.

Dependency	**Sample Concentration**	**Excitation power**	**Spectral shift**
Mechanism			
FRET	++	o	o
Two-Photon absorption	o	++	o
Multi-electron excitation	o	++	o
Aggregation	++	o	++
Dimerization	o	o	++

The TRPL data provides further insight into the CS dynamics of individual molecules as bimolecular or aggregation effects and other extrinsic origins are excluded: varying the excitation fluence and concentrations in the sample solutions over several orders of magnitude provide identical results. Intriguingly, the PL decay is non-single-exponential for all D-bearing samples.

This infers the existence of an additional, reservoir, state in the molecule feeding the bright transition: the emission from an optical two-level system of localized states will always yield a single-exponential decay. Adding a second, possibly non-radiative decay channel again results in a single exponential decay. The combined decay rate in the law of decay is given by the sum of the two individual rates ($1/t_{combined} = 1/t_1 + 1/t_2$). Consequently, an additional reservoir needs to be involved to invoke a bi-exponential decay. A bi-exponential decay will result exclusively from the independent population of this reservoir, which is able to feed the originally considered emissive state. Taking into account this mathematical fact sheds new light on the obtained experimental results.

The CSS is a viable candidate for the proposed reservoir state. This infers that the photoinduced CS is accompanied by the reverse process, which repopulates of the emissive state. In turn, the repopulation leads to the observed bi-exponential PL decay, the CSS acting as shelving state. Following the method described in Chap. 3.2.2, the three rates k_{CS}, k_{rCS} and k_{CR} (cf. Fig. 4.5) can be obtained from the two t_{fast} and t_{slow} and the ratio A_{fast}/A_{slow} of the respective amplitudes. The value for $k_{0\leftarrow1}$ (cf. Chap. 3.2.2) is taken from the inverse single-exponential lifetime $1/t_{Ref}$ of reference **1**.

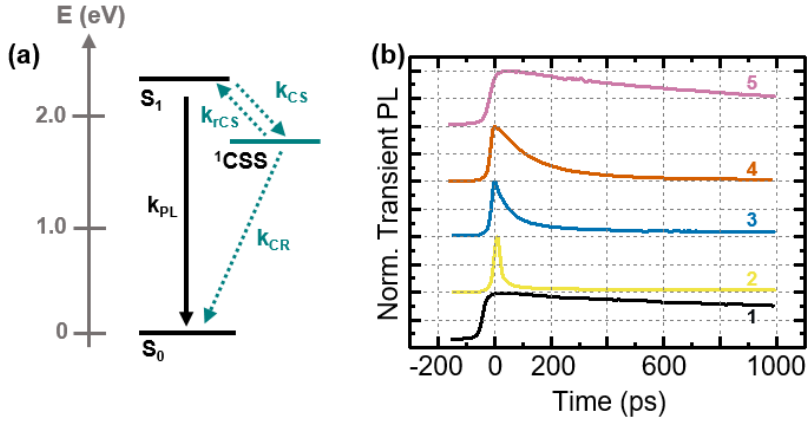

Figure 4.5: (a) Proposed energy level diagram for the decay of the excited S_1 state probed by TRPL. (b) Transients of the reference sample **1** as well as the samples from the distance series, **2** to **5**, respectively.

The obtained rate constants are shown in Fig. 4.6. A clear dependence of the k_{CS} and k_{rCS} on the D-A distance is observed, both decreasing with distance. The fact that k_{CS} and k_{rCS} are correlated and not anti-correlated is intriguing at first. A possible explanation is schematically shown in Fig. 4.7(a). There, simplified PEPs for all three states involved are given. With decreasing D-A distance, the CS process becomes more and more exergonic, while ocurring in the "normal" Marcus regime. For **2**, both k_{CS} and ΔG_{CS} peak. The spectral and temporal emission characteristics of **2** in a poly(methyl methacrylate) (PMMA) matrix are temperature-independent in the range from 10–300 K [cf. Fig. 4.6(b)]. This observation reveals that the CS reaction occurs close to the Marcus optimum region and, thus, almost activationsless.

For the reverse CS process, rate constants are generally reduced by almost two orders

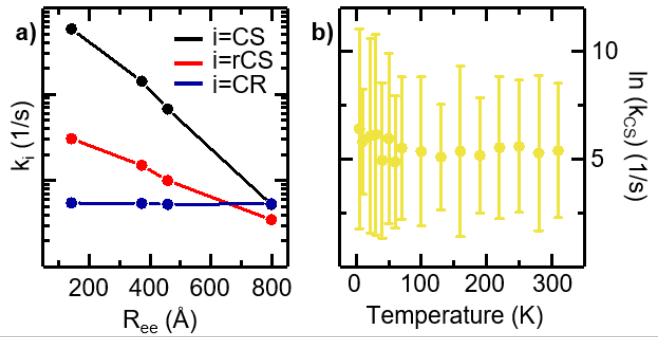

Figure 4.6: (a) Rate constants deduced by the method explained in the text, for forward and reverse charge separation (black, red), respectively, and for charge recombination (blue). The R_{ee} values reflect the D-A distances obtained by DFT. (b) Temperature-dependence of k_{CS} of **2** in a PMMA matrix over a temperature range of 10–300 K.

of magnitude, compared to the forward process [cf. Fig. 4.6(a)]. The reverse process is endergonic ($\Delta G^{rCS} > 0$) in all cases, the only exception being **5**, depending on which D-A distance is assumed. Consequently, the k_{rCS} are more than one order of magnitude lower than those for forward CS. The observation of decreasing k_{rCS} with increasing D-A distance is puzzling at first, but can be understood when considering the situation shown in Fig. 4.7(b). While going from **2**→**5**, the ΔG^{rCS} values , the reorganization energies E_{λ}^{rCS} increase more rapidly (with increasing D-A distance), hence reducing the CT rate growing with donor-acceptor distance.

Finally, for k_{CR}, the dependence on the D-A distance is significantly lowered. Again, the largest rates are obtained for the shortest D-A distances. This behaviour is explained in Fig. 4.7(b), where the PEPs for the the ground state, the exicted π^* state and the CSS are schematically shown. In all cases, the intersection of initial and final state's PEPs is in close proximity to the potential energy minimum of the CSS. Consequently, the rates depend less strongly on ΔG but to a larger extent on the (exponentially) decreasing overlap of PDI core and amine donor MOs, respectively.

4.3.2 Dependence on Excitation Energy

Next, the dependence of the PL decay and, therefore, the electron transfer rate constants (k_{CS}), on the excitation photon energy is discussed. Four different excitation

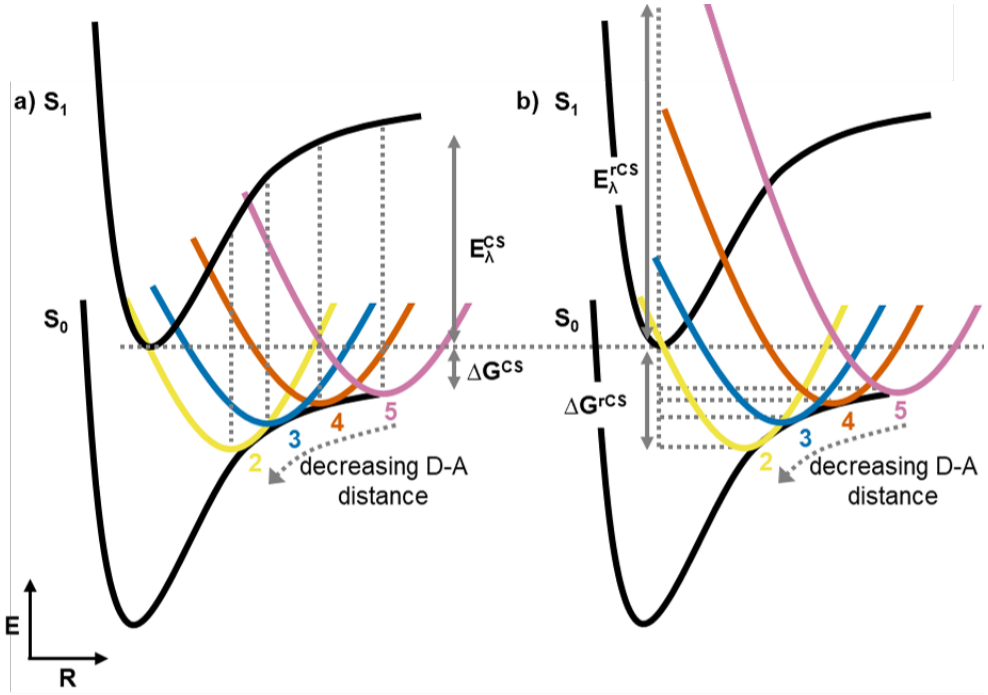

Figure 4.7: Proposed scheme of the PEPs for the forward (a) and reverse CS processes (b) for the distance series **2**-**5**.

energies are used in time-resolved measurements, 2.5 eV, 2.8 eV, 3.3 eV, and 4.5 eV (cf. Fig. 4.9). Pumping at 2.5 eV and 2.8 eV excites the system into the S_1 electronic state, while higher-lying singlet states, denoted S_x, are excited with excitation photon energies of 3.3 eV and 4.5 eV.

Initially, the reference sample **1** is discussed. Fig. 4.8(a) shows the comparison of the linear absorption and PLE data. The peak positions and intensities show good overall agreement. Strikingly, in three distinct spectral regions (3.0–3.2 eV; 3.4–3.5 eV; 4.1–4.6 eV), the PLE signal is significantly lowered, compared to the absorption measurement. This indicates a violation of Kasha-Vavilov's rule. While it is generally assumed that the quantum efficiency is independent of the excitation energy (Vavilov's law), this rule is not obeyed here. This phenomenon, commonly referred to as "anti-Kasha"-behavior, has been subject of research studies for many years [60, 61]. The deviations infer an additional loss channel, as the PLQY is lowered in the respective excitation energy regions. One possibility is that of an ISC to a higher lying triplet state. It has been shown, that for higher energy excitation, ISC rates can significantly

Table 4.5: TDDFT (B3LYP/6-31G**) calculations for the first ten triplet excitation energies using DALTON 2.0. Energies given in eV.

Sample	**1**	**2**	**3**	**4**	**5**
Mode #					
1	1.236743	1.242301	1.238784	1.240160	1.240974
2	2.676726	2.145085	1.880988	1.887959	1.941363
3	2.788240	2.150013	1.933428	1.929191	1.959174
4	2.952286	2.684797	2.679917	2.681089	2.681879
5	2.978699	2.788131	2.786522	2.786900	2.785632
6	2.983389	2.925977	2.951342	2.946222	2.946871
7	3.053460	2.931112	2.961256	2.954997	2.948360
8	3.192909	2.978014	2.973610	2.957820	2.952136
9	3.247663	3.104894	3.049473	3.045296	3.031313
10	3.252397	3.315574	3.170836	3.161499	3.144373

increase and become competitive to $S_x \rightarrow S_1$ IC and vibrational relaxation (VR), respectively [60] even in materials with negligeable spin-orbit coupling. DFT calculations reveal multiple triplet states close to the higher lying singlet states (cf. Tab. 4.5). Consequently, an accelerated ISC appears plausible. The TRPL transients in Fig. 4.8(c) reveal a dependence of the PL lifetimes on excitation energy is, i.e. for higher excitation energies, a 1.7-fold lifetime increase is observed. Hence, the excited state dynamics of the S_1 state are no longer independent of the excitation energy. In addition, spectral positions and relative weights of the vibronic progressions (VPs) in the PL spectra show small but observable differences (cf. Fig. 4.8). These findings are not trivial and the most likely explanation lies in an external effect. The charge-distributions are expected to significantly differ between the S_1 and the higher lying states. In general, the orientation of the molecular dipole will also change. The dipole-dipole interaction between solute and solvent molecules infers a reorientation of the electron-distribution of the solvent molecules and, in some cases, also of the nuclei. As nuclear motion is comparably slow (cf. Chap. 2.1.2), solvent reorganization times can increase.

Next, the k_{CS} rates for the distance series **2**–**5** is discussed. The CS rates of all samples peak at 2.8 eV excitation energy. They subsequently decrease for higher and lower excitation energies, respectively. Sample **5** shows an overall weak dependence on excitation energy. This is probably owed to the already low k_{CS}; the PLQY already approaches that of **1**. The initial increase of k_{CS} is most pronounced for **2**. For an excitation with

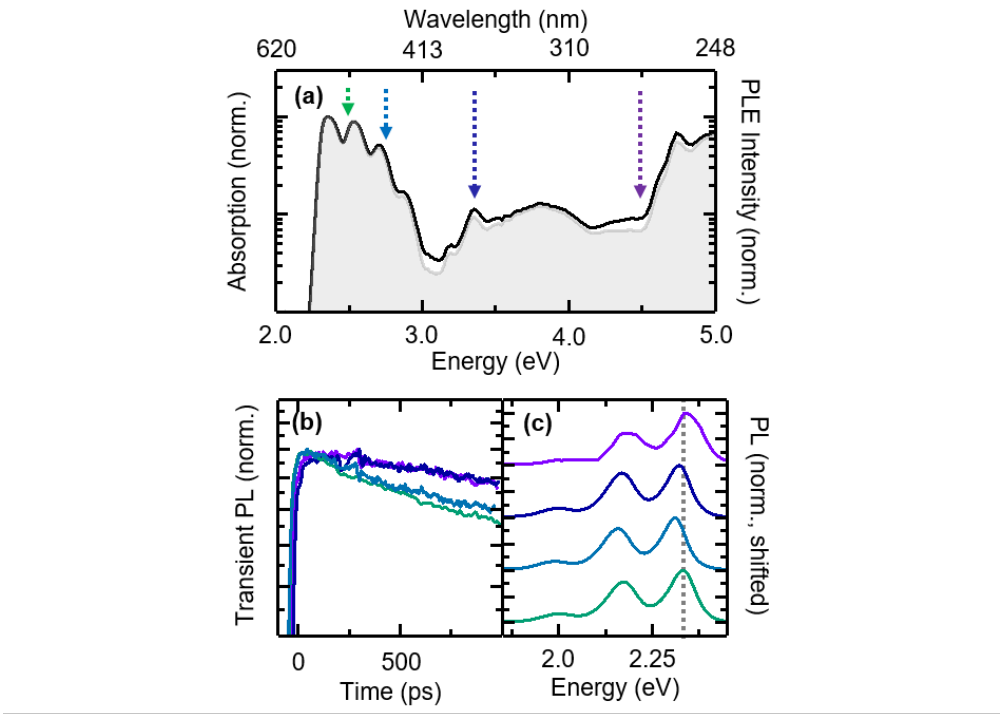

Figure 4.8: (a) Comparison of absorption (shaded grey area) and PLE spectra for reference sample **1**. The detection is set to the PL maximum (2.3 eV). The colored arrows indicate the excitation energies used to determine the dependence of k_{CS} on E_{exc}. Both spectra are normalized to their respective intensities at 2.33 eV excitation. (b) The results of the excitation energy-dependent TRPL measurements. (c) The normalized PL spectra corresponding to the transients in panel (b).

2.8 eV photon energy, the system is transferred to a higher vibrational sublevel of the S_1 state (compared to $E_{exc} = 2.5$ eV). The surplus vibrational energy might facilitate the transition to the CSS and thus increase the CS rate and efficiency. Several studies show an impact of high-energy vibrational levels on excited state reactions, e.g., CT processes [62–64]. Vibrational relaxation within the S_1 excited state of perylene in solution has been measured to occur on a timescale of 30 ps, very well on a timescale comparable to $1/k_{CS}$ of **2** [65], and, hence, on the same timescale as the ultra-fast decay to the CSS.

Possibly, the general assumption of all photophysical and -chemical reactions proceeding from a vibrationally relaxed state (as a consequence of Kasha's rule) does not hold. Alternatively, the dissipation of the excess excitation energy to the surrounding

medium could lead to a local heating. This increased vibrational motion of the solvent molecules then would give rise to distortions of either the length of the D-A spacing or the reorganization energies. For **3**–**5** $k_{CS}(E_{exc} = 2.5\,\text{eV})$ is already lowered, compared to **2**. Consequently, the dependence of $1/k_{CS}$ on the which vibrational level within the electronic S_1 state is excited, is a lot less pronounced. For higher excitation energies, the dynamics of the S_1 excited state are influenced, presumably again by solvent effects. The above findings strongly demand further investigations to disentangle the intricate interplay, e.g., solvent-molecule interactions, leading to the observed dependence of excited state dynamics on excitation energy.

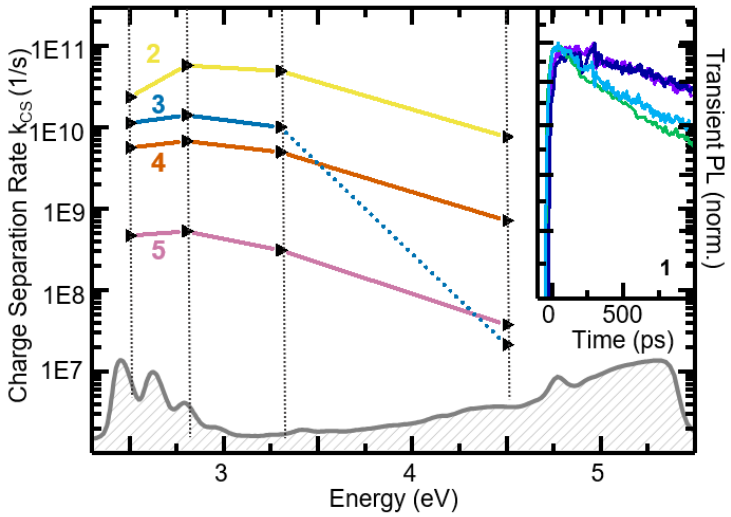

Figure 4.9: Semi-logarithmic plot of the k_{CS} determined by TRPL measurements for samples **2b** (squares), **3** (circles), **4** (up-pointing triangles) and **5** (down-pointing triangles). The dashed vertical lines indicate the respective excitation energies into the S_1 and higher energy S_x absorption regions. Inset: Excitation energy dependence of the reference sample **1** plotted on a logarithmic scale. The color of the traces represent the color of the respective excitation wavelength. A clear increase of lifetime (fitting yields a 1.7-fold increase from 2.5 eV to 4.5 eV) with excitation energy is observed.

Sample **3** displayed a puzzling behavior when excited in the ultraviolet (UV) spectral range. In the case of excitation at 4.5 eV, an irreversible transition occurs, leading to a remarkable increase in PL intensity, while at the same time k_{CS} is strongly quenched (cf. dashed line in Fig. 4.9). From mass spectroscopy it becomes clear that the most likely explanation lies in a bond cleavage of the bon connecting the PDI backbone and the D group. However, it is unclear why this behavior is exclusively observed for the

sample bearing the C_2 spacer.

4.4 Conclusions

In summary, the characterization of new PDIs, chromophores with a directly nitrogen bound donor -NR2 attached to the acceptor perylene imide core was studied. In particular, a well soluble **2** is investigated, which is isoelectronically related to reference "swallowtail" **1**. These PDHs with very short donor-acceptor distances exhibit a very efficient PL quenching. The process responsible for PL quenching in unprotonated compounds could be attributed to the MO associated with the terminal amine at an energy intermediary to the π and π^* orbitals; protonation and/or methylation are expected to reduce the energy of this MO to below that of the π and π^* orbitals, reducing the PL quenching. However, upon protonation, only a weak recovery of PLQY is observed, despite DFT calculations predicting elsewise. This behavior was attributed to a intramolecular hydrogen bond between the D-centered proton and the carbonyl oxygen. By this, the protonation effect is disabled and consequently PL recovery is absent. The intramolecular CT was analyzed in a series of samples with the donor linked to the PDI acceptor core via a varying number of -(CH_2)- spacer groups, thus at distinctively different distances. Control of the CT across the intramolecular interfaces is achieved by three different methods. D methylation proved to be the most efficient, as indicated by quantum efficiency and time-resolved measurements. The donor-acceptor distances for the ground and excited state compounds are determined by DFT and TDDFT calculations, and used to calculate ΔG^{CS}. The elongation of the spacer effectively prevents overlap of the donor and acceptor orbitals. The observed exponential distance dependence is in accordance with a through-space type mechanism. This experimental observation is unaffected by spurious effects in the spacer units from, e.g., delocalized π-electron systems. The excitation energy dependence of k_{CS} reveals the intricate interplay of charge-separation and IC processes. The pronounced non-single-exponential decay dynamics infer the presence of a dark shelving state within the system as extrinsic effects can be excluded. The CSS was succesfully identified as aforementioned shelving state. Furthermore, the excitation-energy dependent decay dynamics and revealed that even in comparetively low polar media, solvent reorganization can have a significant impact on excited state dynamics.

5 Correlation of Structural and Optical Properties in PEN-PFP Heterostructures

In the following chapter, the promising model system PEN-PFP is introduced. Initially, the assigment of the absorption signatures of the unitary PEN and PFP thin films is performed. The identifed signatures are compared to those found in three different heterostructure samples. A new signature at ≈1.55 eV is assigned to a CT transition at the PEN-PFP interface. The careful analysis of PLE measurements shows that the CT state has appreciable oscillator strength in all three heterosystem samples. Most promonently, the absence of any PFP-related signatures in the PLE measurements of the heterostacks hints that population of the CT state by hole-transfer does not occurs. This implies, that the commonly employed picture of unperturbed MOs might not hold in the case of PEN-PFP heterostacks.

5.1 Sample Growth and Structure

Three different PEN-PFP heterosystems are investigated in the following, with all samples having a nominal thickness of 40 nm. Firstly an intermixture blend of both molecules in a stoichiometrically equivalent ratio with exclusive upright molecular orientation. Secondly, to probe the influence of molecular orientation, two different layered heterostacks, will be investigated. In either case 20 nm of PFP were grown on top of 20 nm PEN, with the constituent molecules uprightly oriented in the “standing” sample and a lying molecular orientation in the “lying” sample.

For the PLE measurements all samples were prepared on silicon substrates. In order to measure the absorption spectrum in a transmission geometry, the samples need to be grown on a transparent substrate. In this case, SiO_2 and graphene-coated fused silica[1] are used as substrates. On bare Si(001) and SiO_2, both, PEN and PFP adopt a standing molecular orientation. PEN crystallizes in the thin-film [66] phase while PFP crystallizes in the Siegrist-phase [67]. In the case of graphene-coated substrates, the situation is changed: Both systems adopt a lying orientation, which is the Campbell-phase [68] of PEN. For PFP a π-stacked polymorph is found. Here, the molecules are slip-stacked and growth is perfectly planar, i.e., the molecular plane is parallel to the substrate. This is not the case for PEN, where the molecules are slightly tilted about the short axis.

Remarkbly, in multilayer structures such as the the heterostructures studied here, the bottom layer can also induce the polymorph of the layer deposited on top. Hence, for a PEN bottom layer grown on, e.g., graphene-coated fused silica, a PFP top layer will crystallize in the π-stacked polymorph. Hence, the (substrate templated) bottom layer acts as template for the top layer. This effect also is observed for all other mutual orientations and substrates. A detailed description of the growth procedure and structural characterization can be found in Ref. [69].

5.2 Identification of Unitary Film Resonances

The linear absorption spectra are obtained with an alteration of the PLE setup introduced in Chap. 3.3. A tungsten halogen lamp is focussed onto a pinhole aperture of 100 µm diameter which, in turn, is imaged onto the sample. The magnification is chosen such that the spot size corresponds to that in the PLE measurements.

A detailed analysis of the spectra of the respective four unitary films and comparison with intermixed and stacked samples allows an assigment of unitary signals to those observed in the heterosystems. The absorption spectra of the three standing samples are shown in Fig. 5.1(a). The spectra of PFP and PEN dissolved in dichlorobenzol (DCB) are given for reference. Comparing the lowest-lying resonance in solution, the peak at 1.94 eV is assigned to the slightly red-shifted HOMO-LUMO transition. The

[1] Graphenea, Spain

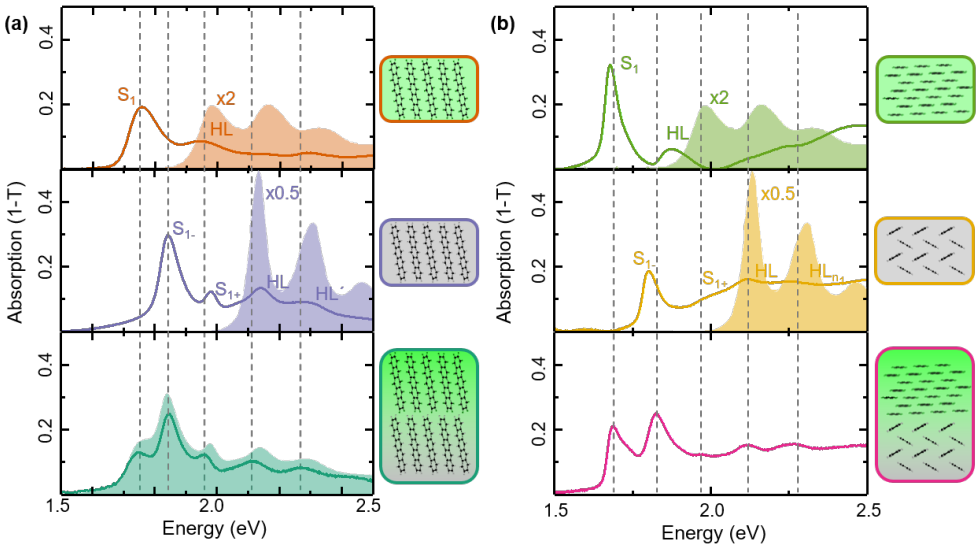

Figure 5.1: Linear absorption measurements of the unitary PFP (top panels) and PEN (middle panels) films, respectively, and the two heterostack samples (bottom panels). In part a), the spectra for the standing molecular orientation are given, while b) shows those for lying case. The linear absorption for PFP and PEN dissolved in dichlorobenzol is given for reference (shaded areas). The shaded areas graphs of the heterostacks are obtained by summing the absorption of the respective constituents. The dashed vertical lines indicate the position of resonances in the heterostacks and illustrate the minor shifts in peak positions compared to the unitary samples. The measurements were performed with a spatial resolution of approximately 100 µm and at a lattice temperature of 20 K.

next two resonances observed in solution are the equidistantly spaced vibronic progressions of the HOMO-LUMO transition, spaced by (180 ± 10) meV. They appear in the thin film spectrum as weak shoulders, again slightly red-shifted by approximately 40 meV. Now turning to the lowest excitations observed, the peak at 1.76 eV can be assigned to the Davydov split exciton resonance. Davydov splitting in Siegrist-phase PFP amounts to 25 meV [70], but is not resolved here due to the limited spatial resolution of the setup and small size of crystalline domains. For the standing PEN [middle panel in Fig. 5.1(a)] the assignment of the resonances is unambigious. In contrast to PFP, no solvent-to-crystal shift is observed in PEN. In line with literature, the peak at 2.14 eV is identified as the molecular HOMO-LUMO transition [71]. The excitonic resonace resides at 1.85 eV with the higher energy Davydov component at 1.97 eV. The difference of the two components amounts to 120 meV and is thus large, compared to

PFP. In general, Davydov splitting is attributed to dipole coupling of translationally noninvariant adjacent molecules in the unit cell. As both, PFP and PEN adopt a very similar crystal structure it is highly unlikely that the orientation of the transition dipole moments alone is sufficient to explain the fivefold difference in Davydov splitting between PEN and PFP, respectivley. As theoretical calculations show, the magnitude of splitting depends strongly on the amount of mixing between Frenkel and CT states [72–75]. Also, it is predicted that a significated planar delocalization of the lowest excitons - and thus increased CT character - exists in PEN.

Table 5.1: Overview of transition energies observed in the absorption spectra of the dissolved PFP and PEN and from the unitary films as obtained by fitting the spectra with multiple Gaussians (see text for details).

Sample	X_+ (eV)	X_- (eV)	HL (eV)	$HL_{1\nu}$ (eV)	$HL_{2\nu}$ (eV)
PFP in DCB	-	-	1.98	2.16	2.34
PEN in DCB	-	-	2.14	2.31	2.48
PFP standing	1.76	1.79 (not resolved)	1.94	2.14	2.29
PEN standing	1.85	1.97	2.14	2.31	2.38
PFP lying	1.67	-	1.87	2.23	2.43
PEN lying	1.8	1.98	2.12	2.25	-

For the samples in lying configuration [Fig. 5.1(b)] the assigment of the resonances is again straightforward. The peak labeled "HL" is again related to the HOMO-LUMO transition of dissolved PFP. Intruigingly, the redshift is even further increased, when compared to standing PFP, and amounts to 100 meV. As mentioned, PFP grown on graphene adopts a π-stacked polymorph with the molecular plane parallel to the substrate. Consequently, as already elaborated in Chap. 2.2.1, no Davydov splitting occurs due to the essentially parallel oscillators. This is evident when comparing the linewidths of the excitonic resonance of standing and lying orientation, the width being significantly narrower in the latter. This is attributed to the missing higher Davydov component, which, although not resolved, leads to the broadening of the excitonic signature in the standing configuration. For lying PEN, the peak related to the HOMO-LUMO transition again is found at 2.14 eV, with no apparent solution-to-crystal shift. Also, the intensity of the lowest resonances is reduced, compared to their standing counterparts. This is due to the tilt of the short molecular axis where the transition dipole of the lowest excitation resides. The lowest lying absorption in both stacks is attributed to the PFP exciton at 1.69 eV for the lying sample. The PEN exciton is

observed 1.82 eV in the lying sample. The higher lying Davydov component is found at 1.96 eV.

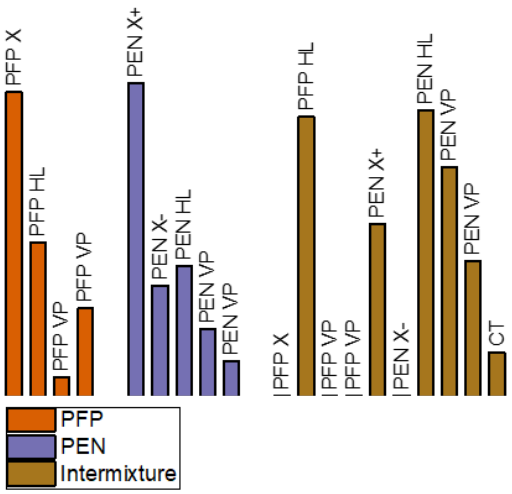

Figure 5.2: Transition strengths of the different signatures in unitary standing PFP and PEN, respectively, as well as in the PFP-PEN intermixture. The values were obtained by fitting multiple Gaussians to the absorption spectra and are normalized to the most pronounced transition in each of the three cases. See text for details.

The following section will deal with the intermixed sample. The absorption spectrum is presented in Fig. 5.3. It shows numerous resonances which seem to be significantly shifted with respect to the unitary films or even completely new in their nature. To shed light on this aspect, the absorption data of all three are further analyzed. To this end, the respective spectra for standing PEN and PFP are normalized and fitted by multiple Gaussians in the energy range from 1.4 eV to 2.5 eV. In the case of PEN, five Gaussians are used (the two Davydov components along with the HOMO-LUMO transition and its respective two observable vibronic progressions), in the case of PFP the number reduces to four, because the Davydov splitting is not resolved. As a next step, the intermixed sample is described by the nine Gaussian oscillators of PFP and PEN. For the fitting process the energetic positions of the transitions of the unitary films are fixed, allowing a $\pm 2\%$ tolerance. The tolerance range is chosen to account for minor energetic shifts due to structural difference between the unitary films and the intermixture. For the intermixed sample an additional Gaussian oscillator had to be included to reach a satisfactory level of fitting ($R^2 \approx 0.99$) in order to fit the low

energy level new peak at around 1.55 eV. The results of the fitting procedure are also given in Tab. 5.2.

Table 5.2: Peak energies from the unitary films used to fit the absorption spectra of the three heterostructutes.

Sample	CT (eV)	E_2 (eV)	E_3 (eV)	E_4 (eV)	E_5 (eV)	E_6 (eV)	E_7 (eV)
intermixture	1.58	1.74	1.89	2.1	2.24	2.42	
lying heterostack	-	1.67	1.83	1.97	2.12	2.26	(2.36)
standing heterostack	-	1.76	1.85	1.96	2.11	2.27	2.44

The fact that the transition at 1.55 eV is unique to the intermixed sample and that it cannot be fitted as superposition of unitary film transitions is taken as clear evidence that it arises from intermolecular coupling between PEN and PFP. Tentatively, the peak is assigned to a CT transition. The transition strengths of the different signatures in standing PFP and PEN, respectively, as well as in the PFP-PEN intermixture are shown in Fig. 5.2. For unitary PFP and PEN the respective relative intensities are rather similiar. In the case of the intermixture the peaks likely related to the respective PFP and PEN HOMO-LUMO transitions (and vibronic progressions thereof) are most pronounced. In the intermixture the intensity of excitonic PFP and PEN signatures is drastically altered: the PFP excitonic signature vanishes entirely, as does the higher energy Davydov component of PEN. On the other hand, the lower energy component remains at a significant intensity (cf. Fig. 5.3). However, as it is only separated by 30 meV from the PFP HOMO-LUMO, an assignment to either of the two is not necessarily unambigious. The actual intensity of the PEN excitonic contribution might be substantially lower. One has to bear in mind that the fitting process and relating of unitary signals to those found in the intermixture is no definitive evidence and could lead to false conclusions. There is, nevertheless, no question that the resonace at 1.55 eV is unique to the intermixed sample and likely due to intermolecular CT transition. Comparing the absorption spectrum of the intermixture with those of the two heterostacks it becomes evident that the low-energy transition at 1.55 eV is entirely absent in the heterostacks. This is however not unexpected as the interfacial region where the two constituent molecules “meet” is comparatively small with respect to the intermixed sample. This also manifests the very high structural quality of the samples indicating high interface smoothness and only short ranged intercalation between the

bulk of PFP and PEN.

Despite not being observed in absorption, it is known from PL experiments that the CT state is also present in the heterostacks [76]. To this end, a high-sensitivity technique such as PLE can be employed to gain further information on the absorptive behavior.

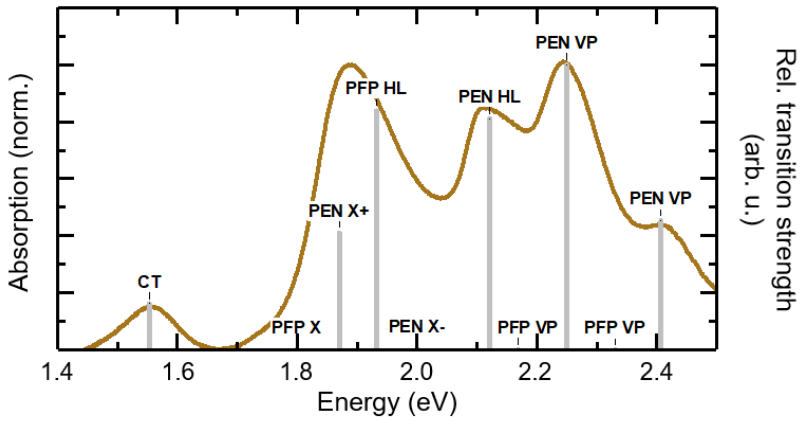

Figure 5.3: Linear absorption of the intermixed film showing the new resonance at 1.55 eV which is tentatively attributed to a PEN-PFP CT transition. The overlay (grey bars) shows the relative contributions of the signatures from the unitary films to the total absorption signal, taken from Fig. 5.2.

5.3 Coupling of the Lowest-lying States to the CT State

To gain further information on the CT state in the heterostacks, PLE measurements are performed on the three heterosystem samples. If the CT state is present in the stacks, it is also expected to show in the PLE measurements as the quantum yield of the CT state is assumed to be comparatively high in the case of direct (resonant with the CT transition at $E \approx 1.55\,\mathrm{eV}$) excitation.

The spectra in Fig. 5.4 show the absorption and PLE measurements for the intermixed sample [panel (a)], and the standing and lying heterostack [panels (b) and (c) respectively]. As shown in the previous section, in the intermixed sample, the lowest lying PFP and PEN exciton lines vanish or are at least diminished. The emerging resonance at 1.88 eV can either be interpretated as superposition of the weakened PEN lower

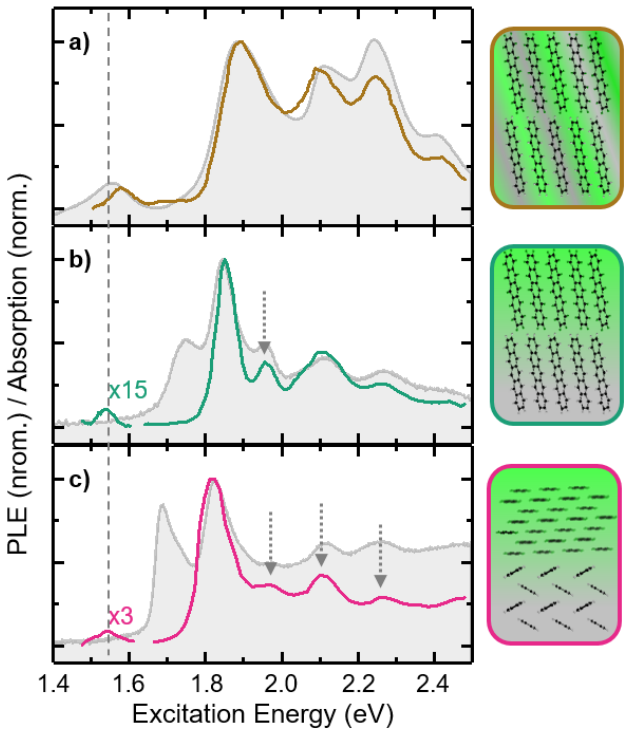

Figure 5.4: Comparison between the absorption (light grey) and PLE (colour) spectra for the intermixed heterostructure (a), the standing (b) and lying (c) heterostack, respectively. The dashed grey line indicates the energetic position of the CT exciton. The PLE detection was set to 1.38 eV in all three cases. The PLE spectra are scaled by factors of 15 and 3 for the standing and lying structures for clarity.

energy Davydov component and PFP HOMO-LUMO transition or alternatively as a new intermolecular exciton line. All peaks observable in absorption are reproduced in the PLE spectrum. Additionally, the intensities in absorption and PLE measurement match in the energy range from 1.8 eV to approximately 2.1 eV. This indicates that all states are coupled to the emissive CT exciton with constant efficiency. For energies above 2.1 eV, the intensity of the PLE spectrum is reduced compared to the absorption spectrum. This can be explained in the following way: for higher excitation energies the energy difference between excited state becomes very large. Hence, more surplus energy has to be dissipated as heat and the likelihood of a non-radiatve recombination increases. One noteworthy deviation is the minor blue-shift of the CT peak from 1.55 eV (absorption) to approximately 1.56 eV (PLE). The blue-shift is accompanied by an apparent narrowing of the PLE linewidth.

Next, the heterostack samples [cf. Fig. 5.4(b) and (c)] are considered. As initially mentioned, the quantum efficiency under direct excitation is assumed to be fairly high. This assumption proves to be justified, as the CT-related resonance at 1.55 eV is clearly observed in the PLE spectra of both the standing and the lying heterostack. Comparing the respective intensities reveals information on the microscopic processes at the internal interfaces. A significant difference is found in the PLE signal strength, the sample with lying molecular orientation showing a by far higher intensity. This is in line with previous results [76] in which the same trend was observed, in this case the signal strength of the CT PL was measured. The increased signal strength is linked to an increased electronic coupling between the molecules at the interface. In the lying heterostack sample, the π-electron systems can efficiently overlap due to the face-to-face orientation of the molecules. Contrastingly, in the head-to-head molecular arrangement of the standing counterpart, this overlap is greatly diminished. An alternative explanation for the increased PL intensity is given by taking into account the orientation of the transition dipole moment (TDM) of the respective higher energy ($S_3 \leftarrow S_0$) transition. The TDMs are oriented parallel to the long molecular axis for both, PEN and PFP. Hence, the absorption efficiency (at $E_{exc} = 3\,\mathrm{eV}$) is increased in the lying heterostack, compared to the standing one. By the following argument, the second interpretation can be dismissed in favour of the first: For the CT PL a 4.8-fold increase was measured when comparing standing and lying heterostacks. However, the PL intensity of the transition related to the PFP exciton is increased only 1.7-fold. Consequently, the difference cannot be explained solely by enhanced absorption in the lying heterostack or alternatively by possible experimental uncertainties. The PLE measurements strongly support the assumption of increased electronic coupling caused by π-stacking at the internal interface. A 4.4-fold increase is obtained when comparing the intensity of the CT-related PLE signals of lying and standing heterostacks. This result is in very good agreement with the observed increase in CT intensity from the PL measurements [76].

The most striking feature regarding the PLE measurements is the lowest lying peak in the absorption measurements, the transition assigned to the PFP exciton. This transition is completely absent in the corresponding PLE spectra of the standing and lying heterostack. In contrast, the resonance attributed to the PEN exciton is present in both spectra. According to Eq. (3.14), the PLE signal is proportional to the product of $\alpha(\lambda)$, the absorption probability, and $\gamma(\lambda)$, which describes the relaxation efficiency

to the emissive state. A vanishing PLE signal thus infers that at least one of the two factors must be zero. Consequently, it can be assumed that the PFP exciton is not coupled to the CT state. To phrase this finding differently, population of the CT state by hole-transfer from PFP is not observed. Moreover, the PLE intensity is diminished in all spectral regions in which PFP predominantly absorbs the incident light [indicated by the arrows in Fig. 5.4(b)-(c)]. This indicates that the excitations created in the PFP part of the heterostructure are decoupled from the CT state.

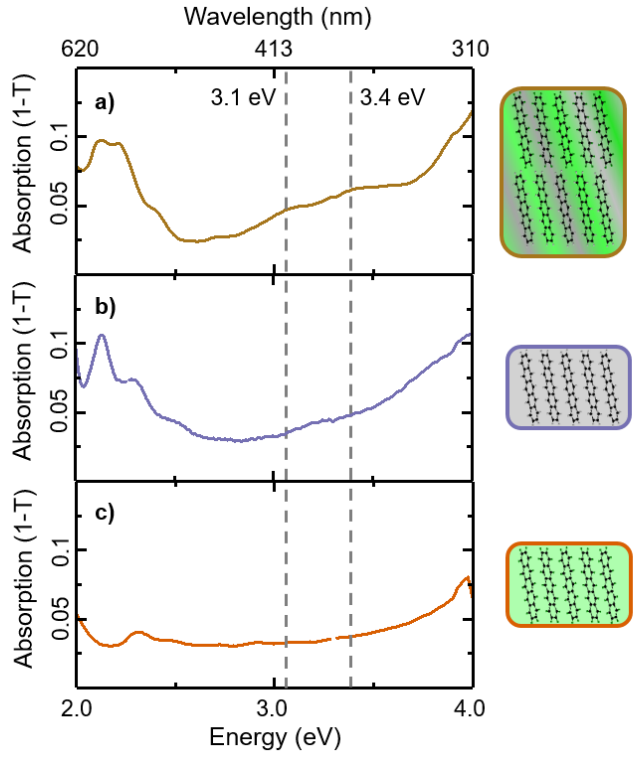

Figure 5.5: (a) Linear absorption measurements for the intermixed sample, as well as the two respective unitary films [(b) and (c)], which are given for reference.

Next, the higher energy absorption spectra are considered. The linear absorption spectra from 2.0 eV to 4.0 eV are given in Fig. 5.5. The intermixture [Fig. 5.5(a)] shows two pronounced resonances at 3.1 eV and 3.4 eV. These resonances are absent in the unitary PEN and PFP films. Moreover, the spectra feature no distinct resonances at all between 2.5 eV and 3.5 eV. Only a very weak resonance is observed at 3.2 eV in the standing PEN. However, none of the higher energy signatures is observed in the heterostacks. This can again be explained by the small volume in which the both

constituents interface. Similiary to the absorption measurements in the lower energy spectral region, the sensitivity of the linear absorption experiment is again to low too measure this interfacial effect. This strongly demands PLE measurements to be performed for excitation energies >3 eV which are unfortunately inaccessible with the experimental setup used in this thesis.

5.4 Implications for the Nature of the CT State

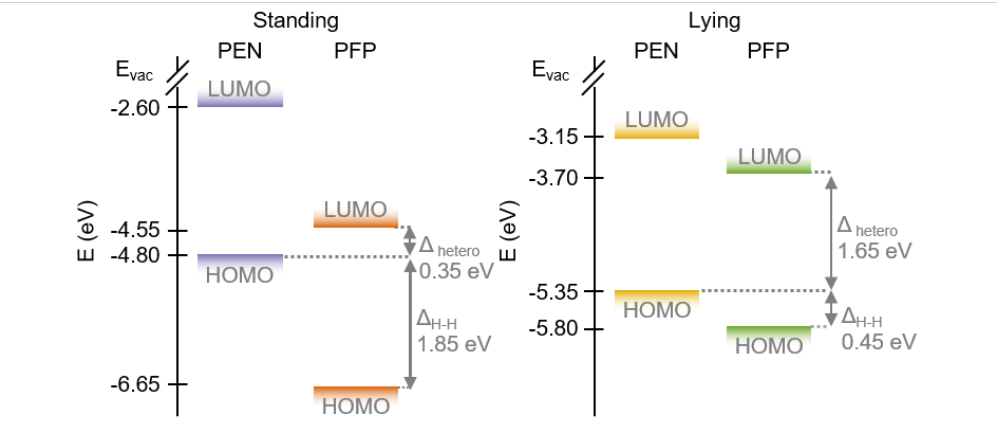

Figure 5.6: Energy level diagram for standing PFP-PEN heterostacks. The HOMO levels are determined by UPS for samples grown on silicon substrate. The LUMO level is taken from the literature values for the transport gap (= 2.2 eV) in the case of PEN. In the case of PFP it is approximated from the optical gap assuming the same exciton binding energy as in PEN (E_B = 0.35 eV) due to lack of experimental values. Data taken from Refs. [13] and [77].

The classical understanding of CT excitons relies on the energy difference between donor HOMO and acceptor LUMO. A simple expression for the energy of a CT state is given by [7]:

$$E_{CT} = q\left(E^{ox}(D) - E^{red}(A)\right) - \frac{e^2}{(4\pi\epsilon_0\epsilon_s r_{DA})} - \frac{e^2}{(8\pi\epsilon_0)}\left(\frac{1}{r_D} + \frac{1}{r_A}\right)\left(\frac{1}{\epsilon_s} - \frac{1}{\epsilon_{ref}}\right) \quad (5.1)$$

This expression strongly resembles Eq. (2.24), which was used to estimate the Gibbs

free energy change for the formation of the CSS in Chap. 4.2.2. While Eq. (5.1) can yield accurate results for CT complexes in solution or supermolecular donor-acceptor units, its use is rather limited in solid-state D-A systems. In the solid state, additional factors such as polarization effects and charge-carrier delocalization have to be considered. Also, as the molecules are in a fixed position, interface geometry and molecular anisotropy have to be accounted for. A more precise description of the energy of the CT-state is given by the following expression:

$$E_{CT} = I_D - E_A - E_C(r) - E_P, \tag{5.2}$$

where I_D is the ionization potential of the D and E_A the electron affinity of the A. $E_C(r)$ is the Coulomb attraction energy between the electron and the hole separated by a distance r. Finally, E_P accounts for the polarization energy of the lattice caused by the (polar) CT exciton. The ionization potential describes the energy required to remove an electron from the highest occupied state; in other words, it defines the energy level of the HOMO with respect to vacuum level. I_D is experimentally accessible through PES, whereas E_A can be obtained by means of inverse photoelectron spectroscopy (IPES) or electron energy loss spectroscopy (EELS).

For the PFP-PEN system, the level aligment is shown in Fig. 5.6 for the standing and lying configuration, respectively. Notably, the respective HOMO levels of PFP and PEN are shifted in opposite directions when going from the standing to the lying configuration. As a consequence, the offset between the PEN HOMO and PFP LUMO, denoted Δ_{hetero} in the following, also drastically varies. In the case of standing stack it amounts to approximately 0.35 eV, whereas for the lying case it increases to 1.65 eV. According to the UPS data presented in Fig. 5.6, the energy of the CT should differ by more than 1.0 eV between the standing and lying configurations. The optical experiments, however, show only minor changes in the energetic positions of the transitions assigned to the CT. This is universally true for all applied techniques, absorption, PL, and PLE spectroscopy, and also for all three heterosystem samples under study. The energies determined from the optical experiments locate the CT at 1.55 eV in absorption and at 1.4 eV in emission. While $\Delta_{hetero}(lying) = 1.65\,\text{eV}$ is large enough to possibly be in agreement with the results presented here, this is not the case for $\Delta_{hetero}(standing) = 0.35\,\text{eV}$. The determination of the IE values is problematic due to the limited escape depth of the electrons in UPS measurements. Thickness

dependent measurements reveal that the spectra of the stacked samples are purely weighted superpositions of the unitary films with no energy shifts or novel spectral features [13]. Hence, a bending of the HOMO bands towards the mutual interface, which could potentially solve the energy level alignment issues, does not occur. To summarize, this indicates the shortcomings of a model relying on E_{CT} being solely constituted of the superposition of the unperturbed HOMO and LUMO of the donor and acceptor molecule, respectively.

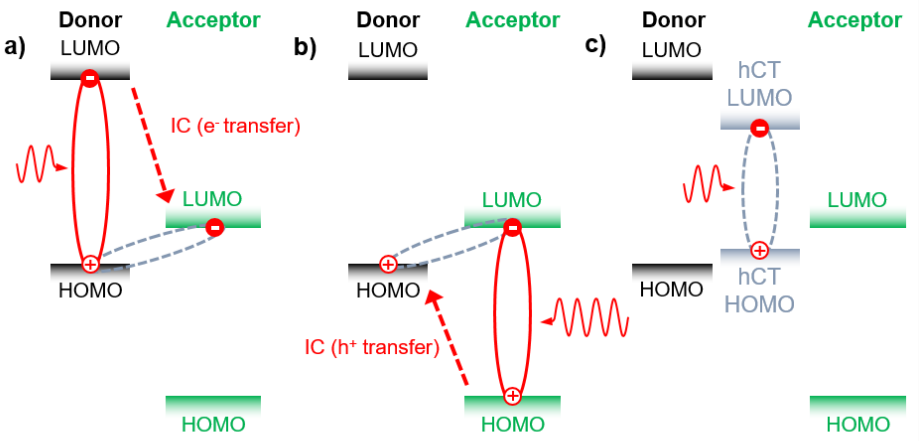

Figure 5.7: Possible excitation pathways leading to the excitation of an interfacial (CT) state at the PEN-PFP heterojunction. (a) shows the case of an ET process from the D to the A, while in (b) the case of a hole-transfer is illustrated. In (c) the case of direct excitation of the CT state is shown. They are denoted as hybrid CT orbitals (hCT) to point out that they possibly constitute newly formed hybrid MOs at the interface, similiar to those observed in the intermixture.

The results obtained by the PLE measurements corroborate the assumption of a newly formed interfacial CT state. In general, three different pathways are expected to lead to a population of this state: a) electron-transfer from the electron donor moiety, b) hole-transfer from the electron acceptor moiety, and c) direct (resonant) excitation of the CT. Fig. 5.7 illustrates these three pathways. While emission from the CT state is observed in the case of direct excitation and via excitation of into the PEN resonances, all transitions related to PFP are absent in the PLE spectra of the CT emission of both,

the standing and the lying heterostack, respectively. The prelinary results obtained for the higher energy resonances in the intermixture hint that direct excitation of the CT state might also be possible from the PFP ground state.

To date, no ab initio calculations of interfacial CT excitons in the PEN-PFP heterosystem exist. The results presented here demand strong efforts to be made in this field. While the interpretation of a newly formed state at the interface is conclusive, its nature needs to be thorougly investigated both, theroretically and experimentally. Especially questions of band bending of excitonic bands and coupling efficiencies to the newly formed CT state need to be addressed.

6 Charge-Transfer Across Internal Interfaces: PEN-Fullerene C_{60}

In the final chapter, another promising material system is introduced: The PEN - Buckminster-fullerene (C_{60}) heterosystem is being discussed as material class for highly-efficient OPV cells. While the majority of research studies deal with blends of PEN and C_{60} or closely-related polymers in combination with derivatives of Buckminster-fullerene, very few are focussed on ordered heterostructures and actual interfacial properties. To this end, the linear optical properties of the individual constituents and the heterostacks will be discussed, followed by TRPL measurements in order to determine the decay dynamics of the excited states. The results also indicate a distinct PL signature which is found exclusively in the heterostructures and is thus possibly related to a PEN-C_{60} CT transition. Further, the PL dynamics of C_{60} show non-negligible changes in the presence of an underlying PEN layer.

6.1 Sample Growth and Single Molecule Properties

The samples under study in this work were prepared by Dr. Tobias Breuer and Andrea Huttner from the group of Prof. Dr. Gregor Witte. All samples under study are grown by (organic) molecular beam epitaxy (OMBE).

The properties of PEN have been treated in the previous chapter to which the reader is referred. Here, only a brief introduction of the structural and electronic properties of C_{60} is given. Buckminsterfullerene is the chemical compound with the formula C_{60} (molecular weigth: $720.66\,\mathrm{g\,mol^{-1}}$). Its structure resembles that of a football (soccer ball), consisting of twenty hexagons and twelve pentagons. The carbon atoms are

located at each vertex of the polygon. In the solid phase C_{60} adopts a face centered cubic (FCC) crystal structure with a room temperature lattice constant of 1.415 nm [78]. For individual molecules in solution the PLQY is on the order of 10^{-4} while it increases to 10^{-3} in the condensed phase. The main decay channel for excitations is an ISC process to the T_1 level at 1.55 eV [79]. The lowest lying dipole transition is parity forbidden and found at an energy of 1.85 eV. The value of the transport gap is still under discussion but it is expected to be at 2.6 eV [80, 81].

When grown on a silicon substrate, PEN adopts the thin-film phase. Here, the molecules are uprightly oriented. If the substrate is coated with a monolayer of graphene, PEN alters its molecular orientation. In this case it adopts the Siegrist phase where the long axis of the molecule is aligned parallel to the substrate. Unlike the case of PEN-PFP interfaces introduced in the previous chapter, a templated growth is not possible in the case of PEN and Fullerenes. The latter two molecules are structurally far less compatible, e.g., differing remarkbly in shape (PEN: rod-like; C_{60}: spherical), size, and intrinsic isotropy. In order to achieve a well-defined internal interface, special care must be taken during sample growth. For instance, when C_{60} is grown on top of PEN, the C_{60} film homogenity strongly depends on growth parameters, e.g., substrate temperature. A two-dimensional C_{60} distribution is achieved only for samples grown at cryogenic temperatures [20]. The homogenity also depends on molecular orientation of in the underlying layer. Uprightly oriented PEN induces crystalline growth of C_{60}, while a bottom layer of lying PEN molecules results in a more amorphous C_{60} layer. A similiar effect is obtained when growing C_{60} as bottom layer and subsequently depositing PEN on top. The choice of substrate will substantially influence sample homogenity and crystallinity, e.g., larger crystallites are achieved for growth on NaCl, compared to silicon substrate.

The interface region makes up only a small fraction of the entire sample volume. Thus, the majority of the sample can be considered bulk PEN and C_{60}, respectively. Additionally, no evidence for mutual intercalation of molecules was found in a study on the structural properties of the heterosystem [21], despite it beeing theoretically proposed for some growth scenarios [82]. Intercalation of molecules could increase the effetive interfacial area. As no intercalation is observed, a “sharp” molecular interface is assumed [21].

6.2 Linear Absorption and Photoluminescence Excitation

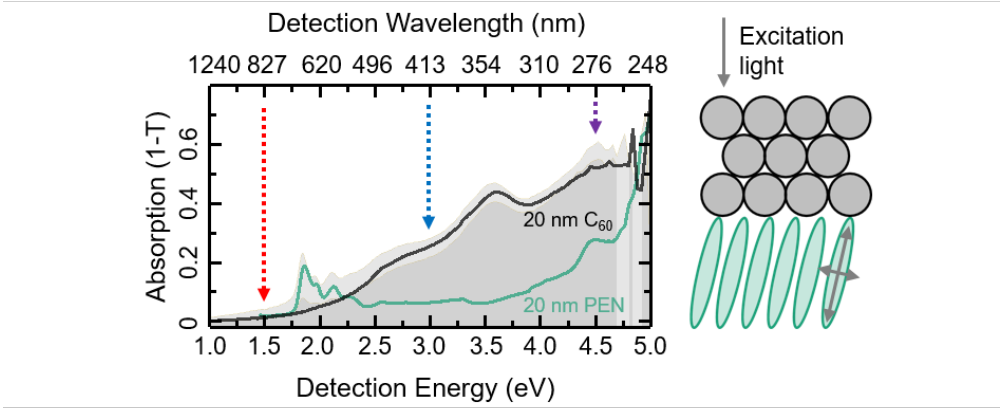

Figure 6.1: Linear absorption spectra of unitary PEN and C_{60} films of 20 nm thickness each. For reference also the absorption spectra of two heterostructures (5 nm PEN + 20 nm C_{60} and 20 nm PEN + 20 nm C_{60} respectively), indicating that the absorption of the heterostacks is in good agreement a superposition of the two constituents. The colored arrows indicate the three distinct excitation energies used in Chap. 6.4.

In Fig. 6.1, the linear absorption spectra for the unitary PEN and C_{60} films, as well as that of two heterostacks are shown. For the assignment of peaks for the PEN film the reader is referred to Chap. 5.2, as the samples are structurally indentical. For the C_{60} sample, two distinct resonances at 2.7 eV and 3.6 eV are observed. These are in concurrence with the literature and correspond to band-to-band transitions deriving from the molecular energy levels, i.e., they are related to the molecular HOMO-n - LUMO+m ($n, m \geq 1$) transitions [83]. The HOMO-LUMO transition, i.e., the lowest lying electronic transition is dipole-forbidden in the single molecule. However, in the solid state, structural disorder can lead to distortions of the icosahedral symmetry of the C_{60} molecules and thus the lowest transitions become partially allowed [84]. Consequently, a lack of observable low energy transitions can be interpreted as an effect of low disorder. Additionally, the Urbach energy, obtained by fitting of the low energy absorption tail [cf. Fig. 6.1(b)] amounts to 0.56 eV. As comparison, typical values found in the literature range from 0.35 eV to 1.8 eV [83,85]. This corroborates the assumption that disorder plays a comparitively small role in the systems under study.

Fig. 6.2 shows the the PLE spectrum of the unitary C_{60} sample in the low energy region. The comparison with the absorption measurement (grey shaded graph) directly reveals that indeed distinct resonances in the low energy region can be observed. This again demonstrates the superior sensitivity of the PLE technique. The lowest energy peak in the PLE spectrum is located at 1.86 eV. In turn, the most intense peak in given range of the PLE spectrum, is situated at 2.03 eV, blue-shifted by approximately 175 meV from the 1.86 eV peak. The same amount of shift, however in opposite direction, is observed for the most prominent peak in the PL spectrum, located at 1.7 eV. It can thus be concluded that the 1.86 eV peak marks the position of the the purely electronic 0-0 transition [84,86]. Its very low intensity again underlines the dipole forbidden character. However, the transitions can gain significant intensity when a vibrational mode is involved in a Herzberg-Teller (HT) (vibrational) coupling scheme. This mode has been identified as the t_{1u} vibrational mode [87] at a frequency of 1437 cm^{-1}, identified as IR active mode [87, 88]. Other studies have reported a doublet structure energetically separated by 30 meV, for each of the peaks. This structure is not reproduced here.

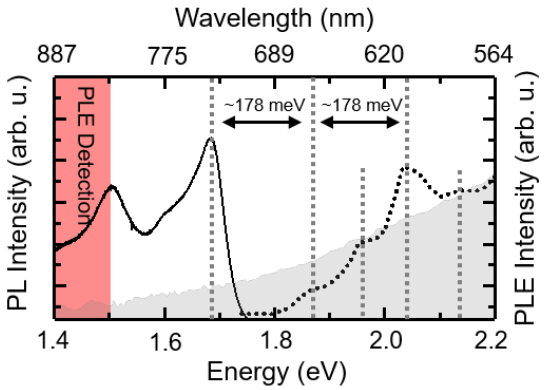

Figure 6.2: PLE (dots) and PL (solid black line) spectra of the unitary C_{60} film taken at a lattice temperature of 20 K. For comparison the linear absorption spectrum of that same film is also given (grey shaded area). The PLE detection window is indicated by the shaded red area.

6.3 Interfacial Effects in the Heterostacks

Now turning from the unitary film to the properties of the PEN-C_{60} heterostacks, the low-temperature PL spectra are presented in Fig. 6.3. In line with the values found in the literature for C_{60} thin films, three main resonances are identified at 1.7 eV, 1.62 eV, and 1.52 eV, respectively [83, 86, 89–91]. In the context of a HT coupling scheme, the peaks at 1.7 eV and 1.52 eV are related to the purely electronic 0-0 transition at 1.86 eV under participation of one (1.7 eV) or two (1.52 eV) vibrational quanta of the t_{1u} mode. This has been theoretically proposed [87] and experimentally evidenced [84]. The origin of the 1.62 eV resonance is not entirely clear.

In the presence of a PEN bottom layer, a slight shift towards higher energies is observable for all three resonances. This shift is tentatively attributed to an altered size of the crystallites [20] and presumably not due to a superimposed PEN signal. PEN can be ruled out because of the low intensity of the PL under the given experimental conditions. Additionally, a peak at ≈1.8 eV appears in the spectrum of the heterostacks. While the obvious conclusion is that this peak is due to PL from the PEN free exciton (FX), the reference measurement (cf. grey shaded graph in Fig. 6.3) curve casts doubt on this conclusion. Again, the intensity is far to weak for the PEN FX to be accountable for this observation.

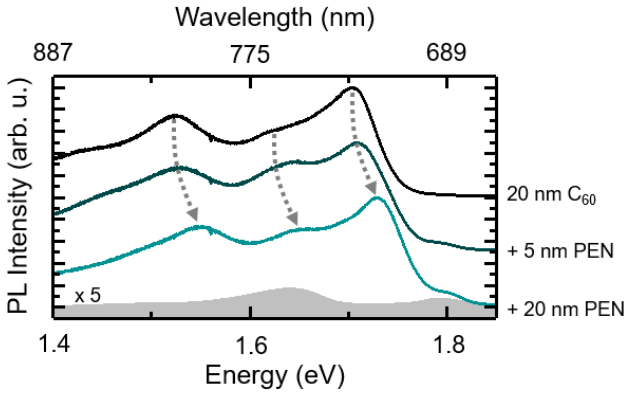

Figure 6.3: Comparison of the low-temperature PL spectra (E_{exc} = 3 eV) of a 20 nm unitary C_{60} thin film (black) and the heterostacks with a 5 nm and 20 nm PEN bottom layer. The grey shaded shows the spectrum of an unitary PEN sample of 20 nm thickness measured under the same conditions.

Next, the temperature dependence of the PL is discussed. The temperature-dependent PL intensities for the unitary C_{60} film and the two heterostacks are shown in Fig. 6.4. To ensure as little contribution as possible from the PEN film, the excitation energy was set to 3.0 eV and a very narrow spectral range around the C_{60} emission maximum was extracted. Intriguingly, the data show qualitative differences, when comparing the temperature-dependent data for the two main PL peaks of the unitary film with those of the heterostructure samples. Apparently, the bulk PL from the C_{60} is influenced by the presence of the PEN film. The two heterostructures show a qualitatively similiar behavior. The PL intensity has a local maximum at around 70 K (as in the unitary film), and subsequently decreases to about 80 % of that value at a temperature of 40 K. The local minimum is followed by the overall maximum value for $T = 22$ K. The PL from the unitary film exhibits a very steep incline from 300 K and 100 K, a plateau is reached with only a moderate increase of PL intensity between 100 K and 22 K. The structure of minima an maxima is not reproduced.

From the fact that PEN alters the temperature dependence of the C_{60} PL, it can be assumed that this effect is related to the mobility of excited species in the bulk of C_{60}. In polycrystalline and disordered media, the exciton diffusion length is generally reduced with decreasing temperature. This is due to the dominant role of thermally activated hopping mechanisms in the transport of excitations. However, band-like transport also occurs, even in disordered systems. Hence, the intricate interplay of the two mechanisms can yield puzzling results when effects related to mobility are studied. In the case studied here, the situation is further complicated by the nature of C_{60}: at elevated temperatures, the C_{60} molecules exhibit a rapid rotatory motion. This motion occurs freely and independently for the individual molecules in the crystal structure. With decreasing temperatures, the angular frequency slows down and the motion becomes discontinuous until the molecules become entirely locked in their orientation. There exist different values for the temperature at which locking occurs, ranging from 250 K [92] down to 100 K [93]. When the angular frequency of the molecules is high, the π orbitals of neighboring molecules do not overlap sufficiently long for mechanical distortions to be transferred or band transport to occur. This implies that the excitations are truly localized on one lattice site. However, when the rotation begins to freeze out, the exciton mobility increases. Thus, the excitons are able to diffuse through the crystal and reach, e.g., defects acting as (non-)radiative recombination centers. Given the results in Fig. 6.4, PEN appears to act as such a defect for the C_{60} excitations. The temperature

at which the local minima occur in the heterostack samples (i.e. ≈40–50 K) is probably related to the overall maximum of exciton mobility. For even lower temperatures, the hopping transport becomes irrelevant and the PL intensity increases again. Whether the quenching is by relaxation of C_{60} excitons to a CT state formed at the PEN-C_{60} interface or induced by "real" structural defects remains unclear. These results also explain in part why such a broad range of exciton diffusion lengths of C_{60} excitons exists in the literature [94–96], the values ranging from 5–40 nm. Experimental conditions and sample structures have to be considered carefully when discussing the complex process of exciton diffusion in C_{60}.

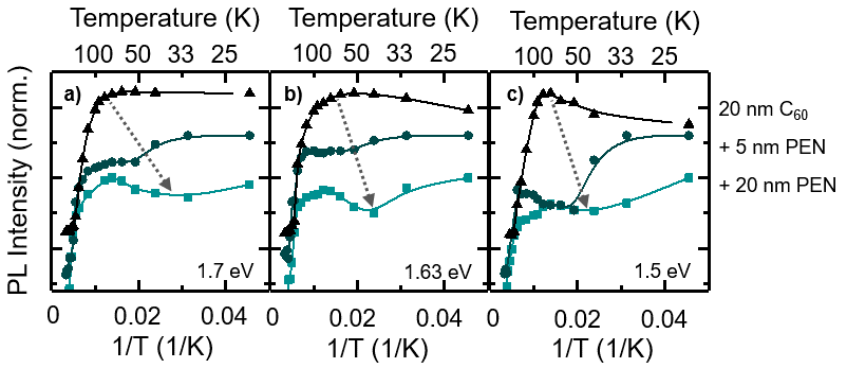

Figure 6.4: Arrhenius plots of the temperature dependence of the PL intensity for a unitary C_{60} film (upward triangles), and heterostacks with 5 nm (down triangles) and 20 nm (squares) PEN bottom layer with a 20 nm C_{60} layer grown on top. The data are extracted for the three main PL peaks at 1.7 eV (a), and at 1.63 eV (b) and 1.5 eV (c), respectively. The individual curves are normalized to the respective maximum and offset vertically for clarity.

To probe the dynamics of the C_{60} excitons, time-resolved PL experiments were carried out. In order to exclusively create carriers in the C_{60} layer, the excitation energy again was set to 3 eV. To further reduce the influence of a possible superposition of PEN and C_{60} signals, the transients were extracted from a narrow spectral window (1.65–1.73 eV) which incorporates the PL maximum of the C_{60}. In this spectral region, the PL intensity of standing PEN is negligible. The transients shown in Fig. 6.5 are for the C_{60} film and for heterostacks with a bottom layer of 5 nm and 20 nm PEN, respectively. For reference, the transients of the PEN FX resonance as well as the self-trapped exciton (STE) measured for a unitary PEN film are also given. The decay of the C_{60} exciton can be described by a single-exponential function with a decay

constant of (881 ± 18) ps. This is in agreement with values found in the literature, which are on the order of 750–1200 ps [97–99]. From the data in Fig. 6.5 it becomes evident, that the PL lifetime of C_{60} excitons is significantly reduced when the substrate is precovered with a PEN film. Further, the magnitude of the lifetime reduction increases with the thickness of the PEN layer. For both, 5 nm and 20 nm PEN coverage, the transients can be fitted single-exponentially to a satisfactory degree ($R^2 \geq 0.97$). The obtained lifetimes amount to (614 ± 8) ps and (417 ± 6) ps for $d_{\mathrm{PEN}} = 5$ nm and $d_{\mathrm{PEN}} = 20$ nm, respectively. It should be noted however, that the transients of the heterostacks are better described non-exponentially (e.g., bi-exponentially). This hints at the complexity of the recombination dynamics occurring in the heterostacks. This is in stark contrast to the case of PEN-PFP, where the lifetimes of the unitary films are unaffected in the stacked samples (cf. Chap. 5 and Ref. [76]).

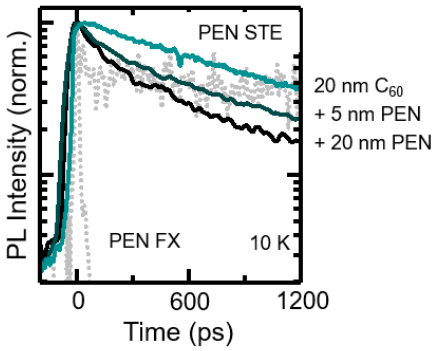

Figure 6.5: Comparison of the TRPL measurements of the C_{60} emission maximum for the unitary C_{60} sample and the two heterstacks. The excitation energy was set to 3 eV and the transients were extracted from a narrow spectral range around the C_{60} PL maximum to ensure a miniscule contribution from the PEN PL.

Hence, already the mere observation of the lifetime quenching is unexpected. Foremost, because the interface and (or) the PEN layer appears to influence the bulk properties of the C_{60}. The interfacial region is small compared to the bulk, and mutual intercalation of the constituent molecules is not observerd [21]. It is thus safe to assume that the quenching must be caused by a long range mechanism. Elsewise, the magnitude of the quenching of the PL lifetime is unexplicable. A frequently discussed quenching mechanism is (Förster) resonant energy transfer (RET). RET is typically efficient on a length scale of 1–40 nm between the two interacting partners. In contrast to photon

reabsorption, RET is not accompied by a spectral shift, i.e., no cutoff of the high energy end of the PL spectrum is observed. Contrastingly, it is characterized by a decrease of PL intensity and altered PL lifetime. This is in line with the data presented here, where only minor spectral shifts are measured. The RET rate can be calculated by the means of Eq. (2.26) and relies on the spectral overlap of (energy) D and A. On the one hand, it can occur between the two molecules of the same type (commonly referred to as homo-RET), in this case RET can promote the migration of excitons through the crystal. On the other hand, a hetero-RET describes the interaction of molecules of different type. Furthermore, the mechanism is not limited to any specific type of (excited) species present in the crystal, as long as the respective D emission and A absorption spectra overlap sufficiently.

In the case of the PEN-C_{60} sample with 20 nm PEN, the quenching efficiency obtained from the TRPL measurements amounts to $E = 1 - \tau_{\text{hetero}}/\tau_{\text{unitary}} = 1 - 417\,\text{ps}/881\,\text{ps} = 0.53$. Under the assumption of homogenous excitation of the sample, and consequently, uniform distribution of excitons in the C_{60} film, the average distance between the D (in this case a C_{60} exciton) and the A ground-state PEN is half the total heterostack thickness, i.e., 20 nm for the thickest heterostack. Hence, the Förster radius R_0, which is defined as the distance of 50% quenching efficiency, would have to amount to $\approx$20 nm. However, the radius calculated by the means of Eq. (2.28) is only $R_0 \approx 1.1$ nm. Consequently, a quenching of the C_{60} lifetime by simultaneous excitation of an PEN exciton is insufficient to account for the magnitude of the observed effect. As mentioned earlier, RET can also occur between an exciton and other excited species, such as individual charges, polaron pairs, or other excitons (in this case the excitons act as their own quenchers). As the interface between PEN and C_{60} is expected to generate CT excitons which ultimately may be dissociated into free charges, the aforementioned species should be present in the system under study. A hole localized on PEN represents a cationic state, whose absorption is typically red-shifted with respect to the ground state absorption. Thus, the comparatively small overlap between C_{60} emission and PEN absorption spectrum would increase. However, such a exciton charge annihilation (ECA) process affords the lifetime of the charges to be on the order of the time interval between to successive excitation pulses ($\approx$12.5 ns). Otherwise, such a cascaded effect would not be observable. ECA to a significant degree has indeed been observed (Ref. [100]) in blended films of organic semiconductors. Additionally, in Ref. [97] ECA has been observed in a C_{60} thin film under different experimental

condition by using a scanning tunneling microscopy (STM) technique and measuring the electroluminescence (EL) in a Hanbury-Brown-Twiss experiment. Both, the EL intensity and lifetimes were quenched as function of the tunneling current. At higher injection rates, excitons already already present in the system are annihalitated by the injected, unbound electrons. The results show that ECA is generally possible in the C_{60} system.

6.4 Possible Interfacial CT-State

In Chap. 5 on the PEN-PFP heterosystem, a CT-related signal was observed in PL and absorption (PLE) measurements for all sample structures. For the PEN-C_{60} system an unambiguous identification of CT-related transitions is not as straightforward. While there are a vast number of studies [16–19, 101–106] dealing with heterosystems of polymers and fullerene derivatives, the majority of these focus on disordered bulk heterostructures. Generally, these consist of domains of the respective constituents which vary widely in their properties, e.g., size, crystallinity, and molecular orientation. These types of materials are not well-suited, to identify effects arising genuinely from the interaction of molecules at the interface.

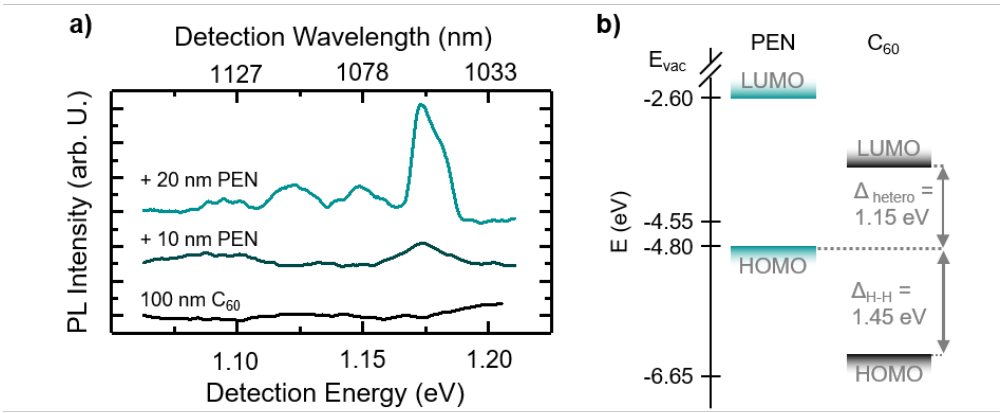

Figure 6.6: (a) PL spectra of three different heterostacks of PEN and C_{60} in the NIR spectral range. The emission of a 100 nm thick unitary C_{60} film is given for reference (grey dots), indicating no emission in the respective spectral region. The excitation energy was set to 1.55 eV (800 nm). (b) The energy level diagram for a heterostack of 13 nm PEN covered with 13 nm C_{60} on PEDOT:PSS substrate. Adapted from Ref. [107].

Regardless of the aforementioned, optical signals unique to the heterosystem can be obtained, even if oscillator strengths prove to be very weak. The graph in Fig. 6.6(a) shows a PL spectrum of PEN-C_{60} heterostacks in the NIR spectral range. For reference, the spectrum of an unitary C_{60} film is also given. The most prominent signal at 1.17 eV is clearly observed exclusively in those samples with PEN coverage. To shed further light on the origin of the signal at 1.17 eV, PES measurements from Ref. [107] are taken into account. For the PES measurements, an approximately 6 nm thick C_{60} layer grown on top of a 13 nm PEN bottom layer was chosen. The substrate used in the study was PEDOT:PSS, a conducting polymeric material. The resulting energy level diagram is shown in Fig. 6.6(b). The corresponding values for the LUMOs are obtained by adding to the HOMO level energy the HOMO-LUMO transition energy, e.g., the transport gap. For PEN, a value of 2.2 eV is broadly accepted. For C_{60}, this value varies from 2.4 eV to 3.4 eV. A value of 2.6 eV [80] is selected because of the structural similarities of the samples under study here and those in the cited article. Given this value for the HOMO-LUMO transition, the hetero-offset Δ_{hetero} between PEN HOMO und C_{60} LUMO amounts to 1.15 eV. As no other transitions in either of the constituents that low in energy are known, the transition at 1.17 eV is tentatively assigned to the C_{60} LUMO - PEN HOMO transition and is thus tentatively labeled a CT transition.

To further elucidate the nature of this transition, its excitation energy dependence is probed by using three distinct excitation energies. Besides the below-gap excitation at 1.5 eV, excitation energies of 3.0 eV and 4.5 eV were selected. Unfortunately, the PLE experiment is not suited for this measurement, due to a lack of both detection ($E_{det} \leq 1.1\,\text{eV}$) and excitation energy range ($E_{exc} \geq 2.5\,\text{eV}$). For $E_{exc} = 3.0\,\text{eV}$, the excitation predominantly takes place in the C_{60} (cf. colored arrows in Fig. 6.1). As discussed previously, the TDM of the second allowed transition is orientated along the long molecular axis of PEN and is thus inaccessible in the case of standing PEN. Finally for, $E_{exc} = 4.5\,\text{eV}$ absorption takes place in both constituent materials. The results of the excitation energy dependent measurements are presented in Fig. 6.7. Intriguingly, for the case of excitation at 3.0 eV, no PL in the spectral range of the CT-related signal is observed. At 4.5 eV, the signal is much more pronounced due to the very large absorption cross-section in both PEN and C_{60}, respectively.

This result comes unexpectedly, since electron- and hole-transfer should both lead to the excitation of the CT state. Apparently, as in the case of PEN-PFP, a population of the CT-related state via a hole-transfer from the acceptor (C_{60}) does not occur. This

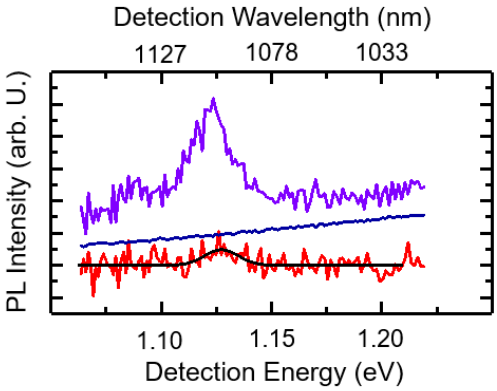

Figure 6.7: PL spectra of the CT-related transition for various excitation energies (1.5 eV, 3.0 eV and 4.5 eV). In the case of 1.5 eV excitation a Gaussian fit of the peak is added as guide to the eye.

result seems in conflict with the literature, where photon absorption in the C_{60} layer has been shown to efficiently generate photocurrent in a photodetector [108] and in an OPV [109] device scheme. Two very important aspects have to be taken into account. First, one could argue that this is due to the fact that the carriers are highly localized in C_{60}, especially at the low temperatures used in the experiments presented in this thesis. As a consequence, diffusion to the heterointerface and consecutive dissocation / population of the CT is far less likely. However, C_{60} molecules and crystals also feature a very high ISC yield (PLQY on the order of 10^{-3}), accompanied by a long triplet lifetime on the order of $\tau_T > 1\,\mu s$ [110]. This renders non-negligible (triplet) exciton diffusion lengths (L_D = 8–40 nm) [94–96]. In turn, photocurrents can still reach the values reported in Refs. [108, 109]. Also, when 2PPE or SHG experiments are performed as, e.g., in Refs. [111,112], multiplicity is not of concern, an aspect which is often ignored. However, as the ground states of both PEN and C_{60} are of singlet character, this plays an undeniable role when considering optical (dipole) transitions. This provides an explanation as to why the CT-related PL is not observed when exciting with 3 eV laser light. On the other hand, if, at 1.5 eV, the CT is directly excited across the internal interface, the singlet CT state is populated and radiative recombination to the singlet ground states is allowed. The very low intensity of the CT-related PL is explained by the generally miniscule absorption cross sections of CT states and thus low direct population of the CT singlet state. Furthermore, theoretical considerations for the radiative recombination rates from the singlet CT state to the ground state (of

PEN) have been calculated to be in the range of $10^5\,\mathrm{s}^{-1}$ [113].

A figure of merit for the exciton binding energy of the CT exciton can be estimated from the excitation energy dependent measurement. Given the energy difference between the energy of the excitation light in the case of direct excitation and the energetic position of the CT-related PL, $E_{exc} - E_{CTPL} = 1.55\,\mathrm{eV} - 1.17\,\mathrm{eV} = 0.38\,\mathrm{eV}$, it becomes evident that the binding energy of the CT exciton lies in the range of 0.4 eV. Such a value is not uncommon in organic semiconductors however, it appears exceedingly large for CT excitons, given that it amounts, e.g., to only 0.1 eV in the PEN-PFP heterosystem. Also, such a large binding energy should prohibit or at least hamper dissocitation of CT excitons into free electrons and holes, respectively.

7 Conclusions

The field of organic semiconductors is an ever emerging one. Yet, a comprehensive interpretation of many effects remains elusive. This thesis aims to help close some of the gaps and so contribute to achieving these higher goals. The interpretation of the formation of CT states at an organic D-A interface is still very crude and often relies on the simplification that an organic solid is little more than an individual molecule in a periodic surrounding. However, this picture has been challenged by many results in the past decade and is further challenged by the results presented here.

The material class of substituted perylenes was introduced. The broad range of potential applications and almost endless possibilities for chemical modifications make this class of materials an important and highly promising area of investigation and prompted the analyses discussed here. As is true for many organic materials, the comprehensive understanding of fundamental processes occurring in these system, is still far from satisfactory understood. For this thesis, novel PDI chromophores with a special focus on substitution at the iminde-N position were synthesized. The process responsible for PL quenching in unprotonated compounds could be attributed to the MO associated with the terminal amine at an energy interfering with the optically bright $\pi \leftarrow \pi^*$ transition. The CS dynamics are controlled by chemical modifications and by controlling experimental conditions, respectively. The observation of drastically reduced PLQY upon introduction of a potential electron donor unit was attributed to a CT process to π orbital of the perylene core. Protonation of the D unit led to only a weak recovery of the PLQY despite DFT calculations suggesting elsewise. The puzzling observation of a non-single-exponential decay of the emissive state was interpreted in terms of a reversible CS process, leading to de- and repopulation of the optically bright S_1 state. By careful evaluation of the decay dynamics, a three-level model was proposed. Following an established procedure, all relevant rates, including the dark ones, could be extracted from the experimental data. The results shed light on the

PEPs of the excited states and revealed unexpected behavior in the Marcus theory of CT. Finally, by exciting higher lying singlet states, the CS could also be controlled. This apparent anti-Kasha behavior was attributed to two effects. First, a very large number of vibrational quanta are excited due to the excess energy. This in turn alters the vibrational coupling between the excited singlet and CSS, respectively. This then affects the CS rates. Alternatively, the dissipation of the excess excitation energy to the surrounding medium could lead to a local heating. This increased vibrational motion of the solvent molecules than would give rise to distortions of either the length of the D-A spacing or the reorganization energies.

The second study was aimed at investigating the properties of an interface made up of two semiconducting organic materials. Also, the impact of molecular orientation on electronic coupling at the heterointerface was an aim of the study. Lastly, the coupling of excitations located in the D and A, respectively, to the CT state was investigated. To this end, the excitation energy-dependent injection efficiency was studied. Indeed, by utilizing a highly sensitive PLE technique, a CT state could be detected in absorption. The evaluation of the two different molecular arrangements at the interface revealed the effect of increased coupling due to the π-stacking of the interfacial molecules. However, the measured CT state energy proved to be incompatible with measurements on the hetero-offset determined by UPS. In stark contrast to the results from UPS, the CT state's energy is unchanged for the different molecular orientations in the experiments performed in this work. This indicates that the idea of superimposing the two quasi-particle energies of the D and A entities in order to reveal the CT energy is deficient. This is corroborated by the lack of an observable hole-transfer from the PFP to the CT state, which is in conflict with the picture of a "simple" CT exciton.

In the case of the PEN-C_{60} heterosystem, such a comprehensive picture could not be obtained. This is mainly due to the complexity of the energy levels in the C_{60} systems, the large shifts of electronic energy levels with the degree of crystallinity, and the structural differences between the two constituents, compared to PEN-PFP. Especially the latter aspect impedes a study of the effects of altered electronic coupling resulting from mutual molecular orientation at the interface. Despite the challenges in the growth of samples of high structural quality, various effects related to the heterointerface were observed. Firstly, a quenching mechanism, leading to drastically reduced lifetimes of the C_{60}-based excitons was found. While a RET from the excited C_{60} state to ground state PEN appears likely intuitively, the vanishing overlap integral between

the potential partners renders this path unlikely. On the other hand, an ECA-type RET could also be possible. The red-shift of cationic states and the long lifetime of charges in this type of organic semiconductors renders this explanation a plausible one. Still, a definitive answer requires a more sophisticated technique (e.g., transient absorption spectroscopy) than was available in the context of this thesis. To date (and to the knowledge of the author), no direct spectroscopic evidence of a CT state for well-defined heterointerfaces of PEN and C_{60} exists. Within this thesis, specific spectroscopic signatures related to the heterointerface were found. While the possible CT state's energy could be located at $(1.17 \pm 0.04)\,\mathrm{eV}$ in emission, there again exist contradictory results obtained by PES. Furthermore, the results of the excitation energy-dependent experiments again indicate that a hole-transfer from the A material does not lead to detectable CT PL. This reinforces the assumption that the frontier MOs are perturbed at an organic heterointerface.

Because of the potential implications of the obtained results, efforts should be undertaken to theoretically address aspects such as formation of CT states at the interface or the injection efficiency into the former. Both crystalline systems under study form an ideal starting point for ab initio calculations on small molecule model systems, as their opto-electronic properties are far less complex than those of materials typically used in OPV structures, e.g., polymer chains. The open-circuit voltage, V_{OC}, directly linked to CT exciton energy, and is one of the key aspects of device optimization. Hence, knowledge of the respective energies and possibly even predictive capabilities are strongly desired in this regard.

Bibliography

[1] J Bardeen and W. H. Brattain. Transistor, a semiconductor triode. *Proceedings of the IEEE*, 86(1):29–30, jan 1998.

[2] T. H. Maiman. Stimulated optical radiation in Ruby. *Nature*, 187(4736):493–494, aug 1960.

[3] Jack.S. Kilby. Miniaturized electronic circuits, 1964.

[4] Vaclav Smil. Energy at the Crossroads. In *OECD Global Science Forum Conference on Scientific Challenges for Energy Research*, page 28, 2006.

[5] I S E Fraunhofer. Photovoltaics Report. Technical Report February, Fraunhofer Institute for Solar Energy and Systems, 2013.

[6] Arne C. Morteani, Anoop S. Dhoot, Ji Seon Kim, Carlos Silva, Neil C. Greenham, Craig Murphy, Ellen Moons, Salvatore Ciná, Jeremy H. Burroughes, and Richard H. Friend. Barrier-Free Electron-Hole Capture in Polymer Blend Heterojunction Light-Emitting Diodes. *Advanced Materials*, 15(20):1708–1712, oct 2003.

[7] Koen Vandewal. Interfacial Charge Transfer States in Condensed Phase Systems. *Annu. Rev. Phys. Chem.*, 67(February):1–21, 2016.

[8] Nikolai I. Georgiev, Alaa R. Sakr, and Vladimir B. Bojinov. Design and synthesis of novel fluorescence sensing perylene diimides based on photoinduced electron transfer. *Dyes and Pigments*, 91(3):332–339, dec 2011.

[9] Frank Würthner, Chantu R. Saha-Möller, Benjamin Fimmel, Soichiro Ogi, Pawaret Leowanawat, and David Schmidt. Perylene Bisimide Dye Assemblies as Archetype Functional Supramolecular Materials, feb 2016.

[10] Leah E Shoer, Samuel W Eaton, Eric A Margulies, and Michael R Wasielewski. Photoinduced Electron Transfer in 2,5,8,11-Tetrakis-Donor-Substituted Perylene-3,4:9,10-bis(dicarboximides). *The journal of physical chemistry. B*, dec 2014.

[11] Yuanping Yi, Veaceslav Coropceanu, and Jean-Luc Brédas. Exciton-dissociation and charge-recombination processes in pentacene/C60 solar cells: theoretical insight into the impact of interface geometry. *Journal of the American Chemical Society*, 131(43):15777–83, nov 2009.

[12] Sean M. Ryno, Stephen R. Lee, John S. Sears, Chad Risko, and Jean-Luc Brédas. Electronic Polarization Effects upon Charge Injection in Oligoacene Molecular Crystals: Description via a Polarizable Force Field. *The Journal of Physical Chemistry C*, 117(27):13853–13860, jul 2013.

[13] Steffen Duhm, Ingo Salzmann, Georg Heimel, Martin Oehzelt, Anja Haase, Robert L Johnson, Jürgen P Rabe, and Norbert Koch. Controlling energy level offsets in organic/organic heterostructures using intramolecular polar bonds. *Applied Physics Letters*, 94(3), 2009.

[14] K. Broch, U. Heinemeyer, A. Hinderhofer, F. Anger, R. Scholz, A. Gerlach, and F. Schreiber. Optical evidence for intermolecular coupling in mixed films of pentacene and perfluoropentacene. *Physical Review B*, 83(24):245307, jun 2011.

[15] Ingo Salzmann, Armin Moser, Martin Oehzelt, Tobias Breuer, Xinliang Feng, Zhen-Yu Juang, Dmitrii Nabok, Raffaele G Della Valle, Steffen Duhm, Georg Heimel, Aldo Brillante, Elisabetta Venuti, Ivano Bilotti, Christos Christodoulou, Johannes Frisch, Peter Puschnig, Claudia Draxl, Gregor Witte, Klaus Müllen, and Norbert Koch. Epitaxial growth of π-stacked perfluoropentacene on graphene-coated quartz. *ACS nano*, 6(12):10874–83, dec 2012.

[16] Hannes Kraus, Michael C Heiber, Stefan Väth, Julia Kern, Carsten Deibel, Andreas Sperlich, and Vladimir Dyakonov. Analysis of Triplet Exciton Loss Pathways in PTB7:PC71BM Bulk Heterojunction Solar Cells. *Scientific reports*, 6(July):29158, 2016.

[17] Marina Gerhard, Andreas P. Arndt, Mühenad Bilal, Uli Lemmer, Martin Koch, and Ian A. Howard. Field-induced exciton dissociation in PTB7-based organic solar cells. *Physical Review B*, 95(19):1–12, 2017.

[18] Xingxing Shen, Guangchao Han, Di Fan, Yujun Xie, and Yuanping Yi. Hot Charge-Transfer States Determine Exciton Dissociation in the DTDCTB/C 60 Complex for Organic Solar Cells: A Theoretical Insight. *The Journal of Physical Chemistry C*, 119(21):11320–11326, may 2015.

[19] Gordon J. Hedley, Alexander J. Ward, Alexander Alekseev, Calvyn T. Howells, Emiliano R. Martins, Luis A. Serrano, Graeme Cooke, Arvydas Ruseckas, and Ifor D. W. Samuel. Determining the optimum morphology in high-performance polymer-fullerene organic photovoltaic cells. *Nature Communications*, 4:1–10, dec 2013.

[20] Tobias Breuer and Gregor Witte. Diffusion-Controlled Growth of Molecular Heterostructures: Fabrication of Two-, One-, and Zero-Dimensional C 60 Nanostructures on Pentacene Substrates. *ACS Applied Materials & Interfaces*, 5(19):9740–9745, oct 2013.

[21] Tobias Breuer, Andrea Karthäuser, and Gregor Witte. Effects of Molecular Orientation in Acceptor-Donor Interfaces between Pentacene and C 60 and Diels-Alder Adduct Formation at the Molecular Interface. *Advanced Materials Interfaces*, 3(7):1500452, apr 2016.

[22] Markus Schwoerer and Hans Christoph Wolf. *Organic Molecular Solids*. Wiley-VCH Verlag GmbH, 2007.

[23] Hermann Haken and Hans Christian Wolf. *Molekülphysik und Quantenchemie: Einführung in die experimentellen und theoretischen Grundlagen*. Springer DE, 2006.

[24] Wolfgang Demtröder. *Expirmentalphysik 3*. Springer DE, 2010.

[25] Sebastian Seiffert and Joris Sprakel. *Physical chemistry of supramolecular polymer networks*, volume 41. W. H. Freeman and Company, New York, New York, 8th edition, 2012.

[26] H. H. Jaffe and Albert L. Miller. The fates of electronic excitation energy. *Journal of Chemical Education*, 43(9):469, sep 1966.

[27] Frank C. Spano. The Spectral Signatures of Frenkel Polarons in H- and J-Aggregates. *Accounts of Chemical Research*, 43(3):429–439, mar 2010.

[28] D. McQuarrie. *Physical Chemistry, A Molecular Approach*. University Science Books, 2003.

[29] S. Singh, W. J. Jones, W. Siebrand, B. P. Stoicheff, and W. G. Schneider. Laser Generation of Excitons and Fluorescence in Anthracene Crystals. *The Journal of Chemical Physics*, 42(1):330–342, jan 1965.

[30] William Shockley and Hans J. Queisser. Detailed balance limit of efficiency of p-n junction solar cells. *Journal of Applied Physics*, 32(3):510–519, mar 1961.

[31] Claude Cohen-Tannoudji, Bernard Diu, and Franck Laloe. *Quantum Mechanics - Volume one*. Wiley, 1st edition, 1991.

[32] Robert L. Fulton and Martin Gouterman. Vibronic Coupling. I. Mathematical Treatment for Two Electronic States. *The Journal of Chemical Physics*, 35(3):1059–1071, sep 1961.

[33] Rudolph A. Marcus. Electron transfer reactions in chemistry. Theory and experiment. *Reviews of Modern Physics*, 65(3):599–610, jul 1993.

[34] Th. Förster. Zwischenmolekulare Energiewanderung und Fluoreszenz. *Annalen der Physik*, 437(1-2):55–75, 1948.

[35] Th. Förster. 10th Spiers Memorial Lecture. Transfer mechanisms of electronic excitation. *Discuss. Faraday Soc.*, 27(16):7–17, 1959.

[36] Albert Weller. Photoinduced Electron Transfer in Solution: Exciplex and Radical Ion Pair Formation Free Enthalpies and their Solvent Dependence. *Zeitschrift für Physikalische Chemie*, 133(1):93–98, jan 1982.

[37] Michael Kasha, H R Rawls, and M Ashraf El-Bayoumi. The exciton model in molecular spectroscopy. *Pure and Applied Chemistry*, 11(3-4):371–392, jan 1965.

[38] Willy. Herbst and Klaus. Hunger. *Industrial organic pigments : production, properties, applications*. VCH, 1997.

[39] Samuel W. Eaton, Leah E. Shoer, Steven D. Karlen, Scott M. Dyar, Eric A. Margulies, Brad S. Veldkamp, Charusheela Ramanan, Daniel A. Hartzler, Sergei Savikhin, Tobin J. Marks, and Michael R. Wasielewski. Singlet exciton fission in polycrystalline thin films of a slip-stacked perylenediimide. *Journal of the American Chemical Society*, 135(39):14701–14712, oct 2013.

[40] Heinz Langhals, Jan Karolin, and Lennart B-Å Johansson. Spectroscopic properties of new and convenient standards for measuring fluorescence quantum yields. *Journal of the Chemical Society, Faraday Transactions*, 94(19):2919–2922, 1998.

[41] Michael W. Holman, Ruchuan Liu, Ling Zang, Ping Yan, Sara A. DiBenedetto, Robert D. Bowers, and David M. Adams. Studying and switching electron transfer: From the ensemble to the single molecule. *Journal of the American Chemical Society*, 126(49):16126–16133, 2004.

[42] Thea M. Wilson, Michael J. Tauber, and Michael R. Wasielewski. Toward an n-type molecular wire: Electron hopping within linearly linked perylenediimide oligomers. *Journal of the American Chemical Society*, 131(25):8952–8957, jul 2009.

[43] Christopher Menelaou, Jeroen ter Schiphorst, Amol M. Kendhale, Patrick Parkinson, Michael G. Debije, Albertus P.H.J. Schenning, and Laura M. Herz. Rapid energy transfer enabling control of emission polarization in perylene bisimide donor-acceptor triads. *Journal of Physical Chemistry Letters*, 6(7):1170–1176, apr 2015.

[44] Ana Morandeira, Jérôme Fortage, Tomas Edvinsson, Loïc Le Pleux, Errol Blart, Gerrit Boschloo, Anders Hagfeldt, Leif Hammarström, and Fabrice Odobel. Improved photon-to-current conversion efficiency with a nanoporous p-type NiO electrode by the use of a sensitizer-acceptor dyad. *Journal of Physical Chemistry C*, 112(5):1721–1728, 2008.

[45] Elizabeth A. Gibson, Amanda L. Smeigh, Loïc Le Pieux, Jérôme Fortage, Gerrit Boschloo, Errol Blart, Yann Pellegrin, Fabrice Odobel, Anders Hagfeldt, and Leif Hammarström. A p-type NiO-based dye-sensitized solar cell with an open-circuit voltage of 0.35 v. *Angewandte Chemie - International Edition*, 48(24):4402–4405, jun 2009.

[46] Loïc Le Pleux, Amanda L. Smeigh, Elizabeth Gibson, Yann Pellegrin, Errol Blart, Gerrit Boschloo, Anders Hagfeldt, Leif Hammarström, and Fabrice Odobel. Synthesis, photophysical and photovoltaic investigations of acceptor-functionalized perylene monoimide dyes for nickel oxide p-type dye-sensitized solar cells. *Energy & Environmental Science*, 4(6):2075, jun 2011.

[47] Julien Warnan, James Gardner, Loïc Le Pleux, Jonas Petersson, Yann Pellegrin, Errol Blart, Leif Hammarström, and Fabrice Odobel. Multichromophoric sensitizers based on squaraine for NiO based dye-sensitized solar cells. *Journal of Physical Chemistry C*, 118(1):103–113, jan 2014.

[48] Sridhar Rajaram, Ravichandran Shivanna, Sunil Kumar Kandappa, and K. S. Narayan. Nonplanar perylene diimides as potential alternatives to fullerenes in organic solar cells. *Journal of Physical Chemistry Letters*, 3(17):2405–2408, sep 2012.

[49] Ravichandran Shivanna, Sridhar Rajaram, and K. S. Narayan. Interface engineering for efficient fullerene-free organic solar cells. *Applied Physics Letters*, 106(12):123301, mar 2015.

[50] Chen Hao Wu, Chu Chen Chueh, Yu Yin Xi, Hong Liang Zhong, Guang Peng Gao, Zhao Hui Wang, Lilo D. Pozzo, Ten Chin Wen, and Alex K.-Y. Jen. Influence of Molecular Geometry of Perylene Diimide Dimers and Polymers on Bulk Heterojunction Morphology Toward High-Performance Nonfullerene Polymer Solar Cells. *Advanced Functional Materials*, 25(33):5326–5332, sep 2015.

[51] Long Ye, Kai Sun, Wei Jiang, Shaoqing Zhang, Wenchao Zhao, Huifeng Yao, Zhaohui Wang, and Jianhui Hou. Enhanced efficiency in fullerene-free polymer solar cell by incorporating fine-designed donor and acceptor materials. *ACS Applied Materials and Interfaces*, 7(17):9274–9280, may 2015.

[52] Robin C. Döring, Eduard Baal, Malcolm A. Bartlett, Christian Prinzisky, Remco W. A. Havenith, Jörg Sundermeyer, and Sangam Chatterjee. Control of Intramolecular Electron Transfer in Perylene Dihydrazides and Perylene Diimides : A Comparative Study by Time-Resolved Spectroscopy. 281:1–35, dec 2016.

[53] Lucia Flamigni, Alberto Zanelli, Heinz Langhals, and Bernd Böck. Photoinduced processes in a dyad made of a linear and an angular perylene bisimide. *Photochemical & Photobiological Sciences*, 12(12):2137, 2013.

[54] T Kircher and H G Lohmannsroben. Photoinduced charge recombination reactions of a perylene dye in acetonitrile. *Phys. Chem. Chem. Phys.*, 1(17):3987–3992, 1999.

[55] Svend J Knak Jensen, Ting-Hua Tang, and Imre G Csizmadia. Hydrogen-Bonding Ability of a Methyl Group. *The Journal of Physical Chemistry A*, 107(42):8975–8979, oct 2003.

[56] Edda E. Neuteboom, Stefan C.J. Meskers, Paul A. Van Hal, Jeroen K.J. Van Duren, E. W. Meijer, René A.J. Janssen, Hélène Dupin, Geoffrey Pourtois, Jérôme Cornil, Roberto Lazzaroni, Jean Luc Brédas, and David Beljonne. Alternating oligo(p-phenylene vinylene)-perylene bisimide copolymers: Synthesis, photophysics, and photovoltaic properties of a new class of donor-acceptor materials. *Journal of the American Chemical Society*, 125(28):8625–8638, 2003.

[57] Joanna Wiberg, Lijun Guo, Karin Pettersson, Daniel Nilsson, Thomas Ljungdahl, Jerker Mårtensson, and Bo Albinsson. Charge recombination versus charge separation in donor-bridge-acceptor systems. *Journal of the American Chemical Society*, 129(1):155–63, jan 2007.

[58] Karin Pettersson, Joanna Wiberg, Thomas Ljungdahl, Jerker Mårtensson, and Bo Albinsson. Interplay between barrier width and height in electron tunneling: photoinduced electron transfer in porphyrin-based donor-bridge-acceptor systems. *The Journal of Physical Chemistry A*, 110(1):319–26, jan 2006.

[59] Jie Huang, Hongbing Fu, Yishi Wu, Shiyan Chen, Fugang Shen, Xiaohui Zhao, Yunqi Liu, and Jiannian Yao. Size effects of oligothiophene on the dynamics of electron transfer in π-conjugated oligothiophene-perylene bisimide dyads. *Journal of Physical Chemistry C*, 112(7):2689–2696, 2008.

[60] R. M. Hochstrasser. On the problem of radiative combinations between upper singlet states and the ground state in aromatic molecules*. *Spectrochimica Acta*, 16(1958):497–504, 1960.

[61] Oleksandr Yushchenko, Giuseppe Licari, Sandra Mosquera-Vazquez, Naomi Sakai, Stefan Matile, and Eric Vauthey. Ultrafast intersystem-crossing dynamics and breakdown of the Kasha-Vavilov's rule of naphthalenediimides. *Journal of Physical Chemistry Letters*, 6(11):2096–2100, jun 2015.

[62] Ralph S Becker, Anna Paola Pelliccioli, Aldo Romani, and Gianna Favaro. Vibronic quantum effects in fluorescence and photochemistry. Competition between vibrational relaxation and photochemistry and consequences for photochemical control. *Journal of the American Chemical Society*, 121(10):2104–2109, 1999.

[63] Alexander P Demchenko, Vladimir I Tomin, and Pi Tai Chou. Breaking the Kasha Rule for More Efficient Photochemistry. *Chemical Reviews*, 117(21):13353–13381, nov 2017.

[64] Ralph S. Becker and Gianna Favaro. New concepts in photochemistry and photophysics: Photochromic and other type molecules, nov 2011.

[65] C. Rulliere, A. Declemy, and Ph. Kottis. Picosecond spectroscopic investigation of the internal conversion rate of excited perylene in solution. *Chemical Physics Letters*, 110(3):308–314, 1984.

[66] Stefan Schiefer, Martin Huth, Alexander Dobrinevski, and Bert Nickel. Determination of the Crystal Structure of Substrate-Induced Pentacene Polymorphs in Fiber Structured Thin Films. *Journal of the American Chemical Society*, 129(34):10316–10317, aug 2007.

[67] Theo Siegrist, Christian Kloc, Jan H. Schön, Bertram Batlogg, Robert C. Haddon, Steffen Berg, and Gordon A. Thomas. Enhanced physical properties in a pentacene polymorph. *Angewandte Chemie - International Edition*, 40(9):1732–1736, may 2001.

[68] R. B. Campbell, J. M. Robertson, and J. Trotter. The crystal structure of hexacene, and a revision of the crystallographic data for tetracene. *Acta Crystallographica*, 15(3):289–290, mar 1962.

[69] Tobias Breuer and Gregor Witte. Controlling Nanostructures by Templated Templates: Inheriting Molecular Orientation in Binary Heterostructures. *ACS Applied Materials & Interfaces*, 7(36):20485–20492, sep 2015.

[70] Kolja Kolata. *Exciton Dynamics in Perfluoropentacene Single Crystals*. PhD thesis, Philipps-Universität Marburg, 2014.

[71] Alexander Hinderhofer, Ute Heinemeyer, Alexander Gerlach, Stefan Kowarik, Robert M.J. Jacobs, Youichi Sakamoto, Toshiyasu Suzuki, and Frank Schreiber. Optical properties of pentacene and perfluoropentacene thin films. *Journal of Chemical Physics*, 127(19):194705, nov 2007.

[72] Murilo L. Tiago, John E. Northrup, and Steven G. Louie. Ab initio calculation of the electronic and optical properties of solid pentacene. *Physical Review B*, 67(11):115212, 2003.

[73] Sahar Sharifzadeh, Ariel Biller, Leeor Kronik, and Jeffrey B. Neaton. Quasiparticle and optical spectroscopy of the organic semiconductors pentacene and PTCDA from first principles. *Physical Review B - Condensed Matter and Materials Physics*, 85(12):1–11, 2012.

[74] H. Yamagata, J. Norton, E. Hontz, Y. Olivier, D. Beljonne, J. L. Brédas, R. J. Silbey, and F. C. Spano. The nature of singlet excitons in oligoacene molecular crystals. *Journal of Chemical Physics*, 134(20), 2011.

[75] Sahar Sharifzadeh, Pierre Darancet, Leeor Kronik, and Jeffrey B Neaton. Low-energy charge-transfer excitons in organic solids from first-principles: The case of pentacene. *Journal of Physical Chemistry Letters*, 4(13):2197–2201, 2013.

[76] Andre Rinn, Tobias Breuer, Julia Wiegand, Michael Beck, Jens Hübner, Robin C. Döring, Michael Oestreich, Wolfram Heimbrodt, Gregor Witte, and Sangam Chatterjee. Interfacial Molecular Packing Determines Exciton Dynamics in Molecular Heterostructures: The Case of Pentacene-Perfluoropentacene. *ACS Applied Materials & Interfaces*, 9(48):42020–42028, dec 2017.

[77] Ingo Salzmann, Steffen Duhm, Georg Heimel, Martin Oehzelt, Rolf Kniprath, Robert L. Johnson, Jürgen P. Rabe, and Norbert Koch. Tuning the ionization energy of organic semiconductor films: The role of intramolecular polar bonds. *Journal of the American Chemical Society*, 130(39):12870–12871, 2008.

[78] W. I. F David, R. M Ibberson, T. J. S Dennis, J. P Hare, and K. Prassides. Structural Phase Transitions in the Fullerene. *Europhysics Letters*, 18(February):219–225, 1992.

[79] R W Lof, M A Van Veenendaal, B Koopmans, H T Jonkman, G A Sawatzky, and Materials Science Centre. Band Gap, Excitons, and Coulomb Interaction in Solid C60. *Physical Review Letters*, 68(26):1–4, 1992.

[80] R. Mitsumoto, K. Seki, T. Araki, E. Ito, Y. Ouchi, Y. Achiba, K. Kikuchi, S. Yajima, S. Kawasaki, F. Okino, H. Touhara, H. Kurosaki, T. Sonoda, and H. Kobayashi. Soft X-ray absorption, UV photoemission, and VUV absorption spectroscopic studies of fluorinated fullerenes. *Journal of Electron Spectroscopy and Related Phenomena*, 78:453–456, may 1996.

[81] Tetsuo Soga. *Nanostructured Materials for Solar Energy Conversion*. Elsevier B.V., Cambridge, 2006.

[82] Yao Tsung Fu, Chad Risko, and Jean Luc Brédas. Intermixing at the pentacene-fullerene bilayer interface: A molecular dynamics study. *Advanced Materials*, 25(6):878–882, feb 2013.

[83] V. Capozzi, G. Casamassima, G. F. Lorusso, A. Minafra, R. Piccolo, T. Trovato, and A. Valentini. Optical spectra and photoluminescence of C60 thin films. *Solid State Communications*, 98(9):853–858, jun 1996.

[84] H. Schlaich, M. Muccini, J. Feldmann, H. Bässler, E. O. Göbel, R. Zamboni, C. Taliani, J. Erxmeyer, and A. Weidinger. Absorption at the dipole-forbidden optical gap of crystalline C60. *Chemical Physics Letters*, 236(1-2):135–140, 1995.

[85] Tamihiro Gotoh, Shuichi Nonomura, Hideki Watanabe, Shoji Nitta, and Daxing Han. Temperature dependence of the optical-absorption edge in C60 thin film. *Physical Review B*, 58(15):60–63, oct 1998.

[86] W Guss, J Feldmann, E. O. Göbel, C. Taliani, H. Mohn, W. Müller, P. Häussler, and H.-U. ter Meer. Fluorescence from X traps in C 60 single crystals. *Physical Review Letters*, 72(16):2644–2647, apr 1994.

[87] Fabrizia Negri, Giorgio Orlandi, and Francesco Zerbetto. Interpretation of the vibrational structure of the emission and absorption spectra of C 60. *The Journal of Chemical Physics*, 97(9):6496–6503, nov 1992.

[88] Donald S. Bethune, Gerard Meijer, Wade C. Tang, Hal J. Rosen, William G. Golden, Hajime Seki, Charles A. Brown, and Mattanjah S. de Vries. Vibrational Raman and infrared spectra of chromatographically separated C60 and C70 fullerene clusters. *Chemical Physics Letters*, 179(1-2):181–186, apr 1991.

[89] J. L. Sauvajol, Z. Hricha, N. Coustel, Z. Zahab, and R. Aznar. Photoluminescence of solid C 60. *Journal of Physics: Condensed Matter*, 5(13):2045–2054, mar 1993.

[90] M. Matus, H. Kuzmany, and E. Sohmen. Self-trapped polaron exciton in neutral fullerene C60. *Physical Review Letters*, 68(18):2822–2825, may 1992.

[91] K Sinha, J. Menéndez, R.C. Hanson, G.B. Adams, J.B. Page, O.F. Sankey, L.D. Lamb, and D.R. Huffman. Evidence for solid-state effects in the electronic structure of C60 films: a resonance-Raman study. *Chemical Physics Letters*, 186(2-3):287–290, nov 1991.

[92] Paul A. Heiney, John E. Fischer, Andrew R. McGhie, William J. Romanow, Arnold M. Denenstein, John P. McCauley, Amos B. Smith, and David E. Cox. Orientational ordering transition in solid C60. *Physical Review Letters*, 66(22):2911–2914, jun 1991.

[93] R. Tycko, R. C. Haddon, G. Dabbagh, S. H. Glarum, D. C. Douglass, and A. M. Mujsce. Solid-state magnetic resonance spectroscopy of fullerenes. *Journal of Physical Chemistry*, 95(2):518–520, jan 1991.

[94] Leif A A Pettersson, Lucimara S Roman, and Olle Inganäs. Modeling photocurrent action spectra of photovoltaic devices based on organic thin films. *Journal of Applied Physics*, 86(1):487–496, jul 1999.

[95] S. Yoo, B. Domercq, and B. Kippelen. Efficient thin-film organic solar cells based on pentacene/C 60 heterojunctions. *Applied Physics Letters*, 85(22):5427–5429, nov 2004.

[96] Anna Katharina Topczak, M Gruber, Wolfgang Brütting, and J Pflaum. Probing the local structural order of C60 thin films by their exciton transport characteristics. *arXiv*, pages 1–13, 2013.

[97] P. Merino, C. Große, A. Rosławska, K. Kuhnke, and K. Kern. Exciton dynamics of C60-based single-photon emitters explored by Hanbury Brown-Twiss scanning tunnelling microscopy. *Nature Communications*, 6(1):8461, dec 2015.

[98] Song Jie, Li Fei-ming, Qian Shi-xiong, Li Yu-fen, Peng Wen-ji, Zhou Jian-ying, and Yu Zhen-xin. Time decay behavior of fullerene-C 60 studied by time-resolved photoluminescence. *Acta Physica Sinica (Overseas Edition)*, 4(3):175–182, mar 1995.

[99] H.J. J. Byrne, W. K. Maser, W.W. W. Rühle, A. Mittelbach, W. Hönle, H.G. G. von Schnering, B. Movaghar, S. Roth, and B. Movaghar. Time-resolved photoluminescence of solid state fullerenes. *Synthetic Metals*, 54(1-3):265–272, mar 1993.

[100] Justin M. Hodgkiss, Sebastian Albert-Seifried, Akshay Rao, Alex J. Barker, Andrew R. Campbell, R. Alex Marsh, and Richard H. Friend. Exciton-Charge Annihilation in Organic Semiconductor Films. *Advanced Functional Materials*, 22(8):1567–1577, apr 2012.

[101] T. Drori, C.-X. X. Sheng, A. Ndobe, S. Singh, J. Holt, and Z. V. Vardeny. Below-gap excitation of π-conjugated polymer-fullerene blends: Implications for bulk organic heterojunction solar cells. *Physical Review Letters*, 101(3):037401, jul 2008.

[102] Andreas Haugeneder, C. Kallinger, Wolfgang Spirkl, Uli Lemmer, Jochen Feldmann, Ullrich Scherf, E. Harth, Andreas Guegel, and Klaus Muellen. Photoinduced electron transfer in conjugated polymer/fullerene heterostructures. volume 3142, page 140, nov 1997.

[103] A. Haugeneder, M. Neges, C. Kallinger, W. Spirkl, U. Lemmer, J. Feldmann, U. Scherf, E. Harth, A. Gügel, and K. Müllen. Exciton diffusion and dissociation in conjugated polymer/fullerene blends and heterostructures. *Physical Review B*, 59(23):15346–15351, jun 1999.

[104] Brent Kitchen, Omar Awartani, R Joseph Kline, Terry McAfee, Harald Ade, and Brendan T O'Connor. Tuning Open-Circuit Voltage in Organic Solar Cells with Molecular Orientation. *ACS applied materials & interfaces*, 7(24):13208–16, jun 2015.

[105] Kaname Kanai, Kouki Akaike, Kiichirou Koyasu, Kentaro Sakai, Toshio Nishi, Yasunori Kamizuru, Tatsuhiko Nishi, Yukio Ouchi, and Kazuhiko Seki. Determination of electron affinity of electron accepting molecules. *Applied Physics A: Materials Science and Processing*, 95(1):309–313, 2009.

[106] Stoichko D Dimitrov, Scot Wheeler, Dorota Niedzialek, Bob C Schroeder, Hendrik Utzat, Jarvist M Frost, Jizhong Yao, Alexander Gillett, Pabitra S Tuladhar, Iain McCulloch, Jenny Nelson, and James R Durrant. Polaron pair mediated triplet generation in polymer/fullerene blends. *Nature communications*, 6:6501, 2015.

[107] Ingo Salzmann, Steffen Duhm, Ricarda Opitz, Robert L. Johnson, Jürgen P. Rabe, and Norbert Koch. Structural and electronic properties of pentacene-fullerene heterojunctions. *Journal of Applied Physics*, 104(11):114518, dec 2008.

[108] J. Lee, P. Jadhav, and M. A. Baldo. High efficiency organic multilayer photodetectors based on singlet exciton fission. *Applied Physics Letters*, 95(3):033301, jul 2009.

[109] Daniel N. Congreve, Jiye Lee, Nicholas J. Thompson, Eric Hontz, Shane R. Yost, Philip D. Reusswig, Matthias E. Bahlke, Sebastian Reineke, Troy Van Voorhis, and Marc A. Baldo. External Quantum Efficiency Above 100% in a Singlet-Exciton-Fission-Based Organic Photovoltaic Cell. *Science*, 340(6130):334–337, apr 2013.

[110] Peter Peumans, Aharon Yakimov, and Stephen R. Forrest. Small molecular weight organic thin-film photodetectors and solar cells. *Journal of Applied Physics*, 93(7):3693–3723, apr 2003.

[111] Wai Lun Chan, Manuel Ligges, Askat Jailaubekov, Loren Kaake, Luis Miaja-Avila, and X. Y. Zhu. Observing the multiexciton state in singlet fission and ensuing ultrafast multielectron transfer. *Science*, 334(6062):1541–1545, 2011.

[112] Matthias Muntwiler, Qingxin Yang, William A. Tisdale, and X. Y. Zhu. Coulomb barrier for charge separation at an organic semiconductor interface. *Physical Review Letters*, 101(19):196403, nov 2008.

[113] Zilong Zheng, Naga Rajesh Tummala, Yao Tsung Fu, Veaceslav Coropceanu, and Jean Luc Brédas. Charge-Transfer States in Organic Solar Cells: Understanding the Impact of Polarization, Delocalization, and Disorder. *ACS Applied Materials and Interfaces*, 9(21):18095–18102, may 2017.